A POSITRON DETECTOR FOR PRECISION BETA DECAY EXPERIMENTS FROM A MAGNETO-OPTIC TRAP

by

Dan G. Melconian
B.Sc., M^{c}Master University, 1995

A thesis submitted in partial fulfillment
of the requirements for the degree of
Master of Science
in the
Department of Physics

Simon Fraser
University

Simon Fraser University
July 2000

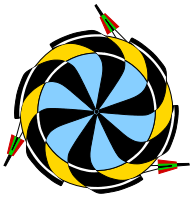

Triumf

Approval

Name: Dan G. Melconian

Degree: Master of Science

Title of thesis: **A Positron Detector for Precision Beta Decay Experiments from a Magneto-Optic Trap**

Examining Committee: Dr. John Bechhoefer – Chair
Associate Professor

Dr. K. Peter Jackson – Senior Supervisor
Associate Member – Senior Research Scientist, TRIUMF

Dr. Byron Jennings
Adjunct Member – Senior Research Scientist, TRIUMF

Dr. Howard Trottier
Associate Professor

Dr. Michel Vetterli
Adjunct Professor – Senior Research Scientist, TRIUMF

Dr. David Hutcheon – External Examiner
Senior Research Scientist, TRIUMF

Date Approved: July 4, 2000

Abstract

The TRINAT collaboration has magneto-optically trapped ^{38m}K from TRIUMF's radioactive beam facility with the goal of measuring to better than 1% the $\beta - \nu$ correlation parameter, a, of the superallowed β decay. This measurement will test the Standard Model prediction of $a = +1$, where a deviation from unity would be a clear indication of scalar contributions to the weak interaction.

The subject of this thesis is the design, optimization and characterization of a plastic scintillator used in coincidence with a double-sided Si-strip detector to observe the E and ΔE of the emitted positron. The timing response of the scintillator relative to a micro-channel plate has a width of $\sigma = 1$ ns, which provides a good time-of-flight measurement used to determine the recoil momentum, allowing that of the neutrino to be deduced.

The scintillator was designed with the aid of Monte Carlo simulations and optimized for the $0 - 5$ MeV region of interest. The energy has been calibrated to within ± 5 keV using the Compton edges of γ sources as well as by the on-line β spectrum. The gain of the scintillator is kept constant over the course of the experiment to within 0.15% by a stabilization system.

The silicon strip detector has been calibrated using photon sources (30–80 keV) and the calibration was extended using the on-line data by requiring energy agreement between the $\hat{x}$ and $\hat{y}$ strips. Using these calibrations, a detailed analysis scheme has been developed that accounts for charge sharing between strips and multiple hits. The strip detector is an important component of the telescope because it provides an effective tag for β events which are needed to discriminate against the ^{38}K γ background in the scintillator. A hardware coincidence between the E and ΔE detectors reduces this background by a factor of 35, and the analysis scheme reduces it another

order of magnitude with minimal loss of good β events.

The β telescope's energy spectrum from the April–May 1999 experimental run is well reproduced by detailed simulations above 2.5 MeV, the lowest β energy expected to be used in the analysis of a. The simulations are not quite as accurate in reproducing the background and the Compton summing of the annihilation radiation, limiting our understanding of the lower-energy part of the β spectrum. A coincidence condition with the recoil detector, however, virtually eliminates these backgrounds, providing a clean measurement for the correlation experiment.

In memory of Otto Häusser

There are grounds for cautious optimism that we may now be near the end of the search for the ultimate laws of nature.

Stephen Hawking
A Brief History of Time, 1988

Acknowledgements

I would like to thank first and foremost the late Prof. Otto Häusser for providing me with the wonderful opportunity of working with TRINAT as his student as well as for instilling in me a part of his deep love for physics. I only wish we could have worked together longer because I know there was still *much* more that I could have learned. Thanks to the intervention of Peter Jackson who took over the responsibility of supervising me, I was able to continue my studies. In addition to helping me with analysis and offering ideas on a daily basis, his comments and suggestions on countless drafts of this thesis have been used throughout and have been an immense help to me. John Behr also deserves much credit, for he was the one who first helped me fumble my way through TRINAT's complicated hardware, and was instrumental in the testing and characterization of the scintillator. He has always played an active role in helping me with analysis, performing complementary calculations and taking the time to talk about physics.

I would also like to thank my supervisory committee, Byron Jennings, Howard Trottier and Mike Vetterli for taking an interest in my work and for the help they have given me.

My fellow TRINAT grad students have made the day-to-day routine much more pleasant, especially on those the long, stressful days before and during runs. I owe a lot to Alexandre Gorelov for his work that is used in this thesis which includes (but is not limited to): his recoil tracking code for GEANT; the new DSSSD mount; Figures 3.6, 4.6, (the cube of) 3.4 and B.1; also, he has continually helped me with setting up and optimizing the hardware. I have also learned many computer and 'shop' skills from him, but perhaps most importantly, I would like to thank him for always being up for a coffee/smoke break; I have valued our conversations together

whether they were about physics, current news, or yes, even the war in the Balkans! Mike Trinczek has been a great help to my mental health by always staying positive and taking the time to chat with me about physics as well as life in general. He also tried to foster my physical activity through volleyball, basketball and soccer, but unfortunately, he's only human. As a result of his use of GEANT, a number of bugs were discovered in the code and fixed, and I thank him for useful comments especially with regard to appendix B.2. Good luck with writing up, guys!

I would like to thank the following members of the group for being additional sources of information and guidance. Ulrich Giesen, who set up the hardware for the DSSSD and is responsible for the basis of TRINAT's hardware as a whole, always left his door open and my only regret is I didn't use it often enough while he was in Vancouver. I owe a lot of the clarity in Chapter 2 to Pierre Dubé who was always interested in my work even though it wasn't atomic physics. I have had many useful discussions with Parker Alford who has also helped editing drafts of this thesis. I would also like to thank Trevor Stocki for looking the thesis over, especially appendix B.1.

I did not get a chance to spend as much time with the Jens' that passed through the group (Dilling and Schmid), but am happy to have had the pleasure of working with them. I would like to extend a special thanks to Jens Dilling for making a special effort to make me feel welcome at TRIUMF when I first joined the group.

Many thanks needs to go to Steve Chan and the rest of the guys in the scintillator shop. If not for their patient natures, flexibility with rushed orders, and extended experience with scintillators, the one used in this thesis surely would not have been made as quickly or with as good a quality.

I would also like to acknowledge various help and useful discussions from John D'Auria, Guy Savard, Tom Davinson, Ted Clifford, Pierre Amaudruz, Renée Poutissou, Peter Machule and Jimmy Chow. The stabilization of the scintillator would not have been possible without the generosity of York Holler who has lent TRINAT two of his units. Joe Chuma has written an excellent program in `physica`, which has been used throughout this thesis. Also, thanks to Anna Gelbart for providing me with the basis for Figure 3.5.

The graduate secretary, Candida Mazza, has shielded me from much of the paperwork and has kept track of important dates for me; thank you for letting me

concentrate on physics rather than worrying about bureaurocratic details.

Finally, I would like to thank Jan Blanchard, my family and my friends for their continued support and for always believing in me. Jan, you have been my best friend since the McMaster days, and always having you around through the good times and the bad has made living here in Vancouver infinitely easier. Thank you for taking a genuine interest in my work and for keeping my head on my shoulders these last few years! Mom, Babi, Leon and Sonja: there is no way I would have been here if not for your love, faith and support — there are no adequate words to express my graditude; I just hope I've made you proud!

Table of Contents

List of Tables

List of Figures

Chapter 1

Introduction

As Hawking and other physicists believe (albeit with reservation), we appear to be very close to finally understanding the fundamental laws governing the universe. Improved technologies have allowed measurements that are testing to greater and greater precision the current theory of particle physics: the Standard Model. This model is comprised of quantum electrodynamics (describes electromagnetic processes), the electroweak theory of Glashow, Weinberg and Salam (unifies weak and electromagnetic forces) and quantum chromodynamics (governs strong interactions). The Standard Model cannot be the 'final theory,' however, because it does not unify the electroweak and strong interactions. A 'Grand Unified Theory' is one in which all three interactions are seen to be low-energy manifestations of a single force. The next (and perhaps final?) step would be to include gravity so that all four forces would be described by one ultimate theory.

Hawking retains "optimism" that a unified theory will one day soon be discovered. Perhaps it will be; or, like at the end of the 1800's, perhaps it will be that we will find evidence of *new* physics, this time from results outside the Standard Model. It is my "optimistic" hope that this will be the case so that the physics community will have many new questions to answer for a long time to come.

The Standard Model has to date stubbornly resisted any attempts at proving it wrong; it remains one of the most thoroughly tested models in science, and has not failed yet. It is important to continue searching for physics beyond the Standard Model because any deviation would be an important guide for, or test of, a unified theory.

Precision β decay experiments can be a sensitive test of the Standard Model be-

cause they are inherently weak processes. The novel technology of neutral atom traps has opened the door to a new generation of β decay experiments. TRINAT has utilized this technology and is currently measuring the $\beta - \nu$ correlation parameter, a, in the $0^+ \longrightarrow 0^+$ β^+ decay of ^{38m}K. The value of a is a sensitive probe of possible scalar contributions to the weak interaction; a measurement to 0.1% precision would complement the high-energy searches at accelerators. Although continued data collection is planned to increase statistics with an improved geometry, TRINAT currently has enough for a 0.3% measurement.

This thesis, after an overview of the theory and the correlation experiment, will describe the design and characterization of the β-telescope used by TRINAT to observe the momentum of the emitted positron.

Chapter 2 is an introduction to the theory of β decay. The first section provides a detailed description of Fermi's model so that the reader can have an intuitive understanding of the decay. The more modern and general view of β decay is outlined in the second section, and shows how the correlation parameter affects the decay. A number of books [1, 2, 3] were used as general reference guides for this section.

Chapter 3 is meant to provide details specific to the correlation experiment. Details of the method TRINAT is using to measure a are given in the first section. Following this is an overview of magneto-optic traps and how TRINAT uses them in the experiment. The last section gives a brief description of the nuclear detection system as a whole, which consists of the β-telescope contained in this thesis as well as a recoil detector.

Chapter 4 describes in detail the β-telescope. The first section explains how the telescope as a whole was designed and with what considerations. Section 2 is a detailed description of the double-sided silicon-strip detector, its characteristics and the results obtained from the ^{38m}K data. Following this is a similar section, this time dedicated to the plastic scintillator. Section 4 presents on-line results of the β-telescope as a whole and the final section gives a preliminary analysis of the β–Ar coincidence spectra, although no attempt is made to calculate a as it is outside the scope of this thesis.

Chapter 5 is simply a summary of important results and suggestions for future endeavors.

Chapter 2

β Decay and Fundamental Symmetries

β decay has proven to be an invaluable tool in our study of nuclear and particle physics since the discovery of radioactive decay at the turn of the century. Early experiments observed only two decay products: the recoiling daughter atom and a charge-conserving 'β ray,' which was soon realized to be either an electron (β^-) or a positron (β^+). The simple kinematics of such a two-body decay would require that the β energy spectrum be a peak corresponding to the energy released in the transition, as in α decay. The fact that the emitted β ray was observed to have a continuous energy spectrum prompted Pauli in 1931 to propose that β decay is a *3-body* process, the extra product being a light (or even massless), neutral particle that interacts very weakly with matter and so escapes detection. Only three years later, but twenty years before it was ever proven to exist, Fermi called this elusive particle a *neutrino* when he incorporated it in his theory of β decay. Fermi's model provides us with a simple, intuitive understanding of β decay that, even to this day, remains essentially unchanged.

2.1 The Fermi Model

A nucleus that undergoes β decay converts one of its neutrons into a proton, or vice-versa, so that its nuclear charge, Z, changes by ± 1 but the total number of nucleons,

Type	Operator	Parity
Scalar	$\mathbf{1}$	$+$
Pseudo-scalar	γ_5	$-$
Vector	γ_μ	$+$
Axial vector	$\gamma_\mu\gamma_5$	$-$
Tensor	$\gamma_\mu\gamma_\nu - \gamma_\nu\gamma_\mu$	N/A

TABLE 2.1: Possible forms for an interaction consistent with Lorentz invariance.

A, remains constant. The basic processes underlying these decays at the nucleon level are:

$$\begin{aligned} n &\longrightarrow p + e^- + \overline{\nu}_e \qquad \beta^- \text{ decay} \\ p &\longrightarrow n + e^+ + \nu_e \qquad \beta^+ \text{ decay} \\ p + e^- &\longrightarrow n + \nu_e \qquad \text{orbital electron capture } (\epsilon) \end{aligned}$$

When Fermi first proposed his theory [4], little else was known except that the force inducing the decay was weak compared to the strong force binding the protons and neutrons together to form the nucleus. This allowed Fermi to use first order perturbation theory to derive his Golden Rule, which gives the transition rate for any suitably weak potential V_{int} (for this chapter only, we use natural units so that $\hbar = c = 1$):

$$\lambda = \frac{1}{\tau} = 2\pi |\mathcal{M}_{fi}|^2 \rho(E_f) \tag{2.1}$$

where $\mathcal{M}_{fi} = \int \psi_f^* \, V_{\text{int}} \, \psi_i \, d^3x$ is the matrix element of the interaction and $\rho(E_f)$ is the density of states available to a final state of energy E_f. The mathematical form of V_{int} for weak interactions is not predicted by Fermi's theory, but there are only five combinations of the γ-matrices that are Lorentz covariant; these interaction types are given in Table 2.1. Inspired by electromagnetism, Fermi guessed a vector form for the interaction whose strength[†] is characterized by a coupling constant, G_F. The Feynman diagram of Figure 2.1 is Fermi's model of the β^+ decay of a nucleus, ${}^Z_A X$, using the more modern concepts of hadron and lepton currents. The following discussion will

[†]Experimentally, $G_F = 1.16639(1) \times 10^{-5}$ GeV^{-2} [5].

be restricted to β^+ decay, but calculations for β^- decay are the same except for the direction of the currents.

The contact nature of the model implies the matrix element is simply a contraction of the two currents:

$$\mathcal{M}_{fi} = \int (j^\mu)_{\rm had}\ G_F\ (j_\mu)_{\rm lep}\ d^3x \tag{2.2}$$

where the lepton current is simply given by

$$(j_\mu)_{\rm lep} = \overline{\psi}_{\nu_e}\ \gamma_\mu\ \psi_{e^+} \tag{2.3}$$

The hadron current is slightly more complicated because it must transform one of the protons within the nucleus into a neutron. This involves isospin, a symmetry of the strong interaction, which views protons and neutrons as two 'states' of the same particle, the nucleon. The isospin of a nucleon is $T = \frac{1}{2}$ and the projections[†] T_3 correspond to the two distinct states, the proton ($T_3 = -\frac{1}{2}$) and the neutron ($T_3 = +\frac{1}{2}$). The $SU(2)$ structure of isospin is the same as angular momentum so there are ladder operators, $\tau_\pm|T\ T_3\rangle = \sqrt{T(T+1) - T_3(T_3 \pm 1)}|T\ T_3 \pm 1\rangle$, which transform between these nucleon states. The hadron current for β^+ decay is:

$$(j^\mu)_{\rm had} = \overline{\psi}_Y\, \gamma^\mu \tau_+\, \psi_X \tag{2.4}$$

where we use the τ_+ operator since the isospin is raised in β^+ decay.

We begin calculation of the hadron current by separating the wavefunction of the decaying nucleon from that of the remaining nucleus:

$$\psi_X = \psi_p\ \psi_{\rm nucl}\ \psi_{\rm iso} \tag{2.5}$$

and

$$\overline{\psi}_Y = \overline{\psi}'_{\rm iso}\ \overline{\psi}'_{\rm nucl}\ \overline{\psi}_n \tag{2.6}$$

Here $\psi_{\rm iso}$ and $\psi'_{\rm iso}$ represent the isospin components of the initial and final state (overall) nuclear wavefunctions. Treating the nucleons as structureless, Dirac particles, we

[†]In particle physics, the convention is reversed with the proton in the $T_3 = +\frac{1}{2}$ sublevel.

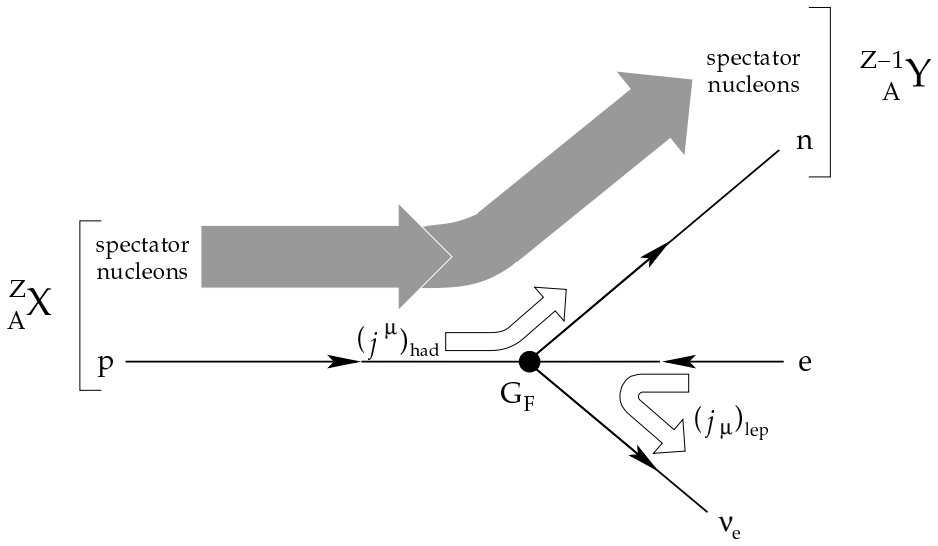

FIGURE 2.1: Fermi's contact, vector-interaction model for the β^+ decay ${}^{Z}_{A}X \longrightarrow {}^{Z-1}_{A}Y + e^+ + \nu_e$.

use wavefunctions of the form†

$$\psi_p = u\, e^{-ip_p\cdot x} = \sqrt{E_p + m_p}\begin{pmatrix} \chi_s \\ \frac{\boldsymbol{\sigma}\cdot\boldsymbol{p}_p}{E_p+m_p}\chi_s \end{pmatrix} e^{-ip_p\cdot x} \tag{2.7}$$

$$\text{and} \qquad \overline{\psi}_n = u^\dagger\,\gamma_0\, e^{ip_n\cdot x} = \sqrt{E_n + m_n}\begin{pmatrix} \chi_r^* & -\frac{\boldsymbol{\sigma}\cdot\boldsymbol{p}_n}{E_n+m_n}\chi_r^* \end{pmatrix} e^{ip_n\cdot x} \tag{2.8}$$

where the χ spinors carry the spin of the nucleons. The energy released in β decay is much smaller than the nucleon masses; thus we can take the non-relativistic limit of Equations (2.7) and (2.8). The overall nuclear wavefunctions are then:

$$\psi_X \xrightarrow[E_p \ll m_p]{} \sqrt{2E_p}\begin{pmatrix} \chi_s \\ 0 \end{pmatrix} e^{-iE_p t}\,\psi_{\rm nucl}\,\psi_{\rm iso} \tag{2.9}$$

$$\overline{\psi}_Y \xrightarrow[E_n \ll m_n]{} \overline{\psi}'_{\rm iso}\,\overline{\psi}'_{\rm nucl}\sqrt{2E_n}\begin{pmatrix} \chi_r^* & 0 \end{pmatrix} e^{iE_n t} \tag{2.10}$$

Substituting these expressions in Equation (2.4), the hadron current in the non-relativistic limit becomes:

$$\begin{aligned}(j^\mu)_{\rm had} \xrightarrow[E \ll m]{} (j^0)_{\rm had} &= \begin{pmatrix} \chi_r^* & 0 \end{pmatrix}\begin{pmatrix} 1 & \boldsymbol{\sigma} \\ -\boldsymbol{\sigma} & -1 \end{pmatrix}\begin{pmatrix} \chi_s \\ 0 \end{pmatrix}\ \overline{\psi}'_{\rm nucl}\psi_{\rm nucl}\ \left(\overline{\psi}'_{\rm iso}\tau_+\psi_{\rm iso}\right)\ e^{-i(E_p-E_n)t} \\ &= \sqrt{4E_nE_p}\ (\chi_r^*\chi_s)\left(\overline{\psi}'_{\rm nucl}\psi_{\rm nucl}\right)\ e^{-i(E_p-E_n)t}\end{aligned} \tag{2.11}$$

†Following the convention of Halzen and Martin [1].

Note that in this limit, only the $\mu = 0$ (time) component of γ^μ contributes to the matrix element. The spatial components, responsible for leaving the neutron in a spin state different from that of the proton, do not contribute in Fermi's vector model of β decay.

The leptons are naturally assigned Dirac wavefunctions, but in this case the non-relativistic reduction is not valid. We only need the time component of the current as for the hadrons, so the lepton current is

$$\begin{aligned}(j_0)_{lep} &= \overline{u}_{\nu_e}\, e^{ip_{\nu_e}\cdot x}\ \gamma_0\ v_e\, e^{ip_e\cdot x} \\ &= u^\dagger_{\nu_e}\, v_e\, e^{i(E_{\nu_e}+E_e)t}\, e^{-i(\boldsymbol{p}_{\nu_e}+\boldsymbol{p}_e)\cdot\boldsymbol{x}}\end{aligned} \tag{2.12}$$

where for the sake of generality we do not assume a massless neutrino. β decay energies are on the order of a few MeV and typical nuclear sizes are a few femtometers; therefore, over the nuclear volume, $(\boldsymbol{p}_{\nu_e} + \boldsymbol{p}_e)\cdot\boldsymbol{x} \ll 1$. This allows us to expand the exponential in Equation (2.12) and to keep only the first term (the "allowed approximation"):

$$e^{-i(\boldsymbol{p}_{\nu_e}+\boldsymbol{p}_e)\cdot x} = \underbrace{1}_{\text{allowed}} - \underbrace{i(\boldsymbol{p}_{\nu_e}+\boldsymbol{p}_e)\cdot\boldsymbol{x}}_{1^{\text{st}}\text{ forbidden}} - \underbrace{|(\boldsymbol{p}_{\nu_e}+\boldsymbol{p}_e)\cdot\boldsymbol{x}|^2}_{2^{\text{nd}}\text{ forbidden}} + \ldots \tag{2.13}$$

Physically, the allowed term corresponds to the leptons being created at $x = 0$ with no net orbital angular momentum carried away; any change in nuclear spin must be reflected in the alignment of the spins of the leptons which can be either parallel ($S = 1$) or anti-parallel ($S = 0$). For the Fermi decays we are considering, the lepton spins must be anti-parallel since according to Equation (2.11), the hadron current vanishes if $\chi_r \neq \chi_s$ so there can be no net change in the nuclear spin, I. The lepton spins *can* be parallel in β decay, but in this case the operator is axial-vector, which Fermi did not consider; these are referred to as *Gamow-Teller* decays which have the selection rule $\Delta I = 0, \pm 1$. If $I^\pi = 0^+$ for both the initial and final nuclei (where π refers to their parity), $\Delta I = 0$ but since no orbital angular momentum can be transferred, it must be a 'pure Fermi' decay (no Gamow-Teller components).

The matrix element, Equation (2.2), of Fermi's β^+ decay can now be expressed

as:

$$\mathcal{M}_{fi} = \sqrt{4E_nE_p}\, G_F\, [u^\dagger v]\, e^{-i(E_p - E_n - E_{\nu_e} - E_e)t} \underbrace{\int d^3x \left(\overline{\psi}'_{\rm nucl}\, \psi_{\rm nucl}\right)}_{M_F} \tag{2.14}$$

where M_F is the (Fermi) *nuclear* matrix element of this decay which accounts for the effects of nuclear structure. Our choice of wavefunction normalization corresponds to having $2E$ particles per unit volume, that is $u^\dagger u = v^\dagger v = 2E$, which we use after squaring the matrix element Equation (2.14):

$$\begin{aligned} |\mathcal{M}_{fi}|^2 &= 4E_nE_p\, G_F^2\, [v^\dagger 2E_{\nu_e} v]\, |M_F|^2 \\ &= 16E_nE_pE_{\nu_e}E_e\, G_F^2\, |M_F|^2 \end{aligned} \tag{2.15}$$

This choice of normalization also makes calculating the density of states rather simple: with $2E$ particles, the individual phase space available to a particle in the momentum element $\boldsymbol{p}+d^3\boldsymbol{p}$ is simply $(d^3\boldsymbol{p}/(2\pi)^3)/2E$. On the basis of Equation (2.1), the differential decay rate of ${}^Z_AX \longrightarrow {}^{Z-1}_AY + e^+ + \nu_e$ from rest is

$$dW_{\rm Fermi} = |\mathcal{M}_{fi}|^2 \frac{1}{2E_p} \left[\frac{d^3\boldsymbol{p}_n}{(2\pi)^3 2E_n} \frac{d^3\boldsymbol{p}_{\nu_e}}{(2\pi)^3 2E_{\nu_e}} \frac{d^3\boldsymbol{p}_e}{(2\pi)^3 2E_e}\right] (2\pi)^4 \delta^4(p_p - p_n - p_{\nu_e} - p_e) \tag{2.16}$$

with energy-momentum conservation ensured through the δ^4 function. The matrix element contains the 'physics' of the interaction, but the observed spectrum shape will be dominated by the final state phase space. Letting $E_\circ$ represent the energy released in the decay, substituting Equation (2.15) into Equation (2.16), and using the relation $p^2dp = p^2\frac{E}{p}dE$ for both the electron and the neutrino gives

$$dW_{\rm Fermi} = \frac{G_F^2}{(2\pi)^5} |M_F|^2\; p_eE_e dE_e d\Omega_e\; p_{\nu_e}E_{\nu_e} dE_{\nu_e} \Omega_{\nu_e}\; \delta(E_\circ - E_e - E_{\nu_e}) \tag{2.17}$$

Finally, we use the δ function to integrate over dE_{ν_e} so that we end up with the decay rate:

$$\frac{dW_{\rm Fermi}}{dE_e d\Omega_e d\Omega_{\nu_e}} = \frac{G_F^2}{(2\pi)^5} p_eE_e(E_\circ - E_e) \left[(E_\circ - E_e)^2 - m_{\nu_e}^2\right]^{\frac{1}{2}} F(E_e, Z', R) |M_F|^2 \tag{2.18}$$

The additional 'Fermi factor', $F(E_e, Z', R)$, accounts for Coulomb interactions between the emitted positron and daughter nucleus. Fermi derived an analytic expression for this function when he first proposed his theory [6]:

$$F(E_e, Z', R) = 4(2p_eR)^{2(s-1)} e^{\pi\eta} \frac{|\Gamma(s+i\eta)|^2}{|\Gamma(1+2s)|^2} \tag{2.19}$$

where $s = \sqrt{1-\alpha^2 Z'^2}$, $\eta = \pm E_e/p_e$ and R is the nuclear radius taken to be $1.2\,A^{1/3}$ fm. $\alpha = e^2/4\pi$ is the fine structure constant and Z' refers to the daughter nucleus. Due to the difficulty of evaluating the complex Γ function, Fermi used a non-relativistic approximation but since we now have computers to aid us, Equation 2.19 is used in calculations throughout this thesis.

Although Fermi's theory worked very well, there were still problems (specifically with the decay of the kaon system) which prompted Lee and Yang [7] to question whether parity was strictly conserved as required by a purely vector coupling. There were, after all, four other types of interactions (Table 2.1) which Fermi could choose from, and some do not conserve parity. Madame Wu's experiments with polarized ^{60}Co, as well as more accurate experiments that followed, indicate that parity is *maximally* violated in weak interactions. The form of the weak operator as presently understood is $V - A$; it is the (equally large) axial-vector component which allows Gamow-Teller decays.

2.2 A Generalized Interaction

Modern particle physics is based on quantum field theory in which the forces are mediated by the exchange of particles, the quanta of the field. The electromagnetic force, for example, is mediated by the emission and absorption of its quantized field, the photon. For the weak force, there are three *massive* bosons: the $W^{\pm}$ which carry one unit of electric charge and the Z^0 which mediates weak neutral currents. The weak coupling constant, g_w, is related to Fermi's constant by

$$G_F = \frac{\sqrt{2}g_w^2}{8M_W^2} \tag{2.20}$$

and gives the relative strength of the weak force. The mass of the $W^{\pm}$ has been measured [5] to be 80.41 ± 0.10 GeV so that $g_w \approx 0.653$ is *greater* than the corresponding

constant for the electromagnetic force, $g_e = \sqrt{4\pi\alpha} \approx 0.303$. Indeed, the only reason this force is 'weak' compared to that of electromagnetism is because of the large mass of the propagator.

If we limit ourselves to pure Fermi decays (ones where there are no Gamow-Teller components in the matrix element), then the axial vector component of the weak interaction vanishes as mentioned earlier. Similarly, the pseudo-scalar and tensor components do not contribute. Consequently, we only have to consider vector and scalar interactions; with only Lorentz invariance required, Figure 2.2 shows their Feynman diagrams. The strength of each interaction type is reflected in the lepton vertex parameters, $C_{S,V}$ and $C'_{S,V}$, which must be determined experimentally. The S stands for a scalar current and the V for vector; the primed parameters allow for parity non-conservation in the lepton current, while time-reversal invariance is assured only if all the parameters are real. We furthermore assume for simplicity that the scalar coupling constant is the same as the vector, and that the scalar boson's mass is the same as the charged W.

In the limit that the momentum transfer, k, is small compared to the W mass (applicable to β decay), the propagators reduce to constants: $\frac{ig_{\mu\nu}}{M_W^2}$ (vector) and $\frac{-i}{M_W^2}$ (scalar). It is for this reason that Fermi's contact approximation worked so well: the mass of the W makes the interaction extremely short-ranged (on the order of

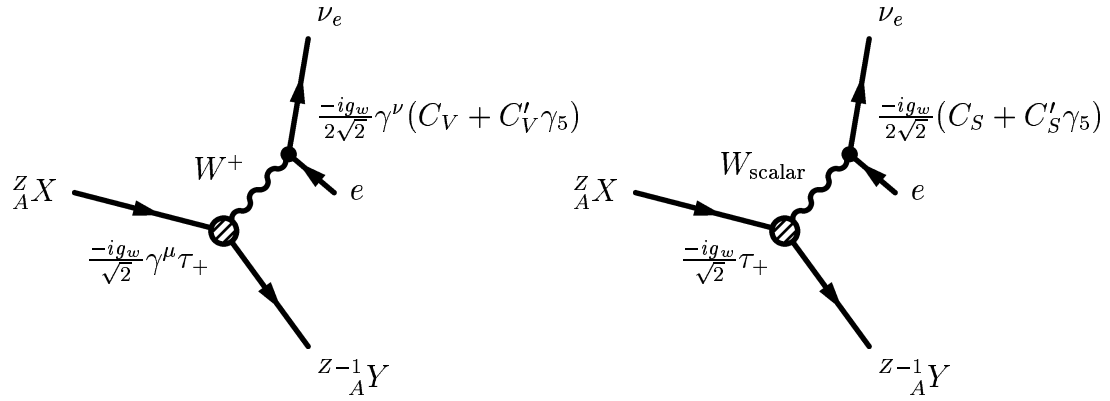

(a) vector propagator: $\frac{-i\left(g_{\mu\nu} - k_\mu k_\nu / M_W^2\right)}{k^2 - M_W^2}$ (b) scalar propagator: $\frac{-i}{k^2 - M_W^2}$

FIGURE 2.2: General Feynman diagrams for the $0^+ \longrightarrow 0^+$ β^+ decay of ${}^Z_A X \longrightarrow {}^{Z-1}_A Y + e^+ + \nu_e$ as mediated by a massive boson. The expressions for the propagators for both the vector and scalar interactions are given below their diagrams.

$1/M_W \approx 0.003$ fm). The interactions depicted in the diagrams of Figure 2.2 are (with the same limits/approximations as in §2.1):

$$\mathcal{M}_V = \sqrt{4E_pE_n}M_F\frac{g_w^2}{4M_W^2}\ g_{0\nu}\overline{u}_{\nu_e}\gamma^\nu(C_V + C_V'\gamma_5)v_e \tag{2.21}$$

$$\mathcal{M}_S = \sqrt{4E_pE_n}M_F\frac{-g_w^2}{4M_W^2}\ \overline{u}_{\nu_e}(C_S + C_S'\gamma_5)v_e \tag{2.22}$$

Note that in the non-relativistic limit, the hadron current is the same for vector interactions as it is for scalar.

The final matrix element is $\mathcal{M}_{fi} = \mathcal{M}_V + \mathcal{M}_S$ which, after squaring and evaluating the traces, yields three terms:

$$|\mathcal{M}_V|^2 = 16E_pE_nE_eE_{\nu_e}G_F^2\left[(|C_V|^2+|C_V'|^2)\left(1+\frac{\boldsymbol{p}_e\cdot\boldsymbol{p}_{\nu_e}}{E_eE_{\nu_e}}\right) - (|C_V|^2-|C_V'|^2)\frac{m_em_{\nu_e}}{E_eE_{\nu_e}}\right] \tag{2.23a}$$

$$|\mathcal{M}_S|^2 = 16E_pE_nE_eE_{\nu_e}G_F^2\left[(|C_S|^2+|C_S'|^2)\left(1-\frac{\boldsymbol{p}_e\cdot\boldsymbol{p}_{\nu_e}}{E_eE_{\nu_e}}\right) - (|C_S|^2-|C_S'|^2)\frac{m_em_{\nu_e}}{E_eE_{\nu_e}}\right] \tag{2.23b}$$

$$\mathcal{M}_V^\dagger\mathcal{M}_S + \mathcal{M}_S^\dagger\mathcal{M}_V = 16E_pE_nE_eE_{\nu_e}G_F^2\left[2\Re\mathrm{e}(C_VC_S^* - C_V'C_S'^*)\frac{m_{\nu_e}}{E_{\nu_e}} - 2\Re\mathrm{e}(C_VC_S^* + C_V'C_S'^*)\frac{m_e}{E_e}\right] \tag{2.23c}$$

Insertion of these equations into Equation (2.16) and continuing the same calculation yields the generalization of (2.18), the decay rate for vector and/or scalar interactions where massive bosons propagate the force:

$$\frac{dW}{dE_ed\Omega_ed\Omega_{\nu_e}} = \frac{G_F^2}{(2\pi)^5}p_eE_e(E_\circ - E_e)\left[(E_\circ - E_e)^2 - m_{\nu_e}^2\right]^{\frac{1}{2}}\ F(E_e, Z', R) \times \xi\left[1 + a\frac{\boldsymbol{p_e}\cdot\boldsymbol{p}_{\nu_e}}{E_eE_{\nu_e}} + b_{\nu_e}\frac{m_{\nu_e}}{E_{\nu_e}} + b_e\frac{m_e}{E_e} + b_{e\nu}\frac{m_em_{\nu_e}}{E_eE_{\nu_e}}\right] \tag{2.24}$$

The decay rate of Fermi's model is effectively renormalized by

$$\xi = |M_F|^2\left[|C_S|^2+|C_S'|^2+|C_V|^2+|C_V'|^2\right] \tag{2.25}$$

and the other parameters are defined as:

$$a = \frac{-|C_S|^2-|C'_S|^2 + |C_V|^2+|C'_V|^2}{|C_S|^2+|C'_S|^2 + |C_V|^2+|C'_V|^2} \qquad (2.26)$$

$$b_e = \frac{-2\Re\mathrm{e}(C^*_S C_V + C'^*_S C'_V)}{|C_S|^2+|C'_S|^2 + |C_V|^2+|C'_V|^2} \qquad (2.27)$$

$$b_{\nu_e} = \frac{2\Re\mathrm{e}(C^*_S C_V - C'^*_S C'_V)}{|C_S|^2+|C'_S|^2 + |C_V|^2+|C'_V|^2} \qquad (2.28)$$

$$b_{e\nu} = \frac{-|C_S|^2+|C'_S|^2 - |C_V|^2+|C'_V|^2}{|C_S|^2+|C'_S|^2 + |C_V|^2+|C'_V|^2} \qquad (2.29)$$

In the Standard Model, $C_S = C'_S = 0$ and $C_V = C'_V$ so that for $0^+ \longrightarrow 0^+$ decays, it predicts that the $\beta - \nu$ correlation parameter $a = 1$. If instead the weak interaction is mediated by a scalar boson (i.e. $C_S = C'_S$ and $C_V = C'_V = 0$), then the correlation parameter is equal to -1; in this manner, a precise measurement of a provides a very sensitive test of possible scalar currents in weak interactions. A determination of a to within $\pm 0.5\%$ would be complementary to more direct high-energy searches [8, 9]. The best measurement to date is of $\tilde{a} \equiv \frac{a}{1+b_e\langle m_e/E_e\rangle} = 0.9989 \pm 0.0052\,\mathrm{stat} \pm 0.0039\,\mathrm{sys}$ [10] from a detailed measurement of the energy spectrum of β delayed protons from the pure Fermi decay of $^{32}\mathrm{Ar}(0^+, T = 2)$ to the lowest $0^+, T = 2$ excited state of $^{32}\mathrm{Cl}$.

The b_e and b_{ν_e} parameters are the amplitudes of the Fierz interference terms which arise from the $\mathcal{M}^\dagger_V \mathcal{M}_S + \mathcal{M}^\dagger_S \mathcal{M}_V$ cross terms in the matrix element; $b_{e\nu}$ represents an interference between the electron and neutrino wavefunctions within each of the vector and scalar interactions. The b_{ν_e} and $b_{e\nu}$ terms are negligibly small (indeed, possibly zero) since $m_{\nu_e} \ll E_{\nu_e}$, but are included for completeness and to expose the symmetry. A limit of $|b_e| \leq 0.007$ has been independently placed using measurements of the $\mathcal{F}t$ values of $0^+ \longrightarrow 0^+$ decays [11].

Jackson, Trieman and Wyld [12] were the first to calculate the general decay rate Equation (2.24) for allowed β-decays (including mixed Fermi/Gamow-Teller transitions). Their calculations assume a massless neutrino and so do not include the b_{ν_e} and $b_{e\nu}$ terms. They do, however, include Coulomb corrections [13] which adds a $\frac{2\alpha Z m_e}{p_e}\Im m(C_S C^*_V + C'_S C'^*_V)/\left[|C_S|^2+|C'_S|^2+|C_V|^2+|C'_V|^2\right]$ term to a and multiplies b_e by the relativistic factor $\sqrt{1-\alpha^2 Z'^2}$.

Chapter 3

The $\beta - \nu$ Correlation Experiment

The β^+ decay of the isomeric state of potassium-38 is one of the approximately twenty known cases of strong $0^+ \longrightarrow 0^+$ decays that Nature has offered us and, as an alkali atom, is perfectly suited for neutral atom traps. The decay $^{38m}\mathrm{K} \longrightarrow ^{38}\mathrm{Ar} + e^+ + \nu_e$ from a trap provides us with an excellent laboratory with which to search for scalar currents.

This chapter is meant to provide some details specific to TRINAT's $\beta - \nu$ correlation experiment. The first section explains how the observables of the decay in the back-to-back geometry can be used to determine a. Following this is a brief introduction to neutral atom traps, TRINAT's double-trap system and how we get our radioactive potassium. An overview of our detection system as a whole is given in the final section which primarily deals with the recoil detector since the β-telescope is the focus of Chapter 4.

3.1 Using ^{38m}K to measure a

The decay schemes for both the isomer and ground state [14] are given in Figure 3.1. The ^{38m}K decay is a pure Fermi transition with a branching ratio measured [15] to be $> 99.998\%$ and a Q-value[†] of 5.02234(12) MeV [16]. The ^{38}K decay is also given because ISAC's mass analyzer (see §3.2.2) cannot iso*merically* differentiate between the ground state and ^{38m}K, making us susceptible to the ground state's γ background.

In what follows, let us consider observing the decay from a point-like source in

[†]For β^+ decay, $Q = E_\circ - m_e c^2$.

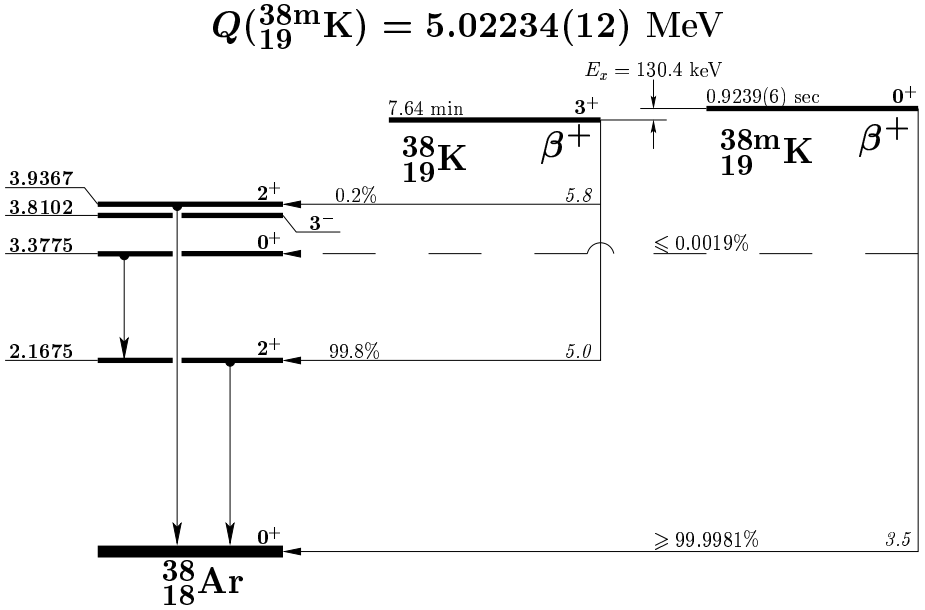

FIGURE 3.1: Nuclear energy levels for ^{38m}K. The superallowed β^+ decay ($\log ft = 3.5$) is by far the most favoured branch for the isomer. The ground state's β^+ decay feeds the 2^+ state resulting in a 2.17 MeV γ.

the back-to-back geometry where the positron is emitted opposite the recoil. The neutrino may be emitted either (a) parallel to the β or (b) parallel to the recoil. The kinematics of the decay will be different for the two cases as shown in Figure 3.2; this is a plot of the recoil's time-of-flight (TOF) against the positron's (kinetic) energy. The recoil TOF is the observable used in the correlation experiment (along with the position of the event) to determine the recoil momentum, so we use the TOF here for consistency. The TOF is nearly independent of β energy in the fast branch (case (a)) because the recoil velocity is not seriously affected by how the leptons share the rest of the available energy: the recoil velocity is $[E_\circ - E_e(1 - v_e/c)]\, c/M_{\mathrm{Ar}}c^2$, which is a constant to order $(1 - v_e/c)$. In the slow branch (case (b)), it is the recoil which is sharing momentum with the neutrino, and in this case the kinematics yield $v_{\mathrm{Ar}}/c = [E_e(1 + v_e/c) - E_\circ]\, /M_{\mathrm{Ar}}c^2$. The β's energy in the asymptotic limit of the slow branch is defined by the relation: $T_e + p_e c = Q$.

The generalized decay rate, Equation (2.24), shows how the population of the two branches depends on the form of the weak propagator: if purely vector (as in the

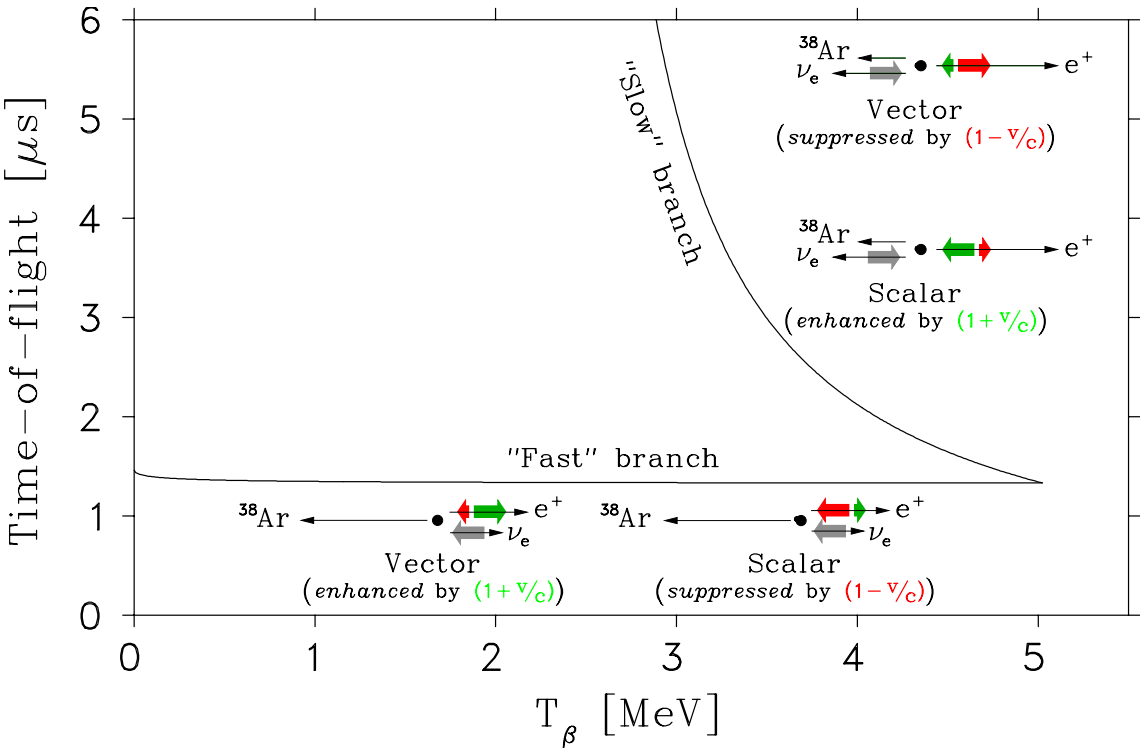

FIGURE 3.2: Recoil time-of-flight vs. β energy for Ar^0 in the back-to-back geometry. For this discussion, we take the neutrino to always be left-handed with helicity $= -1$ as shown and, depending on the interaction type, the positron is preferentially emitted with either equal (scalar) or opposite (vector) helicity. The slow and fast branches are either enhanced or suppressed since the total lepton spin must add up to zero.

Standard Model), $a = +1$ so that the fast branch ($\hat{p}_e \cdot \hat{p}_\nu = \cos\theta_{\beta\nu} = 1$) is enhanced[†] by $1 + v_e/c \lesssim 2$, whereas scalar interactions ($a = -1$) are suppressed[†] by $1 - v_e/c \gtrsim 0$. In the slow branch, $\cos\theta_{\beta\nu} = -1$ so the situation is reversed, and this time it is the scalar currents which are enhanced (with the vector suppressed). In this way, the back-to-back geometry is the most sensitive geometry with which to search for weak scalar bosons.

The enhancement and suppression of the two branches can be understood physically in terms of the outgoing lepton helicities. Helicity is defined as the projection of a particle's spin, $\mathbf{\Sigma}$, along its direction of motion. The projection operators, $\frac{1}{2}(1 \pm \gamma^5)$, can be used to pick out a particle's helicity, i.e. for the (presently assumed massless) neutrino, we can project out its left- and right-handed components:

$$u_\nu = \underbrace{\frac{1}{2}(1-\gamma^5)u_\nu}_{\equiv\, u_\nu^L} + \underbrace{\frac{1}{2}(1+\gamma^5)u_\nu}_{\equiv\, u_\nu^R} \tag{3.1}$$

These chiral states are helicity eigenstates with eigenvalues $+1$ (right) or -1 (left). For particles with mass, however, this is only true in the relativistic limit since [17],

$$\mathbf{\Sigma}\cdot\hat{p}\;\psi_\pm = \pm\gamma^5 \begin{pmatrix} \frac{E-mc^2}{|\boldsymbol{p}|c} & 0 \\ 0 & \frac{E+mc^2}{|\boldsymbol{p}|c} \end{pmatrix} \psi_\pm \underset{E\gg mc^2}{\approx} \gamma^5\psi_\pm \tag{3.2}$$

where ψ_+ represents a particle (u) and ψ_- an anti-particle (v). Note that for massless particles *only*, helicity and handedness can be used interchangeably; a left-handed neutrino will always have negative helicity. A left-handed massive particle on the other hand *predominantly* carries negative helicity, but a component that goes like $(1 - \frac{pc}{E})$ in the relativistic limit has the 'wrong' (positive) helicity.

To see how this affects the ^{38m}K decay, let us for the sake of clarity take the neutrino to be only left-handed so that the scalar current of Figure 2.2 (on page 12) then becomes $\frac{-ig_w}{2\sqrt{2}}\overline{u}_\nu^L(C_S + C_S'\gamma^5)v_e$. The γ^5 of the projection operator anti-commutes with the γ^0 in the adjoint, so $\overline{u}^L = \overline{u}\frac{1}{2}(1+\gamma^5)$ and the current can be seen to only

[†]Neglecting the negligible (but conceivably possible) contribution from the $b_{e\nu}$ term.

couple left-handed neutrinos to left-handed positrons:

$$(j)^S_{\rm lep} = \frac{-ig_w}{2\sqrt{2}}\overline{u}_\nu(C_S + C'_S\gamma^5)\underbrace{\frac{1}{2}(1+\gamma^5)v_e}_{\equiv\, v_e^L} \tag{3.3}$$

Similarly, right-handed neutrinos only couple to right-handed positrons so that for scalar interactions, the leptons are emitted with the same handedness. In the limit of zero mass, their helicities are equal; the positron *may* have the wrong helicity, but this is suppressed because it is relativistic and so the approximation in Equation (3.2) is very good.

The vector current of Figure 2.2 contains a γ^μ at the vertex, which anti-commutes with the γ^5 and so changes the positron projection. A left-handed neutrino in this case couples only to a *right*-handed positron (and a right-handed ν to a left-handed e^+). Vector interactions, therefore, differ from scalar interactions because the leptons are emitted with opposite helicities.

As mentioned earlier, the spins of the leptons in a $0^+ \longrightarrow 0^+$ decay must add up to zero. Returning to Figure 3.2 (which depicts the lepton spins as fat arrows for each of the four decay possibilities), it is easy to see how the fast and slow branches are affected by the type of interaction. In the fast branch, the right-handed positron (resulting from a Standard Model vector boson propagator) naturally has a spin opposite to that of the neutrino's, and so is allowed. In the scalar case, the dominant spin of the left-handed positron is aligned with the neutrino's which is forbidden; the positron would have to have the wrong helicity to be in the fast branch (depicted as the shorter of the two electron spin arrows). Similarly, the slow branch favours the leptons carrying equal helicity since in this case the neutrino's momentum is opposite the positron's.

TRINAT will determine a by simultaneously fitting the recoil TOF spectra for a number of β energy bins to detailed Monte Carlo simulations. The shape of these spectra will depend on the ratio of slow to fast branch events and hence a. The $\beta - \nu$ correlation experiment and the analysis of its results is largely a part of A. Gorelov's Ph.D. and so the interested reader is referred to his thesis [18].

3.2 Trapping Techniques

Ever since the first successful experiment where neutral atoms were trapped using lasers and magnetic fields [19], the use of magneto-optical traps (MOTs) has become widespread in many fields of physics. The ability to observe radioactive decays from such traps opens up new possibilities in precision β decay experiments. The MOT (*i*) confines the decays to occur within a compact (≈ 1 mm^3) trap volume, (*ii*) cools the atoms to temperatures at or below the mK level, and (*iii*) allows distortion-free detection of the daughter particles' momenta because of the negligible source thickness.

3.2.1 The Neutral Atom Trap

A unique feature of magneto-optic traps is that their force is dependent upon the atom's position as well its velocity; much like a spring, the positional force returns atoms back to a common centre while the latter adds a damping effect, as if the spring was submerged in a viscous liquid. A laser field generates the velocity-dependent force which cools the atoms in an optical molasses, while a polarized laser field and an applied magnetic field adds the positional dependence needed to actually confine them.

Initially, if one considers how small the incident photon's momentum, $\hbar\boldsymbol{k}$, is compared to that of thermal atoms, a trap based on the light forces from a laser beam seems futile. For example, the $S_{1/2} \rightarrow P_{3/2}$ (D_2) transition in ^{38m}K has a wavelength of $\lambda = 766.5$ nm so that $p_{\text{phot}} \approx 1.5$ eV/c while the atom's thermal momentum is typically 45 keV/c. In addition, when the atom decays from the excited state via stimulated emission, this small momentum kick is nullified since the atom will recoil by $-\hbar\boldsymbol{k}$ if the photon is emitted coherently. Spontaneous emission, on the other hand, emits photons homogeneously into 4π so that, at least on average, there will be a net momentum transfer in the direction of the incident photon. Clearly, the atoms must absorb and spontaneously emit many photons if one hopes to optically trap them.

Alkali atoms are well-suited for neutral atom traps because they have a simple electronic configuration; the ns^1 valence electron alone determines the fine and hyperfine structures of the atom since all other electrons are in closed (noble gas) shells.

The atomic angular momentum, $\boldsymbol{J} = \boldsymbol{S} + \boldsymbol{L}$, and nuclear spin, $\boldsymbol{I}$, of an atom are a coupled system, so the good quantum states are $|F, m_F\rangle$ where $\boldsymbol{F} = \boldsymbol{J} + \boldsymbol{I}$. The transition from the $F = I + \frac{1}{2}$ ground ($S_{1/2}$) state to the $F' = I + \frac{3}{2}$ excited ($P_{3/2}$) state *cannot* decay back into the other $F = I - \frac{1}{2}$ ground state since the photon carries one unit of angular momentum; the atom must return to the same $F = I + \frac{1}{2}$ ground state where it started. This 'cycling transition' allows an atom to absorb many photons from the same laser beam so that the light forces can build up and significantly affect the atom's motion. The cycling is not perfect due to off-resonant transitions and finite linewidths, and so atoms may be optically pumped into the $F = I - \frac{1}{2}$ state where they will no longer be in resonance with the laser light. Atoms in this 'dark' state are not trapped, so to transfer them back into the cycling transition, a 'repumping' laser is tuned to the $F = I - \frac{1}{2} \rightarrow F' = I + \frac{1}{2}$ transition.

It is worth noting at this time that for ^{38m}K, $I = 0$ which simplifies the atomic energy levels; there is no hyperfine structure in an atom with no nuclear spin. In this case, there is no need for the repumping laser.

Doppler Cooling

Consider the effect on an alkali atom that is placed within a laser field generated by two identical, counter-propagating laser beams detuned Δ MHz below the atomic resonance, ω_{A}. Thermal atoms will have a Maxwellian velocity distribution in all directions and, due to the Doppler effect, will be affected by each beam differently. An atom moving collinear with one of the laser beams will see the light red-shifted *farther* below resonance by a factor v_{atom}/c while the counter-propagating beam will be blue-shifted *closer* to resonance. The atom will preferentially absorb photons from the laser beam that is against the atom's direction of motion and, with each absorption, the atom's momentum is reduced. It is in this way that the atoms are cooled.

It can be shown [20] that the force in an optical molasses is proportional to the velocity if (i) the Doppler shift isn't too large and (ii) the laser intensity, I_L, isn't strong enough to induce stimulated emission. Letting $\omega_L = \omega_A - \Delta$ represent the

frequency of the laser light, the Doppler force is:

$$\boldsymbol{F}_D(\boldsymbol{v}) \approx \frac{8\hbar k^2 \Delta \; I_L/I_{\rm sat}}{\Gamma(1 + \frac{4\Delta^2}{\Gamma^2} + \frac{I_L}{I_{\rm sat}})^2} \; \boldsymbol{v} \tag{3.4}$$

where $\Gamma = 1/\tau$ is the transition linewidth and $I_{\rm sat} = \frac{h\pi c\Gamma}{3\lambda^3}$ is the saturation intensity.

The transition linewidth ends up being this force's limiting factor; in a simple model [20], the coldest temperature attainable is $T_{\rm D} = \hbar\Gamma/2k_{\rm B}$ where $k_{\rm B}$ is Boltzmann's constant. In the case of ^{38m}K for which $\tau = 26$ ns, this 'Doppler limit' is 150 μK.

The Magneto-Optic Trap

An atom with magnetic moment $\boldsymbol{\mu}$ subject to a magnetic field, $\boldsymbol{B}$, will remove the m_F degeneracy and Zeeman split the $|F, m_F\rangle$ energy levels according to

$$E_{F,m_F} \underset{g_I \ll g_J}{\approx} g_J \frac{F(F+1) + J(J+1) - I(I+1)}{2F(F+1)} m_F \mu_B B \tag{3.5}$$

where g_J is the (atomic) Landé g-factor and $\mu_B = e\hbar/2m_e$ is the Bohr magneton. If we apply a linear magnetic field, $B_z = B_\circ z$, to atoms in an optical molasses (Figure 3.3 depicts this for the 1-D case), the Zeeman effect will provide us with a position-dependent force: the energy level shifts (hence the transition frequency and scattering rate) will be proportional to the distance from $z = 0$. An atom at $z > 0$ will have its $|\frac{1}{2}\ \frac{1}{2}\rangle \longrightarrow |\frac{3}{2}\ \frac{-1}{2}\rangle$ transition shifted closer to the laser frequency. The two counter-propagating beams are distinguished by their polarizations; the $\Delta m_F = -1$ transition can only be driven by the σ^- beam, so the atom feels a net force acting towards the left. Similarly, atoms at $z < 0$ will preferentially absorb the σ^+ light through the $|\frac{1}{2}\ \frac{-1}{2}\rangle \longrightarrow |\frac{3}{2}\ \frac{1}{2}\rangle$ transition and be pushed back towards centre. If the laser field does not have perfect polarization, the atom can absorb photons from the wrong beam and will be heated rather than cooled. Thus, the quality of the circular polarization of the laser light is very important.

The magneto-optic force is a combination of the Doppler force with effects induced by the Zeeman shift. The trap centre is defined at $z = 0$ where the magnetic field changes sign. If we let $\xi = kv + \beta z$ where βz represents the Zeeman effect on the

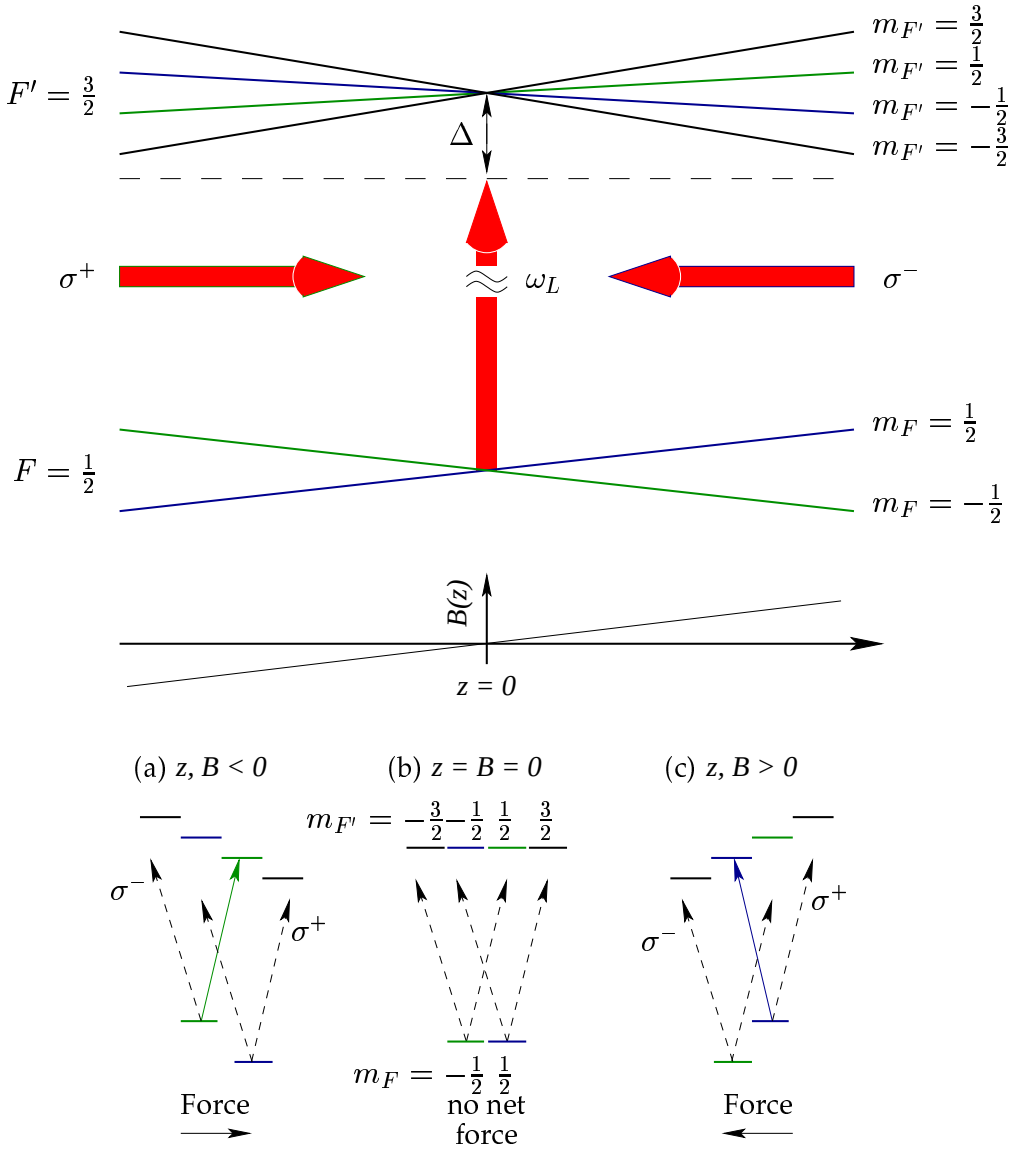

FIGURE 3.3: Atomic energy levels and Zeeman shifts of ^{38m}K in a one dimensional magneto-optic trap. The shift of the energy levels depends linearly on the magnetic field (for weak fields) giving a positional dependent force. The trapping arises because of preferential scattering off the laser that is shifted closer to resonance, depicted by the solid lines arising from σ^+ light in (a) and σ^- in (c); the force in either case pushes atoms towards $z = 0$. Both laser beams are equally off resonant at the trap centre (b) so neither is preferentially absorbed and the atom feels no net force.

transition frequency, then the overall magneto-optic force is [21]

$$F_{\mathrm{MOT}}(r,v) = \frac{\hbar k \Gamma}{2}\left[\frac{I_L/I_{\mathrm{sat}}}{1+\frac{I_L}{I_{\mathrm{sat}}}+\frac{4(\Delta-\xi)^2}{\Gamma^2}} - \frac{I_L/I_{\mathrm{sat}}}{1+\frac{I_L}{I_{\mathrm{sat}}}+\frac{4(\Delta+\xi)^2}{\Gamma^2}}\right] \tag{3.6}$$

It can be shown that [22], for small detunings, this force is proportional to ξ so that the trapped atoms behave like a simple, damped harmonic oscillator.

The generalization to three dimensions requires a magnetic field that is zero at the centre and which increases linearly with distance from there; this is generally accomplished using a quadrupole field generated by two coils in the anti-Helmholtz configuration. With six laser beams oriented along the axes as depicted in Figure 3.4, forces similar to those of the 1D case are present no matter which direction an atom within the trapping volume is travelling.

Typically, MOTs are not very deep and so considerable effort is needed to efficiently load them. The most popular method is known as the vapour-cell MOT [19] and it uses the fact that a MOT *can* capture the low-energy tail of the Maxwell-Boltzmann distribution of velocities. The cell which defines the trapping volume can be specially coated [23] so that atoms tend to bounce off the wall rather than (permanently) chemisorbing to it. When they bounce (physisorb), the atoms re-thermalize (repopulating the whole Maxwell-Boltzmann distribution) and are able to be trapped by the MOT again. The many repeated opportunities for capture allow this method of loading the MOT to have efficiencies on the order of several percent.

3.2.2 TRIUMF's Radioactive Potassium Source

TRIUMF has long been interested in developing radioactive ion beams (RIBs) because they offer the ability to study nuclei away from the valley of stability. The copious production of exotic nuclei delivered with low kinetic energy has already been used by TRINAT as well as an experiment measuring the transition probabilities of superallowed decays which will test the conserved vector current hypothesis [24]; future planned experiments at TRIUMF's RIB include magnetic moment measurements using the Low Temperature Nuclear Orientation facility [25] as well as studies using a polarized ^{8}Li beam [26]. Medium-energy (0.15-1.5 MeV/u; A<30) RIBs are important

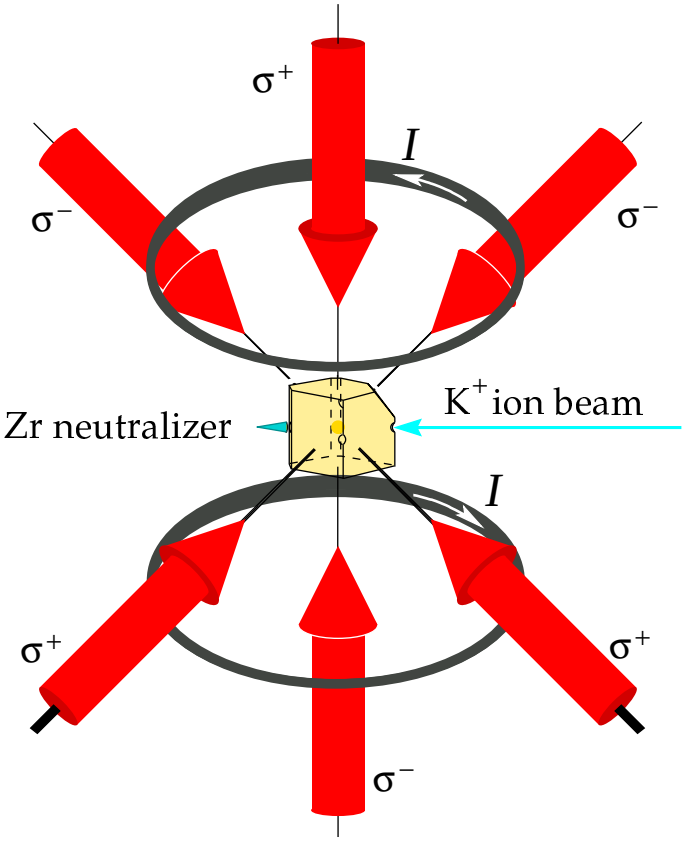

FIGURE 3.4: Schematic diagram of a vapour-cell MOT with an ion beam catcher and neutralizer. ISAC provides us with a potassium ion beam which is neutralized in the hot Zr cone. The atoms then diffuse out into the vapour-cell MOT and the ones in the low-energy tail of the velocity distribution are able to be trapped in the MOT. The quartz cube defines the trapping volume and is coated with SC-77 Dryfilm [23] so as to maximize the number of bounces off the walls and increase the trapping efficiency.

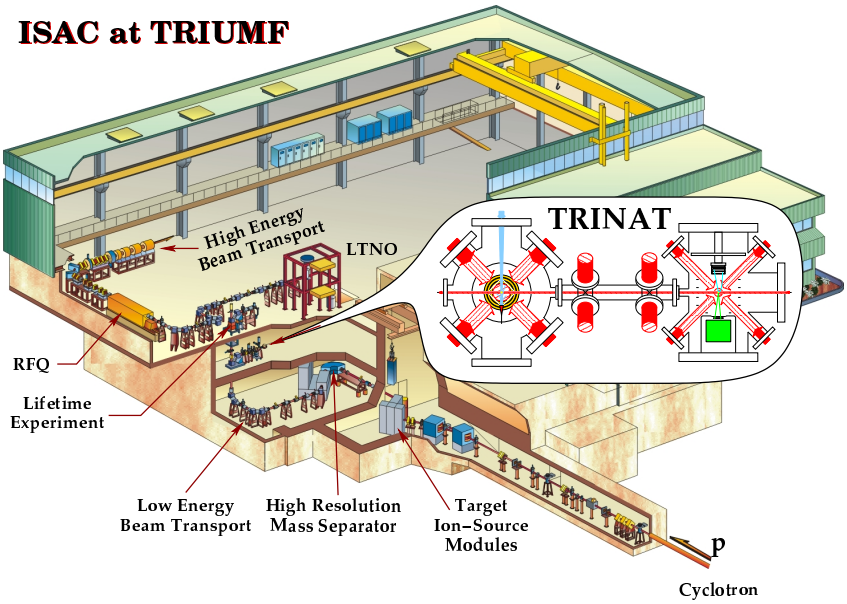

FIGURE 3.5: The ISAC radioactive beam facility at TRIUMF. The 500 MeV protons bombard a CaO target, producing a variety of isotopes; a potassium beam is extracted and filtered through a mass spectrometer before being transported to the TRINAT laboratory.

for nuclear astrophysics because theoretical calculations of stellar processes require measurements of certain nuclear cross-sections that affect key stellar cycles [27, 28].

A test facility, TISOL [29, 30], based on the ISOL facility at CERN-ISOLDE [31] has been operational since 1987 to provide low energy RIBs as well as to develop a robust target-ion source. The $200 - 500$ MeV protons from TRIUMF's high intensity ($150\ \mu$A) cyclotron provide an excellent production beam with which to bombard thick targets, and TISOL has proven that a wide variety of radioactive nuclei can be efficiently produced (500 MeV protons; 1 μA current). Ion beams were extracted from the target at $6 - 12$ keV, and transported to a magnetic analyzer (mass resolution $M/\Delta M = 1\,600$) that had a bend angle of 90° to provide a clean, tunable beam of radioactive isotopes to the experimental area. TRINAT was able to successfully couple TISOL's RIB to a MOT, continuously trapping 2 000 atoms of ^{37}K ($t_{1/2} = 1.23$ s) and 5 000 of ^{38m}K. From this, the viability of the correlation experiment was proven and measurements were made of the isotope shifts [32] in potassium as well as charge-state distributions of daughter atoms in β decay [33, 34].

Isotope	Intensity
^{37}K	1×10^7 ions/sec
^{38m}K	2×10^7 ions/sec
^{38}K (bkgd)	5×10^8 ions/sec

TABLE 3.1: ISAC radioactive beam intensities.

The success of TISOL and the experience gained in developing it has enabled TRIUMF to successfully build a large scale radioactive beam facility: ISAC (the Isotope Separator and ACcelerator). A schematic diagram of the new beam facility is given in Figure 3.5. The general idea is the same as for TISOL, but the new surface ion source can handle more intense production beams (1 μA in June, 1999; currently 10 μA and up to 100 μA in the future) and the ions can be extracted between $12-60$ keV. ISAC's mass analyzer consists of a low-resolution pre-separator followed by the former Chalk River mass separator [35] which has a mass resolution of $\geq 5\,000$. The isotopically selected RIB is then transported to the various experimental areas; in the case of TRINAT, the beam is deposited into a conical zirconium foil as indicated in Figure 3.4.

ISAC's first radioactive beams, ^{37,38m}K, were produced on November 30, 1998. By TRINAT's June 1999 run, ISAC had already demonstrated the ability to produce these beams with intensities comparable to those attained at TISOL (see Table 3.1). The vapour-cell MOT of Figure 3.4 allows an efficient loading of atoms into the trap, but is completely incompatible with observing the recoil of the decays. Efficient loading of an open MOT can be obtained by carefully transporting atoms already trapped in the vapour-cell MOT; this system is outlined in the next section.

3.2.3 TRINAT's Double MOT System

In order to reduce backgrounds as well as to iso*merically* differentiate between ^{38}K and ^{38m}K, a double-MOT system is utilized (see Figure 3.6). The first 'collection trap' is a vapour-cell MOT that traps the potassium atoms once they diffuse out of the hot Zr neutralizer (which is based on the Los Alamos scheme [36]). The laser linewidth is small enough to resolve the different fine structure of the isomer and ground state, so only the isomer is trapped. The cold, trapped ^{38m}K atoms at the

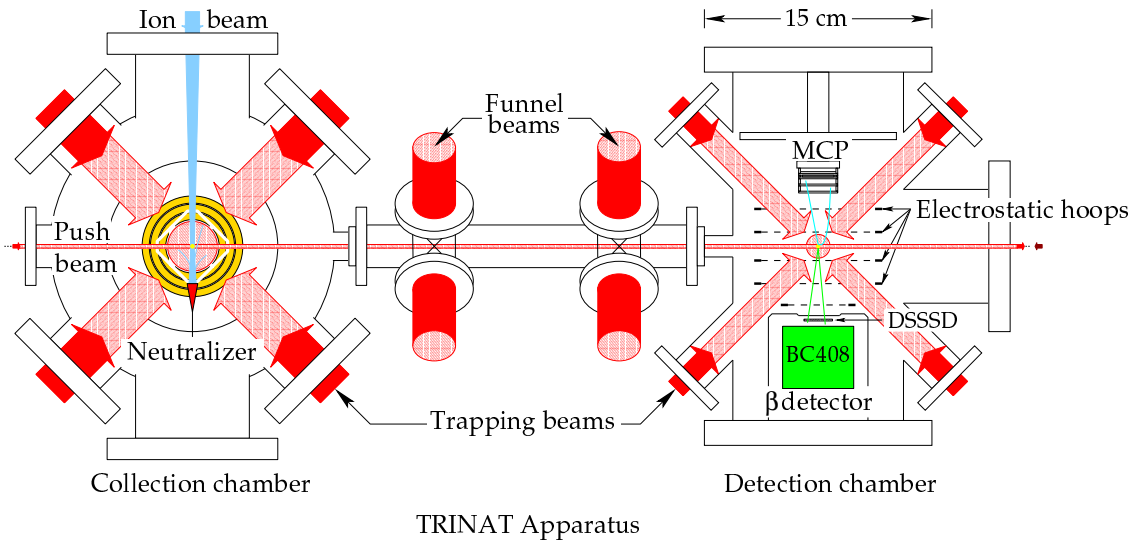

FIGURE 3.6: Schematic diagram of TRINAT's $\beta - \nu$ correlation experiment. The ion beam from ISAC is deposited and neutralized in a Zr foil and then trapped in the first 'collection' trap. The cold, trapped atoms are then transferred to the 2^{nd} trap where the decay is observed using a micro-channel plate (recoils) and the β-telescope (positrons).

centre of the collection trap are then pushed with a small (≈ 1 mm^2) pulsed laser beam to a second 'detection trap.' The push beam, aimed a few millimeters above the 2^{nd} MOT so as not to interfere with any atoms already trapped there, generates a low-energy ($v_{atom} \approx 40$ m/s) atomic beam of ^{38m}K that can be directly captured in the detection trap. The large separation of the two traps reduces the probability of a thermal ^{38}K randomly entering the detection chamber, and so provides a cleaner environment from which to observe the decay.

As the atoms are being transferred they expand radially, so the efficiency of the transfer will rapidly decrease as the inter-trap distance is increased. In order to be able to separate the detection trap 75 cm (enough to add approximately 15 cm of lead shielding) without a great loss of atoms, two 2D MOTs ('atomic funnels') have been employed to compress them back along the push beam axis. The detection trap typically catches 75% of the atoms pushed from the 1^{st} trap. The efficiency of the system as a whole, including capture and transfer, is 5×10^{-4} atoms trapped per ion incident into the neutralizer.

For a more thorough review of TRINAT's double-MOT system and the details regarding the transfer, the interested reader is referred to [37].

3.3 Nuclear Detection System

The $\beta - \nu$ correlation experiment requires the detection of the recoiling Ar atom and the emitted β^+ and, as mentioned earlier, is most sensitive to scalar contributions in the back-to-back geometry. The recoil detector has a nominal active area of 2.6 cm in diameter and is placed -6.23 cm along the $\hat{z}$ direction from the center of the chamber (which roughly corresponds to the detection trap center). The β-telescope is on the opposite side and consists of a 1.2×1.2 cm^2 double-sided silicon strip (ΔE) detector at $z = +6.90$ cm backed by a large plastic scintillator (E) detector. The solid angle subtended by the recoil and β detectors are 0.14 and 0.13 sr respectively.

The MCP purchased from Galileo [38] and depicted in Figure 3.7(a) is a thin array of tens of thousands of tiny cylindrical lead glass channels ($10 - 15$ μm in diameter). Each of the specially formulated micro-channels acts as a miniature electron multiplier tube. An ion incident on one of the channels will generate secondary electrons which are accelerated down the channel wall and generate further secondary electrons, resulting in a cascade which yields amplifications up to a few times 10^4. The applied high voltage bias provides the electric field along the length of the channel, and supplies the electrons needed for the avalanche. The channels are oriented $\approx 11^\circ$ with respect to normal of the MCP surface in order to minimize variations in the detector's efficiency as a function of the incident particle's direction which is related to $\theta_{\beta\nu}$. TRINAT's recoil detector is a combination of three 600 μm thick MCPs in the Z-stack configuration (see Figure 3.7(b)) with an inter-plate separation of 150 μm. The signal from the Z-stack, which has an amplification up to 10^{11}, is registered by a resistive anode which has four separate readouts; the relative distribution of charge between the readouts allows the position of the recoil to be determined to ± 0.25 mm.

As TRINAT is determining the recoil momentum from the position of the hit in the MCP and its time-of-flight relative to the plastic scintillator, the MCP is operated at saturation ($\approx$ 1 keV bias/plate) to make its efficiency as insensitive to the incident ion's energy as possible. The timing resolution of the MCP is excellent (characteris-

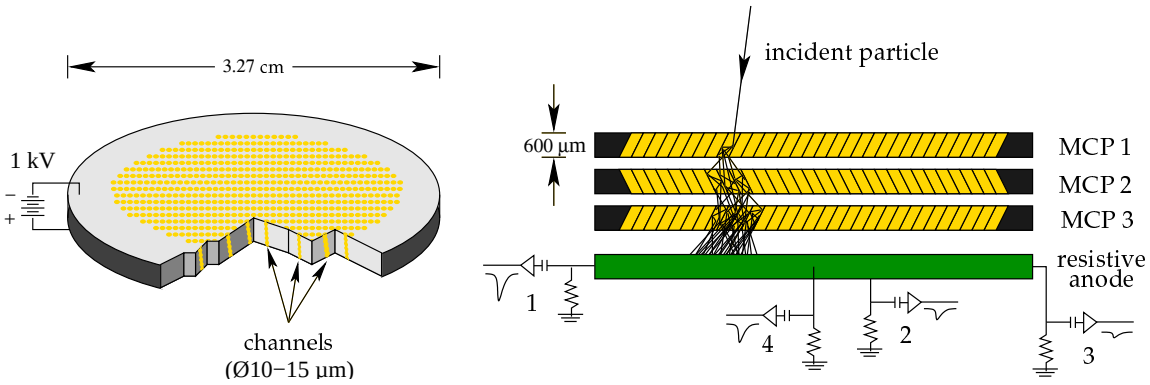

(a) A micro-channel plate

(b) Operation in the Z-stack configuration

FIGURE 3.7: Schematic diagram of an MCP detector and the arrangement used by TRINAT. The distribution of charge of the four resistive anode readouts is used to determine where the event occured.

tically hundreds of picoseconds), and so it is not surprising that the relative timing between the recoil and β detectors is limited by the scintillator's timing (see §4.3.2).

The MCP efficiency for Ar recoils can have a strong dependence on the atom's energy; over energies of $0-450$ eV, the MCP efficiency is not known. This fact makes using the neutral Ar recoils for the correlation experiment very difficult because the slow branch covers a large recoil energy range. For decays where the daughter Ar is a positive ion, however, this source of systematic error can be greatly reduced; TRINAT uses a uniform electric field to accelerate the charged Ar recoils up to energies where the MCP's efficiency is known [39] to be relatively flat ($\delta\epsilon_{\mathrm{MCP}} < 2\%$ between $E_{\mathrm{Ar}} = 5.3 - 5.6$ keV).

Additionally, this field separates the different charge states in TOF and increases the number of detected recoils by focusing Ar ions that would have otherwise missed the MCP. Collection of the complete angular distribution is obtained for charge states greater than $+3$ with our present field of -829 V/cm.

The double-sided silicon-strip detector (DSSSD) provides both position information of the β as well as a coincidence condition to be used with the scintillator to reduce background (non-β) events. The energy deposited in the scintillator (and, to a lesser extend, in the DSSSD) together with the position of the hit in the DSSSD pro-

vides us with a measurement of the β's momentum. Therefore, the energy resolution of the scintillator needs to be as good as possible for the β^+ momentum reading. With the recoil and positron's momenta both measured event-by-event, the momentum of the neutrino can be deduced; in fact the kinematics of the decay are *over*determined, and so we are able to check systematic errors in our experiment.

Chapter 4

The Positron Detector

This chapter will first go through the design of the scintillator and will then go on to the characterization of the ΔE and the E detectors. The β-telescope as a whole is discussed in the final section where results from the April/May 1999 run pertinent to the $\beta - \nu$ correlation experiment will be presented.

4.1 Design and Construction

For the $\beta - \nu$ correlation experiment to succeed, the emitted positron must be detected with good energy resolution and have good timing relative to the recoil MCP detector. In general, the energy of β-particles is difficult to measure accurately because they are relativistic over the $1 - 5$ MeV region of interest; because of their small mass, they scatter easily, into large angles and emit bremsstrahlung radiation which may escape detection. The situation is worse for β^+'s since one must also contend with the possible detection of the annihilation radiation. An added complication is the possibility of annihilation-in-flight, in which case $E_\gamma > m_e$ and it may add to the low-energy tail.

4.1.1 Design Considerations

Early TRINAT experiments utilized a double-Si(Li) detector in conjunction with a double-sided Si-strip detector (DSSSD) to form the E and ΔE detectors of a β-telescope, which has been discussed in detail elsewhere [40]. The Si(Li) semiconductor devices naturally have excellent energy resolution (FWHM $= 60 - 120$ keV over the

region of interest) as well as linear energy responses, but suffer from a number of serious drawbacks: they have a large low-energy tail from bremsstrahlung and the large probability of backscattering off the high-Z material; a systematic error for β's that penetrate the first Si(Li) due to the necessary dead-layer between the detectors; and its overall change in response (the peak of the response function at 2.5 MeV is $\sim 3\times$ larger than at 5 MeV) [40]. Simulations of the correlation experiment [41] compared β-telescopes where the E detector was (1) a double-Si(Li), (2) a $\varnothing$4 cm $\times$ 4 cm plastic scintillator, (3) a $\varnothing$7.5 cm $\times$ 5.1 cm plastic scintillator, and (4) a perfect detector (δ-function response). The simulations used measured response functions from [40] for (1) and (2); the parametrized responses of Clifford et. al's telescope have been published [42, 43] and were used for (3). The results indicated better sensitivity to the correlation parameter if a plastic scintillator similar to the Clifford design was used instead of the Si(Li).

4.1.2 GEANT Simulations

In order to optimize the plastic scintillator for TRINAT's $\beta - \nu$ experiment, Monte Carlo simulations were performed for various geometries using the GEANT detector description and simulation tool [44]. The goal was to design a scintillator that is insensitive to the entrance angle/position of the βs upon the DSSSD.

The initial geometry was extremely simple: a piece of silicon, representing the DSSSD, was placed in front of a cylindrical scintillator, both 'magically' suspended in space. The sizes of scintillator considered ranged from $4 - 6.5$ cm in diameter and lengths between $3.5 - 6$ cm, while the strip detector was constrained to be 2.4 cm $\times$ 2.4 cm $\times$ 491 μm (the size of the existing detector). The simulations helped to determine the best compromise between:

1. Too large a scintillator — Compton scattering of the annihilation radiation adds a high-energy tail (the 'Compton toe') that approximately scales with the volume of the detector.

2. Too small a scintillator — the positrons may escape the detector before annihilating thereby adding to the low-energy tail; also the likelihood of bremsstrahlung radiation escaping increases.

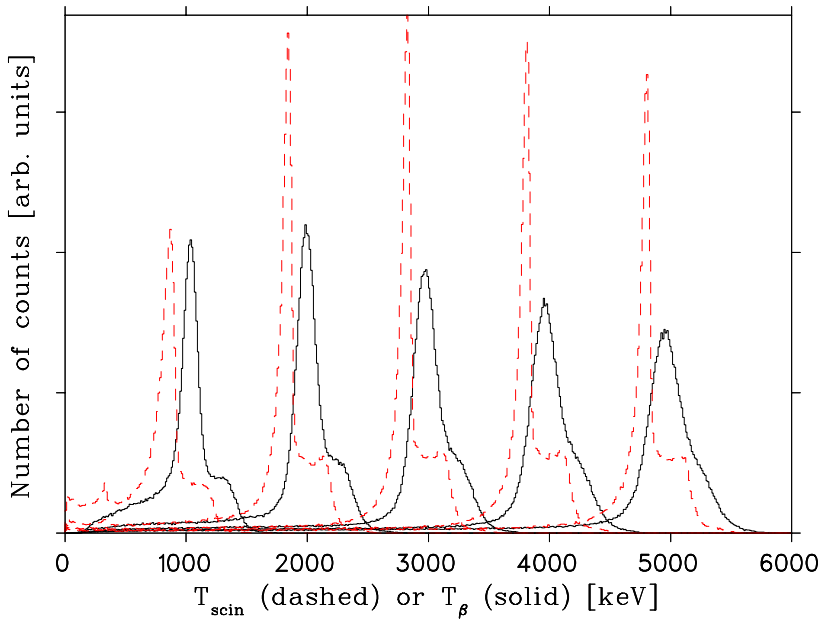

FIGURE 4.1: GEANT simulations of response functions for a ∅6.5 cm × 5.5 cm plastic scintillator for $1, 2, \ldots, 5$ MeV positrons. The solid line has a resolution function folded in and the DSSSD's energy added back in, while the dashed line represents a perfect energy reading which requires a DSSSD coincidence, but the energy is not added to the scintillator's.

Simulations of response functions for a plastic scintillator are depicted in Figure 4.1 for $T_\beta = 1, 2, \ldots, 5$ MeV. The high-energy tail is due to Compton summing of the annihilation radiation and is most prominent for 1 MeV positrons (§A.3). The low-energy tail contains events where the positrons escaped the detector before stopping, but also adding to this tail are cases where bremsstrahlung (radiative) energy losses escape the detector (§A.2) and/or the positron annihilates before depositing all of its kinetic energy and the γ quanta escape (§A.3).

The optimal geometry

Figure 4.2 shows the percentage of positrons that fired the ΔE detector but, due to multiple scattering, missed the scintillator and therefore represent lost events. The plot on the left has the ΔE placed 1.0 cm in front of the E detector while the plot on the right is the case where it is only 0.3 cm away. The effects of backscattering

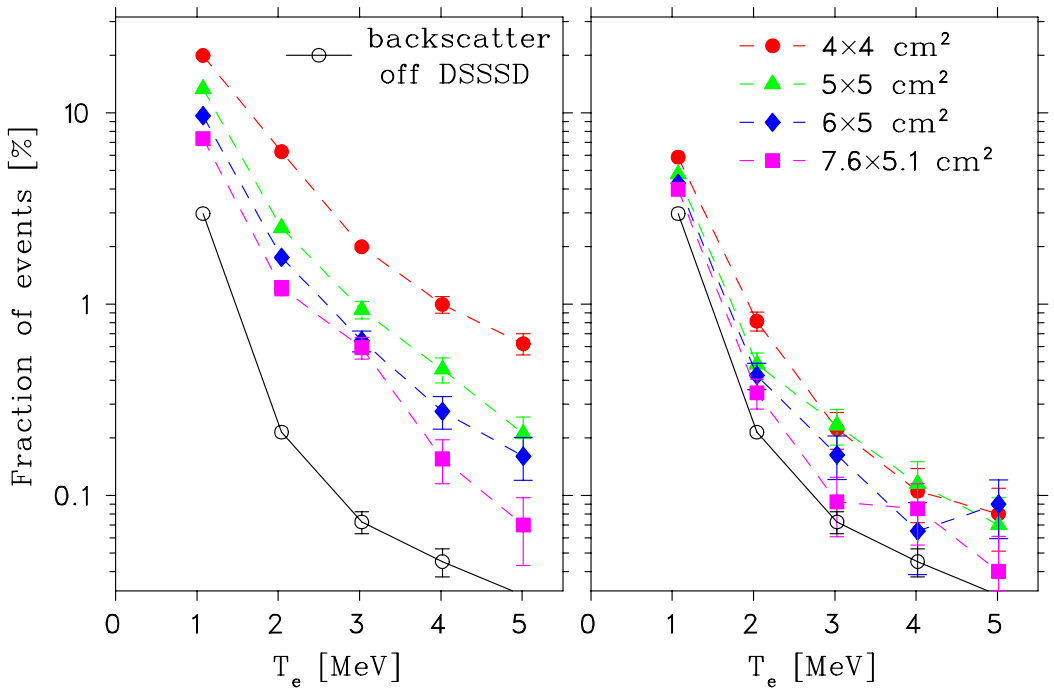

FIGURE 4.2: Monte Carlo design simulation of the fraction of positrons that multiply scattered in the DSSSD and consequently did not interact with the scintillator. The effect depends on the diameter of the scintillator if the DSSSD-scintillator spacing is 10 mm (left), but is nearly independent if this spacing is only 3 mm (right). The 7.6 cm × 5.1 cm design, based on Clifford's dimensions [42], was simulated for comparison.

directly off of the DSSSD is, of course, independent of its position and so the same in both cases. The original DSSSD mount used with the Si(Li) was such that 2.5 cm was the closest the ΔE could be to the front face of the scintillator. The results of Figure 4.2 indicate that almost all of the positrons are fully contained, virtually regardless of the diameter of the scintillator, if the DSSSD is placed close enough to the front face of the scintillator. This motivated the design and implementation of a new mount [45] which enabled us to reduce the spacing to 0.29 cm (see also §4.1.3).

A major factor in determining the optimal diameter was the requirement that all of the positrons come to rest and annihilate within the plastic's volume. In the experiment, the most energetic positrons will have the largest range and so simulations of 5 MeV positrons were performed with a very large scintillator to see what the required length and diameter must be to contain them all. Figure 4.3(a) shows the

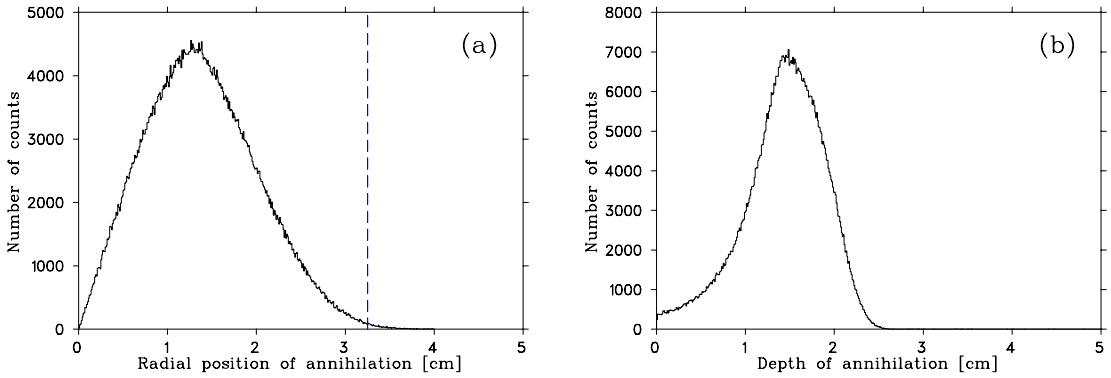

FIGURE 4.3: Monte Carlo design simulations of a pencil beam of 5 MeV positrons depicting the radius (a) and depth (b) of where in the scintillator the annihilation occurred. The dashed line in (a) represents the radius of the scintillator used throughout this thesis.

radius at which the positrons annihilated in the plastic. This aspect of the scintillator design was based primarily upon this result, but other factors, such as the total number of accepted events and the relative percentage in the (high- and low-energy) tails, also supported a larger radius. The dashed line in the figure depicts the final scintillator's size and one can see that virtually all of the positrons are contained. We would have considered a slightly larger diameter, however mechanical constraints due to the existing vacuum chambers limit us to the present design with a 6.5 cm diameter.

The penetration of the βs along the length of the scintillator (Figure 4.3(b)) is well contained below 2.75 cm. The original analysis scheme for the correlation experiment, which involved excluding kinematically forbidden events, was thought to be very insensitive to the re-absorption of annihilation radiation, and so any extra volume was not a *major* concern. The low-energy tail on the other hand, which was the instigating factor for switching from the Si(Li) to a plastic, *is* a potentially large source of systematic error. Therefore, we ordered and (at least for the present time) have continued using a $\varnothing$6.5 cm $\times$ 5.5 cm piece of scintillator, saving the option of later cutting the length to $\approx$ 2.75 cm.

The scintillator used throughout this thesis is 5.5 cm in length, and therefore the Compton toe of the response function is larger than necessary; although we will see

that the present scintillator suffices at this time, the existing scintillator should at some point be compared to one whose depth is only 2.75 cm. If the light collection is not seriously compromised or if the final analysis scheme *does* prove to be sensitive to the re-absorption, the β-telescope should be upgraded with the smaller piece of plastic.

The β window

Some of the β-telescope's components (e.g. the scintillator's wrapping) are not compatible with the ultra-high vacuum needed by a magneto-optical trap and so it is housed in a separate ('β-telescope vacuum') chamber as depicted in Figure 3.6. The front face of this chamber is 7 mm thick stainless steel with a $\varnothing$38 mm 'window' the β particle can enter through to suppress the observation of activity from atoms that do not decay from the trap.

The positrons Coulomb scatter in the foil as they traverse this necessary dead layer and, if the positron scatters into a large angle, the deduced positron momentum (calculated by the position of the subsequent hit in the DSSSD) would *not* be correct. Originally, the β window was a 0.025 mm thick stainless steel foil ($\tilde{Z}_{\text{stst}} \approx 26.5$); however, the characteristic scattering angle [46] that defines the cone the βs scatter into scales with $Z^{2/3}/p_\beta^2$, so the steel is clearly not the optimal material. The scattering angle should be cut in half by using a lower Z material like a commercially available [47] beryllium foil (type IF1, $\tilde{Z} = 4.14$).

In order to see if the position improvements warranted purchasing the relatively expensive beryllium foil, GEANT simulations were performed to compare the beryllium (0.127 mm thick) with the stainless steel. Low energy βs have the greater probability of scattering into large angles, so a pencil beam of 1 MeV positrons was incident normally on the centre of the β window in the simulations to see the position deviations caused by the two types of foils. The geometry in the MC is the same as for the actual telescope used in the April/May 1999 run, which has the front of the DSSSD 2.9 mm behind the β window.

Figure 4.4 shows the radial position of where the positrons hit the ΔE after traversing the two types of foils. The distributions are approximately Gaussian over the peak (from small angle scattering) but have more pronounced tails arising from large angle

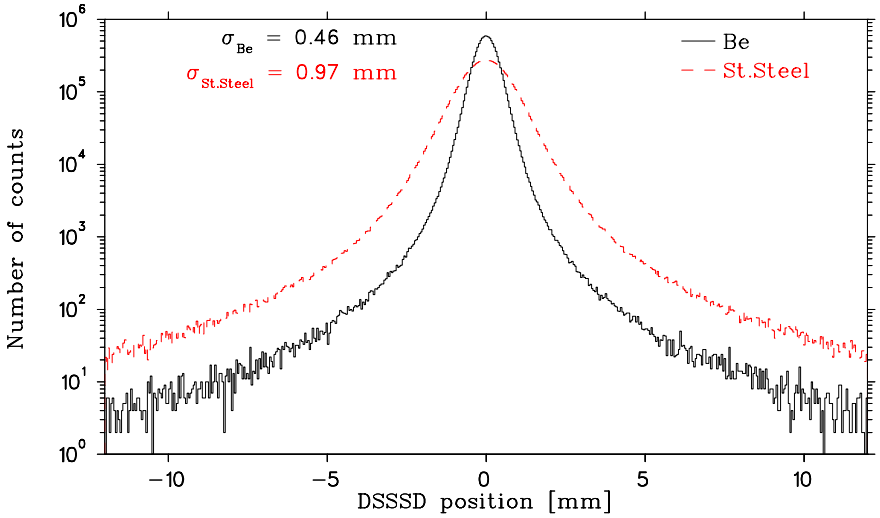

FIGURE 4.4: Monte Carlo design simulations of multiple scattering effects due to the β window. The solid line depicts a pencil beam of 1 MeV positrons entering the DSSSD after traversing a 0.127 mm beryllium foil while the dashed simulates 0.025 mm stainless steel. Both foils are placed 2.9 mm in front of the DSSSD.

(Rutherford) scattering. The widths of the distributions are 0.46 and 0.97 mm for the beryllium and stainless steel respectively. For the stainless steel foil, then, a β originally incident towards a given DSSSD strip will only have 1σ of this distribution firing that strip, whereas 2σ will fire the correct one for beryllium. This factor of two improvement is decidedly worth the effort, and so the β window was changed to the 0.127 mm thick beryllium.

4.1.3 The Final Design of the Telescope

The Telescope Assembly

The realization of the plastic scintillator and of the β-telescope as a whole is depicted in Figure 4.5. The scintillator, a $\varnothing$6.5 cm $\times$ 5.5 cm long BC408 plastic purchased from Bicron [48], is optically coupled to a plexiglass light guide which in turn is coupled to a Philips 4312/B 12-stage photomultiplier tube (PMT). Both the plastic and the light pipe are wrapped with a diffuse reflector, Teflon, to increase collection of the scintillation light as discussed in §4.3.1. The scintillation light produced in the BC408 (λ_{max} = 425 nm) overlaps the maximum of the bialkali photocathode's

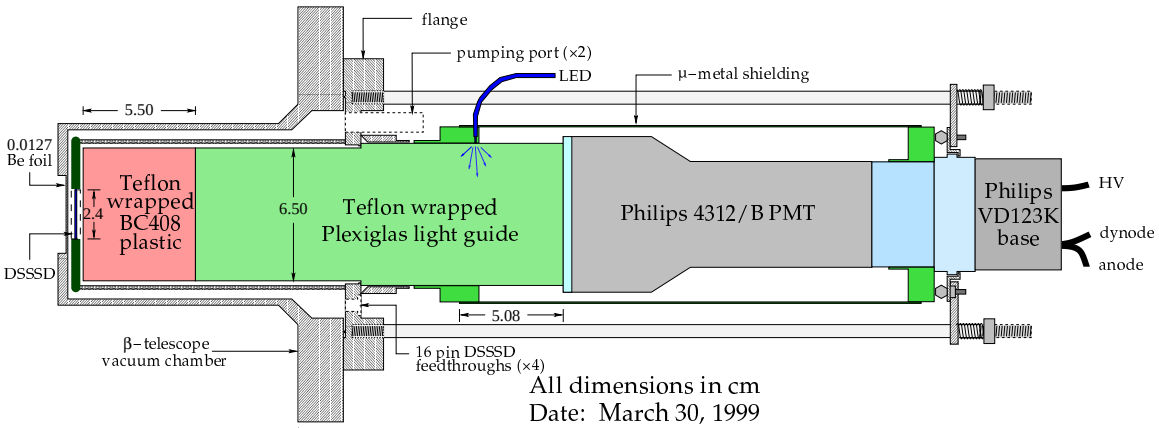

FIGURE 4.5: Schematic diagram of the β-telescope assembly (to scale). The major components are described in the text.

response (400 – 450 nm; 20% quantum efficiency). The Philips PMT was chosen because it was specified to have a good hybrid of energy and timing characteristics. A transistorized voltage divider assembly (Philips VD123K) was used to minimize gain fluctuations arising from variations of the dynode voltages.

The β-telescope's chamber separates the trapping region's 2×10^{-10} Torr ultra-high vacuum from the telescope's poorer vacuum of typically 5×10^{-4} Torr. A conflat flange was modified by adding two vacuum pumping ports and four 16-pin electronic feedthroughs for the 48 DSSSD strips. The vacuum is maintained by an O-ring which seals the light guide to the flange using a specially designed clamp.

The PMT is surrounded by 0.2 mm thick μ-metal which, in addition to protecting the PMT from magnetic fields, also serves to make the system light-tight. A blue LED[†] with a nominal wavelength of 450 nm (closely matched to the scintillation light) is coupled to the PMT via a fibre-optic cable as shown in the figure. This is used to stabilize the PMT gain as discussed in §4.3.4.

The DSSSD is mounted within a plexiglass disk (as shown in Figure 4.6) whose thickness is only slightly larger than the 0.40 cm thick frame of the DSSSD (which mounts the silicon wafer and houses the strip readout contacts). The low Z material and minimal thickness was chosen so as to reduce the probability of βs scattering off this mount. The plexiglass plate provides both a rigid mount as well as a well-

[†]A Panasonic digikey #P390-ND light emitting diode.

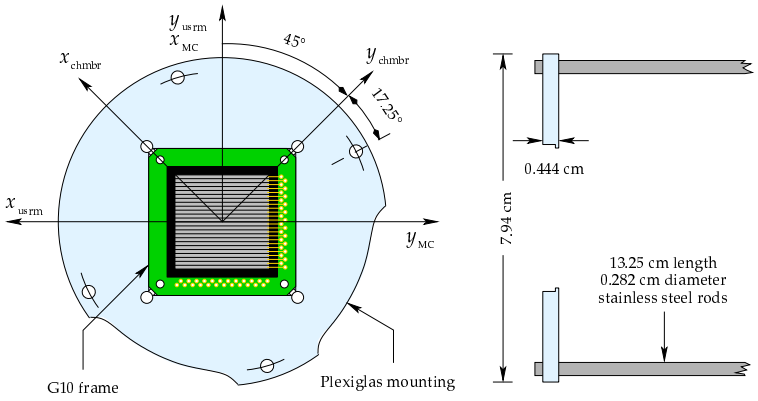

FIGURE 4.6: Schematic diagram of the DSSSD mounting showing the strip detector's reference frame relative to that of the detection chamber.

defined overall DSSSD orientation; with the axes defined in Figures 3.6 and 4.7, the DSSSD is rotated $+(45.0 \pm 0.5)^\circ$ with the y-strips facing the recoil detector. The G10 frame represents the largest source of scattered βs adding to the telescope's low-energy tail; as the DSSSD is manufactured this way, we are not free to reduce this contribution mechanically, but we may suppress it in software by not including the edge strips in the analysis (see §4.2). Coaxial wiring for the strip readouts is fed out of the β-telescope's vacuum chamber through the 16-pin feedthroughs, and is input to locally constructed [49] preamplifiers which are mounted directly on the flange. The wiring from outside the shielded vacuum chamber to the preamplifiers is coaxial (and additionally are shielded) to prevent noise from electrical pick-up.

Final GEANT Geometry

Once the β-telescope was built and optimized, a more realistic description of the geometry was input in the Monte Carlo simulation. A diagram of the volumes included in GEANT is given in Figure 4.7. The β window is at $z = +6.60$ cm and is defined by the specifications [47] of the IF1 type beryllium[†]. The bulk of DSSSD remains a pure wafer of silicon, but now the geometry of the detector includes the 48 aluminum

[†]99.837% Be, with the biggest contaminations from Fe (0.006%), Ni (0.02%), Ca (0.02%) and Zn (0.01%). These percentages, and those hereafter, give the relative number of elements making up the medium.

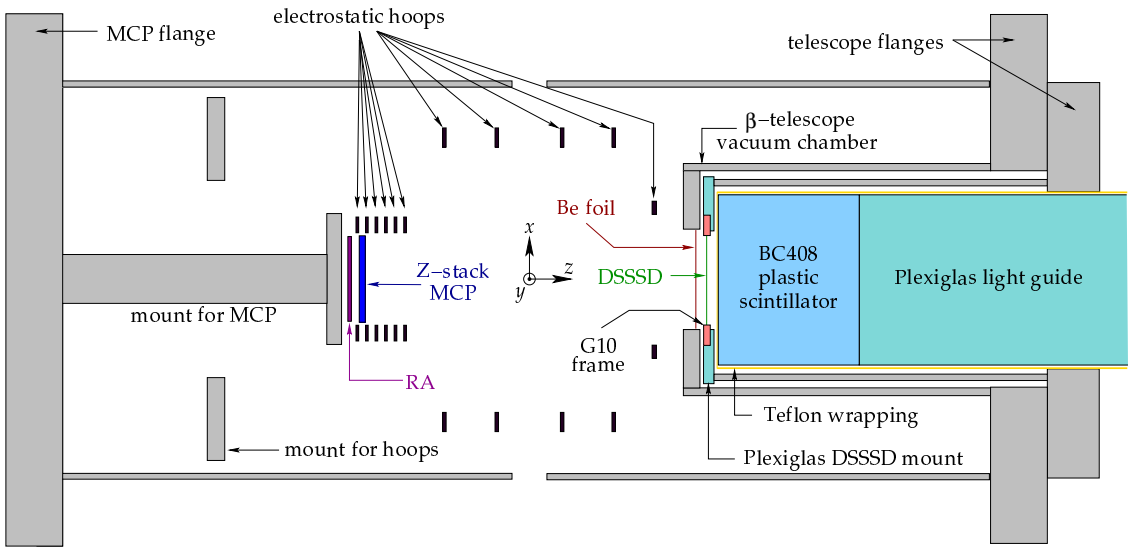

FIGURE 4.7: Geometry of TRINAT's detection chamber that is input into further (detailed) Monte Carlo simulations. The volumes outside of the β-telescope's vacuum chamber are important because positrons can (back)scatter off of them before entering the β-telescope.

readout strips (assumed to be 500 Å thick) and, more importantly with regard to scattering effects, the G10[†] frame in which the wafer is mounted. The plexiglass[‡] mount was simplified in the MC by approximating it as a ring whose inner diameter does not overlap the G10 frame. The four stainless steel rods connecting the DSSSD mount to the (smaller) telescope flange are also included.

The scintillator has five layers of Teflon[*] on the front face totalling 0.02 cm in thickness, and many layers around the sides of the scintillator and light guide, totalling about 0.7 cm in thickness. The BC408 plastic is defined by the hydrogen to carbon ratio of 1.104, but also contains a 2% addition of PPO[††] which is added to increase scintillation efficiency [50]. The light guide extends out past the flanges, but other components behind the flanges (the clamp, the PMT, etc.) were not included because they will not affect detection of the positron.

[†] defined as 60% SiO_2 and 40% Kapton ($C_{22}H_{10}N_2O_5$).
[‡] defined as $CH_2{=}C(CH_3)CO_2CH_3$.
[*] defined as $CF_2{=}CF_2$.
[††] defined as $C_{15}H_{11}N_1O_1$ (2,5-diphenyloxazole).

The rest of the geometry includes the 2nd trapping chamber, the aluminum hoops for the electric field and the MCP assembly. The material of the MCP plates is Corning 8161 glass† and the resistive anode is pure Si. A large number of β's were found to scatter off the MCP or one of its electrostatic components before entering the β-telescope (see §4.5.1) and so it is important to keep these volumes in the Monte Carlo, even though it requires $\approx 10\times$ the CPU time. The rods for the hoops, not included in the simulations presented here, have since been included since they offer a considerable volume of stainless steel that βs can scatter from.

4.2 The Double Sided Silicon Strip Detector

This section begins with a brief introduction to these semiconductor devices, but for a more thorough review, the interested reader is referred to [51]. Sections 4.2.2–4 describe the energy calibration and resolution of the detector, followed by the position decoding scheme in §4.2.5. The final section, §4.2.6, presents the results obtained from the correlation experiment data.

4.2.1 The Device

The ΔE component of the β-telescope is a double sided silicon strip detector purchased from Micron Semiconductor [52]. It is a silicon wafer of dimensions 2.4 cm $\times$ 2.4 cm $\times$ 491 μm upon which a thin (typically a few μm) p^+-type layer is deposited onto the 'front' or ohmic side of the n-type silicon. Similarly an n^+-type layer is deposited on the grounded side ('rear') of the detector as depicted in Figure 4.8. This forms a p^+n junction, each side upon which is evaporated a thin (typically 500 Å) layer of aluminum; a reverse bias of -135 V is applied to the p^+ side (with the n^+ side at ground) to ensure that the depletion layer extends throughout the Si wafer so that all of the energy deposited by an ionizing particle gets collected onto the aluminum readouts. The negative bias also increases the magnitude of the electric field across the depletion layer which serves both to make the charge collection more complete as

†defined as 8.8% Pb, 61.1% O, 24.6% Si, 4% K, 0.8% Rb, 0.3%Ba, 0.19%As, 0.08% Cs and 0.15% Na.

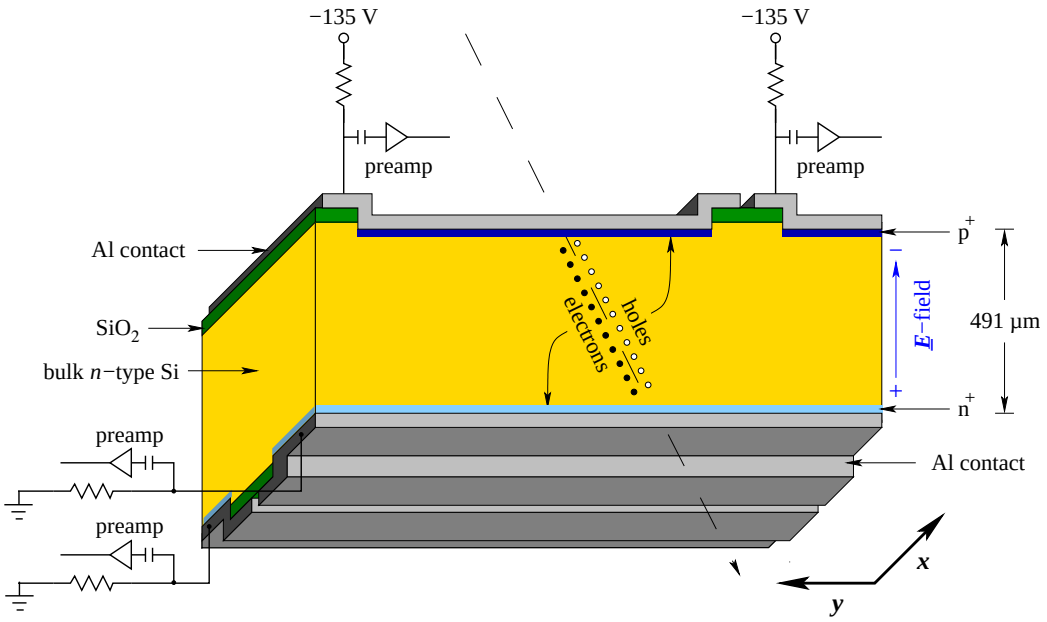

FIGURE 4.8: Schematic diagram of a p^+n double-sided silicon strip detector. Electron-hole pairs are created as an ionizing particle goes through the depletion region, and they are separately collected on readouts on the p^+ (electrons) and n^+ (holes) side. Both of these readouts are divided into 24 strips, providing position sensitivity in both $\hat{x}$ and $\hat{y}$.

well as to decrease the time needed for the electrons and holes to reach the readouts (*i.e.* the pulse duration). To add position sensitivity to this detector, the aluminum readouts are both divided into 24 *orthogonal* strips whose width and spacing are nominally 900 and 100 μm respectively. The lengths of the p^+ strips are aligned with $\hat{x}$ and so, depending on which strip registers the hole collection, we obtain the position of the hit in $\hat{y}$. Similarly, position information in $\hat{x}$ is determined by the negative charge collection on a given n^+ strip. With a depletion depth of $d = 491$ μm, the capacitance works out to $C_{\text{strip}} \approx A/d = 4.4$ pF, where $A = 900$ μm $\times$ 2.4 cm is the area of a strip.

Upon entering (and exiting) the detector, a charged particle will interact with the aluminum contacts, thus introducing two necessary (yet entirely negligible) dead layers. As the particle then goes through the bulk silicon, the energy deposited through multiple Coulomb scattering in the depletion region† creates electron-hole pairs; the

†though fully depleted, the wafer will have small gaps in its depletion region near the surface of

positive holes are swept by the electric field to a readout on the ohmic side while the negative electrons migrate to the readout at ground. Thus for each event, the DSSSD fires *two* pulses – one for holes and the other for electrons – which are both proportional to the energy deposited by the incident particle. The electrons and holes are created in pairs so the two signals should in fact be *identical*, although in practice differences occur due to electronic noise and, hopefully to a lesser extent, uncertainties in the energy calibration of the strips.

The electronics for the DSSSD is illustrated by the sample strips depicted in the figure of Appendix C (page 128). The timing of the `y`-strips is used to trigger events while the energy signal (of both the `x`- and `y`-strips) goes directly to LeCroy 2249A charge-sensitive ADCs. The timing signals are fanned together in groups of four, each of which is then input to the 2228A TDC for separate timing; these six groups are then fanned together giving any 'DSSSD event' either (a) used to provide an event trigger (off-line calibrations) or (b) checked to see if it is coincident with the scintillator's timing (on-line event trigger). The hardware thresholds for each of the 24 triggering strips were individually optimized and set to be above their respective pedestals (≤ 20 keV).

We will see how with a good energy calibration and an understanding of the detector's resolution, a condition on the difference between the two energy readings provides a clean tag for β events.

4.2.2 Energy Calibration

Low-energy photons from the decay of ^{241}Am and ^{133}Ba were used to calibrate the strip detector. ^{133}Ba decays by electron capture [53] to a number of excited states in ^{133}Cs. The resulting radiation consists of Cs X-rays as well as several γ rays, with the photons of interest listed in Table 4.1. For calibration purposes, we use the weighted average of the two unresolved M1 γ peaks and fit to one (slightly widened) peak at 80.898 keV. Similarly, the K_{α_1}- and K_{α_2}-shell X-rays are averaged to 30.851 keV. The α decay of ^{241}Am to ^{237}Np has a strong $E1$ branch ($E_\gamma = 59.5412$ keV [54]), providing us with a third calibration point.

the areas between strips — carriers generated here do not get collected with the same efficiency.

The photoelectric effect and Compton scattering are the two competing processes for photon interactions over the energy range $h\nu = 30 - 80$ keV in silicon. In a photoelectric process, a K-shell electron bound to the Si atom totally absorbs the incident energy; this 'photoelectron' is ejected with a kinetic energy $T_e = h\nu - B_e$, where B_e is the shell binding energy. As was the case for barium, the inner shell vacancy is filled up, but in this case Auger processes are favoured and so the binding energy is generally recovered. In Compton scattering† the photon imparts only a part of its energy to the struck 'Compton electron', the amount of which depends entirely on the direction of the scattered photon. The result is an energy spectrum that extends from zero up to a maximum $(T_e)_{max} < h\nu$ corresponding to a backscattered photon (see Equation (4.12)). For 30 keV X-rays, the photoelectric effect has the largest cross-section so the DSSSD spectrum contains the large peak at $E = h\nu$ with a small low-energy tail arising from Compton collisions. At 60 keV, these processes have about equal cross sections and by 80 keV the Compton effect is an order of magnitude larger; since the photoelectron's spectrum is concentrated over a small energy range, the photoelectric peak is still evident in the γ sources, although the Compton tail complicates determining the centroid as precisely as with the X-rays.

In addition to those resulting from the photon sources, a large peak referred to as the 'pedestal' is evident in the energy spectrum (as in Figure 4.9); this peak occurs when the strip in question did not fire, but another strip triggered the event. For the charge-integrating ADC's used, the observed pulse-height of the non-triggered

†this is covered in more detail in §4.3.3 with regard to the off-line scintillator calibration.

	Source	Rel. intensity	Energy [keV]	
^{133}Ba	Cs K_{α_1}	0.648	30.973	30.851
	Cs K_{α_2}	0.351	30.625	
	γ (M1)	0.929	80.9971(27)	80.898
	γ (M1)	0.071	79.6139(6)	
^{241}Am	γ (E1)	—	59.541	

TABLE 4.1: Low-energy photon sources used to provide an initial calibration of the strip detector.

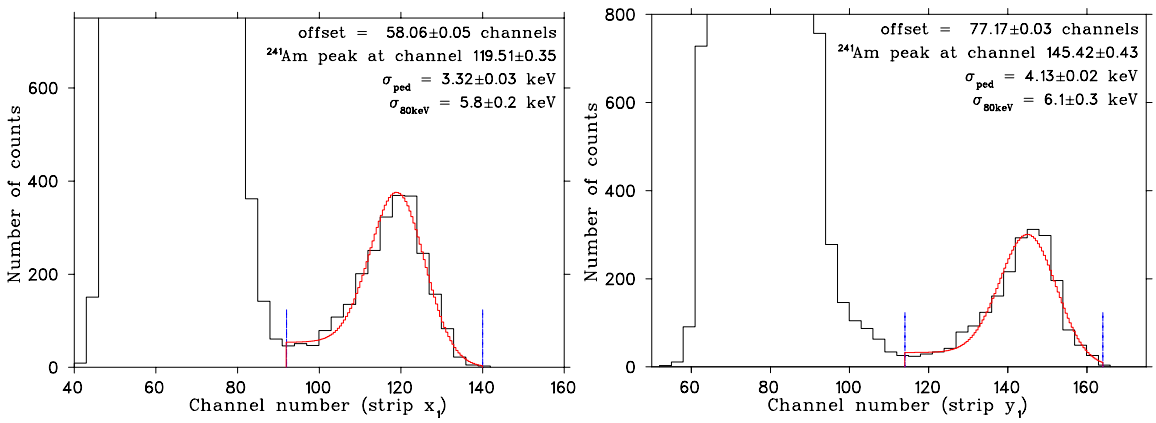

FIGURE 4.9: Sample fits to the DSSSD energy spectrum of the γ source ^{241}Am. The data is the coarsely binned histogram and overlayed is the fit using a function consisting of a Gaussian (photoelectrons) plus a constant low-energy background (Compton electrons). The fitting range is indicated by the lines above and below the 59.541 keV peak.

strip corresponds to the ADC offset and, ideally, would be a δ function. In reality, the pedestal is a Gaussian peak centered at zero energy with a width that directly reflects the noise in the electronics. The average width for the x-strips is $\langle\sigma_{\mathrm{x}}^{\mathrm{elec}}\rangle = 3.7 \pm 0.7$ keV and that of the y strips $\langle\sigma_{\mathrm{y}}^{\mathrm{elec}}\rangle = 3.9 \pm 0.4$ keV. The centroids of each of the photoelectron peaks as well as the pedestal provide four points which can be fit to a linear calibration relating the observed pulse height with the energy deposited in the detector.

The Am and Ba sources were placed in front of the DSSSD within a light-tight and electrically shielded volume: a thin stainless steel cylinder ∅40 cm × 60 cm (sufficiently large to minimize scattering effects off the walls of the container) with a mount for the β-telescope assembly.

Each peak in the resulting energy spectra of the 48 strips was then individually fit to a function consisting of a constant background that extends below the mean of a Gaussian peak (the *photopeak*) representing the full energy reading of the ejected photoelectron. Fits to the 60 keV peak from ^{241}Am in strips x_1 and y_1 are given in Figure 4.9. The pedestal is fit independently by gating on pulser events for the scintillator, in which case all of the DSSSD strips were read out with zero energy. The widths, which are calculated using the final off-line source calibration, are typical;

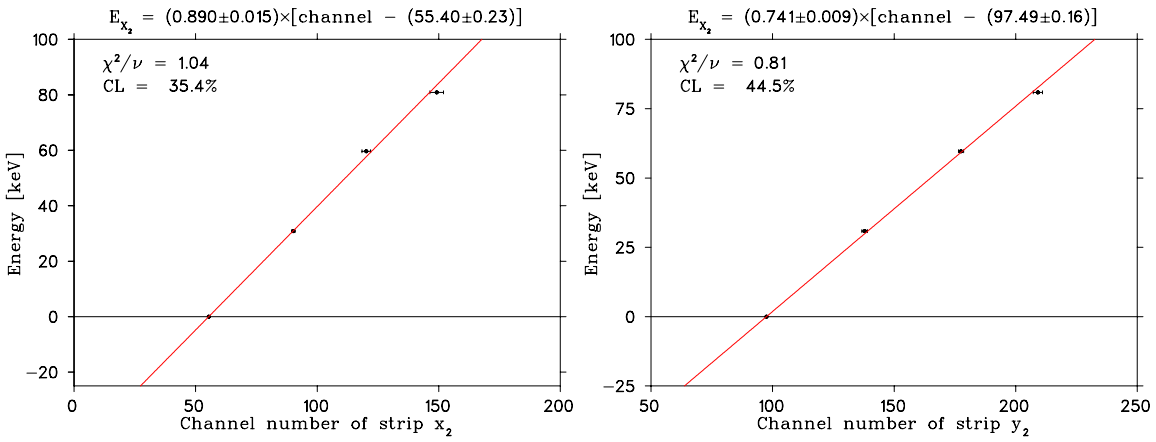

FIGURE 4.10: Energy calibration of the DSSSD strips $\mathtt{x}_2$ and $\mathtt{y}_2$ using the sources ^{133}Ba and ^{241}Am. The four points used in the fits (given above) consist of the sources listed in Table 4.2 plus the ADC offset. The calibrations have an offset with units of channels and the slope has units of keV/channel.

the pedestals contribute $3-4$ keV to the noise while the pulsers are roughly equal to the photopeak widths of $5-6$ keV. The fits to the barium peaks were done in a similar fashion, but in that case a separate overall constant background was also required to account for the higher energy photons that Compton scatter in the detector. The 81 keV photon interacts predominately through Compton scattering, so the resulting photopeak in the observed spectrum is weaker compared to that arising from the Cs K_α-shell photons; these calibration points, therefore, have relatively large uncertainties in their values.

Using the results of the fits to these spectra, energy calibrations were made using linear regression on the four points. Figure 4.10 is the calibration for $\mathtt{x}_2$ and $\mathtt{y}_2$ and numerical results of the off-line source calibrations are given in Table 4.2. The calibration to the strips look reasonable but, as we will see in the following section, we can improve the calibrations using the on-line β^+ data themselves.

4.2.3 Extended Calibrations

In addition to the inherent resolution, the final energy reading from the strip detector will also be affected by systematic deviations in each strip's calibration in many ways. As we will see in §4.2.5, event selection is based upon which and how many strips

strip number	x calibration		y calibration	
	offset (channels)	slope (keV/chan)	offset (channels)	slope (keV/chan)
1	58.11±0.44	0.871±0.028	77.15±0.24	0.850±0.017
2	55.40±0.23	0.890±0.015	97.49±0.16	0.741±0.009
3	43.49±0.27	0.893±0.018	75.26±0.12	0.822±0.008
4	43.79±0.18	0.885±0.012	72.62±0.22	0.805±0.014
5	58.59±0.30	0.848±0.018	74.98±0.25	0.768±0.015
6	62.64±0.30	0.965±0.023	52.98±0.30	0.854±0.022
7	60.03±0.24	0.982±0.019	66.82±0.26	0.817±0.018
8	51.98±0.40	0.949±0.030	75.17±0.17	0.815±0.011
9	65.10±0.20	0.816±0.011	123.26±0.14	0.700±0.007
10	65.99±0.27	0.792±0.014	73.86±0.28	0.773±0.017
11	64.02±0.27	0.837±0.015	96.11±0.29	0.792±0.018
12	67.49±0.21	0.786±0.011	92.87±0.20	0.756±0.011
13	64.04±0.21	0.925±0.015	42.41±0.31	0.807±0.020
14	61.74±0.26	1.006±0.021	53.46±0.25	0.847±0.018
15	61.08±0.25	0.965±0.019	86.45±0.20	0.788±0.012
16	190.32±0.39	0.685±0.015	51.93±0.35	0.775±0.021
17	71.85±0.25	0.768±0.012	72.52±0.28	0.759±0.016
18	61.15±0.23	0.809±0.013	108.56±0.18	0.761±0.010
19	91.98±0.26	0.820±0.014	126.26±0.21	0.725±0.011
20	63.54±0.28	0.828±0.016	55.63±0.24	0.843±0.017
21	72.66±0.31	0.815±0.017	59.63±0.28	0.825±0.019
22	63.27±0.35	0.767±0.017	59.94±0.29	0.810±0.019
23	63.57±0.28	0.857±0.017	111.81±0.21	0.859±0.016
24	69.42±0.57	0.736±0.026	66.43±0.28	0.797±0.018

TABLE 4.2: Fit parameters of the DSSSD strips off-line source calibration. The calibration is fit to a function of the form $E[\text{keV}] = \text{slope} \times (\text{channel} - \text{offset})$.

pass a calibrated energy threshold, as well as a maximum limit on $\Delta E = |E_{\mathtt{x}} - E_{\mathtt{y}}|$, and so poor energy calibrations will cut legitimate events. In order to minimize the differences in each strip's energy reading, we take advantage of the fact that the two signals in $\hat{x}$ and $\hat{y}$ should be identical, and effectively re-align the strips by forcing that fact to be true on average. To that end we can use the on-line ^{38m}K data which is advantageous because they provide a continuous spectrum well beyond the 81 keV barium peak; the re-alignment of the calibrations using the data themselves is, by definition, over the entire energy range of interest.

In applying the off-line calibrations to the on-line data, corrections for possible DC offset and gain variations in the electronics were made by comparing the peak positions of the pedestals and pulsers. Throughout the experimental runs, the offsets of the original calibrations are adjusted by the difference in the pedestal centroids (over $\approx$ 5 minute intervals) from the centroids observed when calibrated. Similarly, the slope of the calibrations was adjusted by the ratio of the pulser centroids. If x°_{ped} is the pedestal and $x^{\circ}_{\mathrm{puls}}$ the pulser centroid when the off-line calibration was done, then the corrections applied at time t are:

$$\mathrm{offset}'(t) = \mathrm{offset} - (x_{\mathrm{ped}}(t) - x^{\circ}_{\mathrm{ped}}) \tag{4.1}$$

$$\mathrm{slope}'(t) = \mathrm{slope}\left(\frac{x_{\mathrm{puls}}(t) - x_{\mathrm{ped}}(t)}{x^{\circ}_{\mathrm{puls}} - x^{\circ}_{\mathrm{ped}}}\right) \tag{4.2}$$

The calibrations were done only a few days before the April 1999 experiment and since the DSSSD is an inherently stable device, these corrections end up being very small, typically on the order of 0.1%.

After applying these corrections to the ^{38m}K β^+ data, for each x-strip that passed a low-energy threshold of 40 keV with only one corresponding strip in y, the energies $E_{\mathtt{x}}$ and $E_{\mathtt{y}}$ were plotted as in Figure 4.11. Assuming that variations in the y-strips' calibrations average out, the deviation from $\langle E_{\mathtt{y}} \rangle = E_{\mathtt{x}_i}$ provides us with a correction

$$E'_{\mathtt{x}_i}(E_{\mathtt{x}_i}) = \alpha_{\mathtt{x}_i} E_{\mathtt{x}_i} + \beta_{\mathtt{x}_i} \tag{4.3}$$

with which to align each of the x-strips to the average of y. In making the fits, Poissonian statistics needed to be used in order to be able to include the scarce events

at higher energies. Note, however, the extended low-energy tail especially evident in the edge strip $\mathtt{x}_1$ (the inner strips, e.g. $\mathtt{x}_2$, are much cleaner indicating edge effects in the DSSSD). *Every* event in Figure 4.11 is plotted, so this actually only represents $\lesssim 10\%$ ($\lesssim 1\%$) of the total number of counts in the edge (inner) strips. It is still an important concern, however, because this low-energy tail has a stronger weighting in the fits if all the data are used, thereby biasing the calibrations to $\alpha_{\mathtt{x}_i} < 1$ and $\beta_{\mathtt{x}_i} > 0$. In order to minimize this effect, yet still retain the high-energy events, an iterative method was used: in the first step we assume $\alpha_{\mathtt{x}_i} = 1$, $\beta_{\mathtt{x}_i} = 0$ and fit Equation (4.3) only to events where $E_{\mathtt{x}} - 30\text{keV} \leq E_{\mathtt{y}} \leq E_{\mathtt{x}} + 30\text{keV}$. Based on the new values of $\alpha_{\mathtt{x}_i}$ and $\beta_{\mathtt{x}_i}$, we again fit using events where the new $|E_{\mathtt{y}} - E'_{\mathtt{x}}| \leq 30$ keV. This process was repeated until the changes in the parameter values were less than their respective uncertainties. Table 4.3 lists in detail the corrections to each of the x-strips using this alignment scheme.

The iterative method used to fit the extended calibrations ends up applying rather large corrections to the ^{241}Am and ^{133}Ba calibrations. Generally, the slopes are decreased and the offsets increased, but by far more than can be explained by the bias from the low-energy tail as described above. Most surprising is the change in the offset; the pedestal peak is well-defined and if it really does represent zero-energy, one would expect the $\beta_{\mathtt{x}_i}$ parameters to be very close to zero. Random changes in the $\alpha_{\mathtt{x}_i}$ would be expected (versus a systematic difference) since the larger energy range of the on-line data is more sensitive to the slope of the calibrations. The extended calibrations and the calibration of the DSSSD as a whole are therefore not without their problems, and so the uncertainties quoted by the fit are certainly underestimated.

The extended calibrations *are* effective in aligning all of the x-strips' calibrations together, which is necessary in order to be able to compare the energies of each equally. In order to similarly place the y-strips on equal footing, we do the same procedure to re-fit them to the average of the corrected x-strips. The corrections are listed in Table 4.4 and Figure 4.12 shows the fits to $\mathtt{y}_1$ and $\mathtt{y}_2$. The variance of the points around the fit is reduced compared to Figure 4.11 because the x-strips have already been calibrated to a common energy axis. The fit parameters still show the same trends as in the x-strips ($\beta_{\mathtt{y}_i} > 0$ and $\alpha_{\mathtt{y}_i} < 1$), but are not as large or systematic. The high-energy tails, however, can be seen to still have a bias since they do not

TABLE 4.3: DSSSD calibration fits of $E'_{\mathtt{x}_i} = \langle E_{\mathtt{y}} \rangle = \alpha_{\mathtt{x}_i} \times E_{\mathtt{x}_i} + \beta_{\mathtt{x}_i}$. These fits align the calibrations of the x-strips to the average calibrations of the y-strips.

strip	$\beta_{\mathtt{x}}$ (keV)	$\alpha_{\mathtt{x}}$ (keV/keV)	strip	$\beta_{\mathtt{x}}$ (keV)	$\alpha_{\mathtt{x}}$ (keV/keV)
1	16.94±0.11	0.9075±0.0006	13	12.94±0.10	0.8751±0.0005
2	13.55±0.10	0.8671±0.0005	14	16.80±0.10	0.8010±0.0005
3	14.44±0.10	0.8562±0.0005	15	15.66±0.10	0.8586±0.0005
4	10.99±0.10	0.9230±0.0006	16	−5.67±0.11	1.1542±0.0007
5	12.27±0.10	0.9015±0.0006	17	5.01±0.11	0.9923±0.0006
6	16.44±0.10	0.8729±0.0005	18	7.12±0.10	0.9811±0.0006
7	16.08±0.10	0.8804±0.0005	19	6.50±0.11	0.9691±0.0006
8	17.55±0.10	0.8671±0.0005	20	6.65±0.11	0.9720±0.0006
9	5.20±0.11	0.9830±0.0006	21	6.52±0.11	0.9948±0.0006
10	5.20±0.10	0.9856±0.0006	22	6.07±0.11	0.9769±0.0006
11	6.59±0.11	0.9921±0.0006	23	7.24±0.11	0.9832±0.0006
12	5.01±0.11	0.9803±0.0006	24	9.47±0.12	0.9797±0.0007

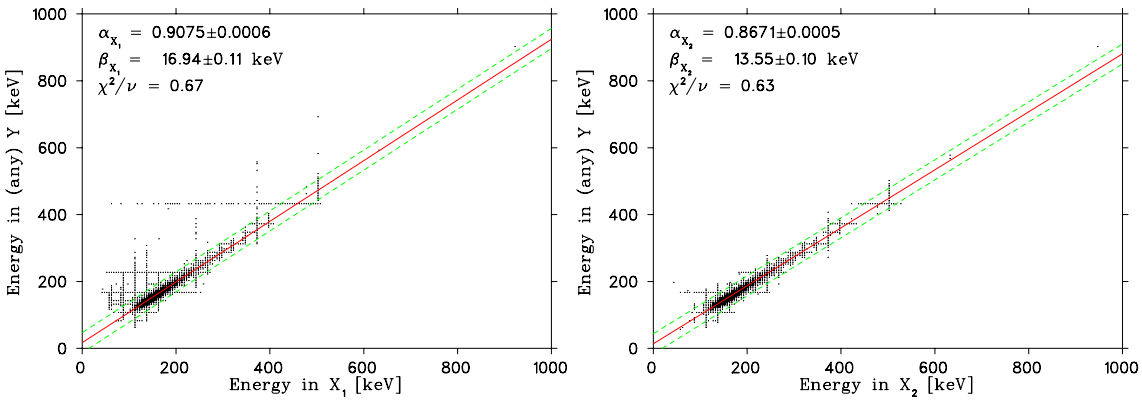

FIGURE 4.11: Comparison of $E_{\mathtt{x}}$ and $E_{\mathtt{y}}$ energy readings using the calibrations determined using off-line sources for strip $\mathtt{x}_1$ (left) and $\mathtt{x}_2$ (right). The solid line is the fit $E'_{\mathtt{x}} = \alpha \times E_{\mathtt{x}} + \beta_{\mathtt{x}}$ and the dashed lines contain the fitting region defined by $|E_{\mathtt{y}} - E'_{\mathtt{x}}| \leq 30$ keV.

follow the fit line to within the quoted uncertainties, again indicating that they are underestimated.

As with the x edge strips the y-strips contain a background, but in this case it is manifest as a *high*-energy tail. The vast majority of these events have too much energy in $\hat{y}$ and correspondingly too little energy in $\hat{x}$. Yorkston, et. al [55] have discussed such effects in the case where the incident particle was a heavy ion, and they found that inter-strip events gave rise to pulses of the *wrong* polarity from induced charges. They performed similar tests with ^{207}Bi but did not observe this effect in this case; the tails seen in our edge strips are not at present understood, but the effect is relatively small and the events can be excluded in software if desired (see also §4.4.3).

4.2.4 Characterization of the Resolution

The dominant noise apparent in the DSSSD spectra is electrical, but additional components arise from fluctuations in particle-hole generation and charge collection. As mentioned earlier, the electrical noise determines the width of the pedestal while the overall inherent resolution of the detector should be reflected by the width of the photopeaks. The average widths of the ^{133}Ba $M1$ γ peaks are 5.6 ± 0.5 keV for y and 5.5 ± 0.9 keV for x, in agreement with the resolution of these devices as indicated in the literature [51].

The final resolution of each strip was determined by comparing the difference of the corrected energy reading of a given strip to that of the orthogonal's corrected energy. This is basically the same procedure as in the extended calibrations, except this time we just look at the deviations in order to generate an average resolution function. As can be seen for $\mathtt{x}_{16}$ in Figure 4.13, the final extended calibration of this strip versus all of those in y still suffers from a slight bias, as is especially evident from events in the high-energy tail of the peak (above ≈ 400 keV). The dashed lines above and below $E'_{\mathtt{x}} = E'_{\mathtt{y}}$ are at ± 24 keV, representing a $\Delta E \leq \pm 3\sigma_{\mathtt{x}_{16}}$ acceptance for this strip (see below). The low-energy thresholds are set to 40 keV, well above the pedestals of the strips. This strip was chosen as the example because it has the largest offset and smallest energy range as is evident by the saturated ADC readings at $E_{\mathtt{x}_{16}} \approx 725$ keV. In order to ensure that no biasing of the on-line data occurs due to

TABLE 4.4: DSSSD calibration fits of $E'_{\mathtt{y}_i} = \langle E_{\mathtt{x}} \rangle = \alpha_{\mathtt{y}_i} \times E_{\mathtt{y}_i} + \beta_{\mathtt{y}_i}$. These fits align the calibrations of the y-strips to the average calibrations of the (already corrected) x-strips.

strip	$\beta_{\mathtt{y}}$ (keV)	$\alpha_{\mathtt{y}}$ (keV/keV)	strip	$\beta_{\mathtt{y}}$ (keV)	$\alpha_{\mathtt{y}}$ (keV/keV)
1	7.02±0.11	0.9526±0.0006	13	12.80±0.10	0.8808±0.0005
2	4.53±0.11	1.0003±0.0006	14	10.84±0.10	0.9174±0.0005
3	6.63±0.10	0.9685±0.0006	15	5.55±0.10	0.9785±0.0006
4	9.76±0.10	0.9634±0.0006	16	11.40±0.10	0.9123±0.0005
5	6.36±0.10	0.9635±0.0006	17	6.43±0.10	0.9744±0.0006
6	11.04±0.10	0.9130±0.0005	18	2.84±0.11	1.0194±0.0006
7	6.80±0.10	0.9679±0.0006	19	1.77±0.11	1.0420±0.0006
8	5.86±0.10	0.9752±0.0006	20	10.67±0.10	0.9123±0.0005
9	1.20±0.11	1.0361±0.0006	21	10.57±0.10	0.9198±0.0005
10	6.13±0.10	0.9728±0.0006	22	9.42±0.10	0.9360±0.0006
11	5.10±0.10	0.9911±0.0006	23	10.74±0.10	0.9280±0.0006
12	3.46±0.10	1.0098±0.0006	24	7.95±0.11	0.9450±0.0006

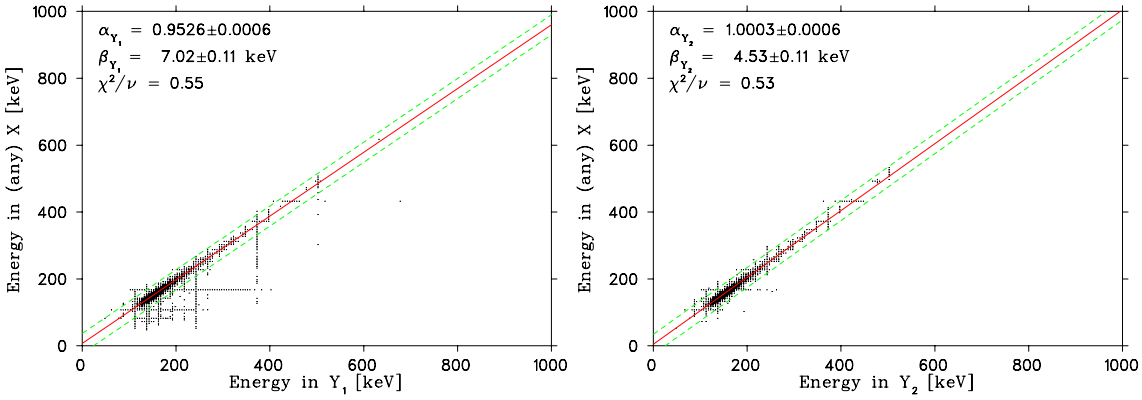

FIGURE 4.12: Comparison of the energy readings of strips $\mathtt{y}_1$ (left) and $\mathtt{y}_2$ (right) to that in x. The result of the fit yields $E'_{\mathtt{y}} = \alpha_{\mathtt{y}_i} E_{\mathtt{y}_i} + \beta_{\mathtt{y}_i}$ which aligns each y-strip to the average of the (already corrected) x-strips.

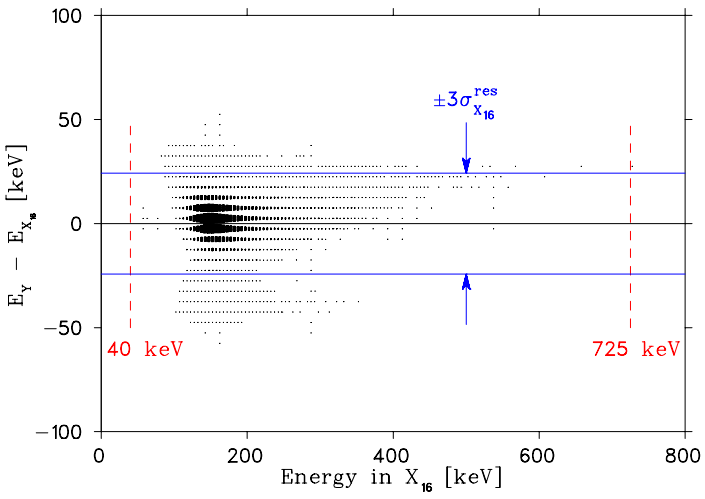

FIGURE 4.13: Plot of $E'_{\mathrm{x}16}$ vs. $\langle E'_{\mathrm{y}}\rangle - E'_{\mathrm{x}16}$ with the proposed thresholds for the on-line data indicated by the dashed lines. Strip x_{16} has the largest ADC offset and hence smallest energy range; the upper energy threshold needs be placed at 725 keV so as to ensure that no events are off the energy scale of this the most limited strip. The solid lines at ± 24 keV represent an $\hat{x}$-$\hat{y}$ energy agreement condition used to discrimate against noisy events.

such saturated energy readings, a high-energy threshold of at least 725 keV needs to be imposed; the threshold may be set lower to value of 400 keV so that the bias from the imperfect alignment of the calibrations is contained within the strips' resolution.

The resolution functions defined by:

$$R_{\mathrm{x}_i} \equiv (E'_{\mathrm{x}_i} - E'_{\mathrm{y}_j}) \qquad \text{and} \qquad R_{\mathrm{y}_i} \equiv (E'_{\mathrm{y}_i} - E'_{\mathrm{x}_j}) \tag{4.4}$$

were generated and a sample of them are depicted in Figure 4.14. The fact that the Gaussian fits agree reasonably well over the peaks of the distributions, and that they are nearly centered around zero, is very encouraging. This indicates that the resolution of the strips is dominated by random processes and that the strip calibrations are consistent. The widths of these Gaussian fits, listed in Table 4.5), average 8.1 keV. The (relatively) large tails of the edge strips, however, show that they suffer from additional systematic effects. Since these tails are not a large percentage of the events, the edge strips can be included in a final analysis, but one might wish to consider excluding these events if statistics is not a concern.

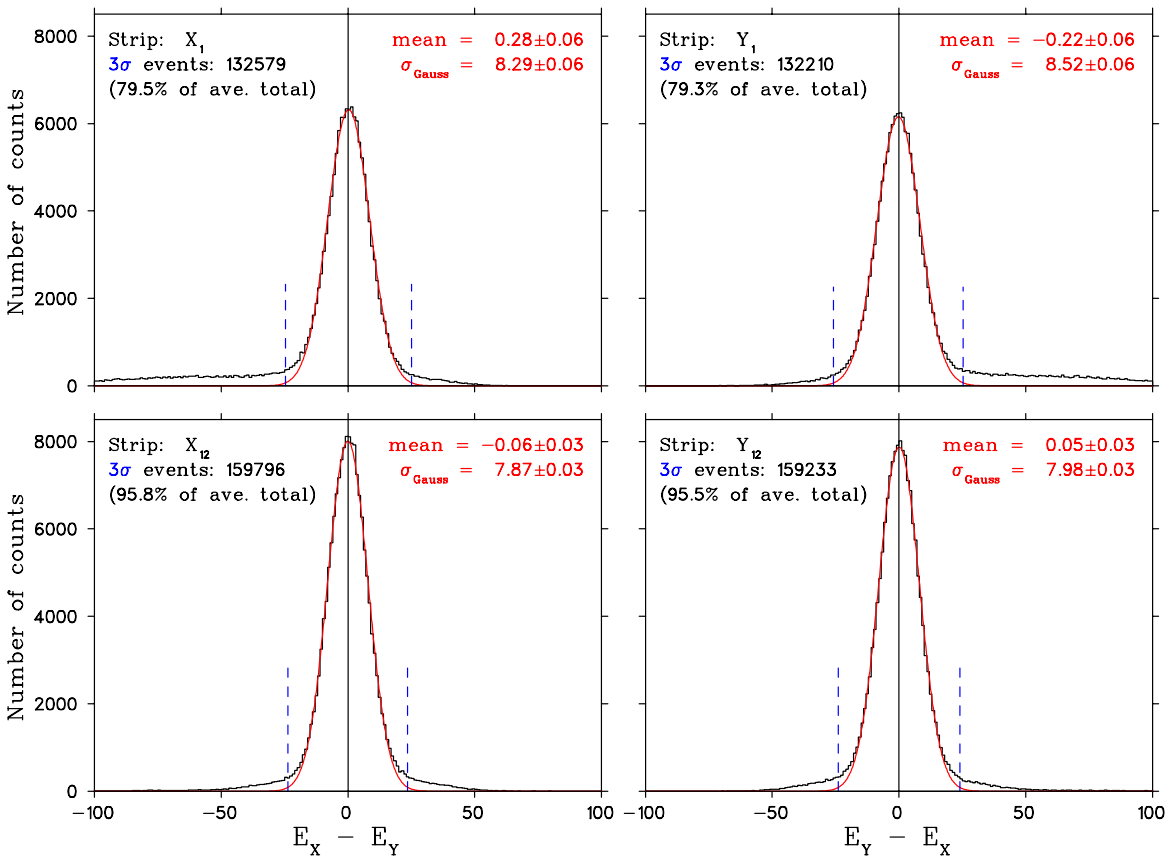

FIGURE 4.14: Overall resolution functions for strips $\mathtt{x}_1$, $\mathtt{x}_{12}$ (left), $\mathtt{y}_1$ and $\mathtt{y}_{12}$ (right). The resolution is calculated as $R_{\mathtt{x}_i} = (E'_{\mathtt{x}_i} - E'_{\mathtt{y}_j})$ and $R_{\mathtt{y}_i} = (E'_{\mathtt{y}_i} - E'_{\mathtt{x}_j})$. The dashed lines are at $\pm 3\sigma$ of the Gaussian fit (solid line), which fit well over the peak of the distributions; the $\mathtt{x}_1$ and $\mathtt{y}_1$ have especially large tails arising from edge effects.

TABLE 4.5: Final widths of the DSSSD energy readings by comparing x and y energy readings. The average widths are $\langle \sigma_{\mathtt{x}} \rangle = 8.07 \pm 0.18$ and $\langle \sigma_{\mathtt{y}} \rangle = 8.08 \pm 0.18$ keV.

strip	σ_{DSSSD} [keV] x-strips	y-strips	strip	σ_{DSSSD} [keV] x-strips	y-strips
1	8.29±0.06	8.52±0.06	13	7.76±0.03	7.72±0.03
2	8.14±0.04	8.57±0.04	14	7.80±0.03	7.81±0.03
3	8.10±0.04	8.20±0.03	15	7.94±0.03	8.02±0.03
4	8.14±0.04	8.27±0.04	16	8.18±0.03	8.00±0.03
5	8.07±0.03	8.18±0.04	17	8.18±0.03	8.05±0.04
6	8.04±0.03	8.00±0.03	18	8.07±0.03	8.12±0.04
7	7.96±0.03	8.06±0.03	19	8.17±0.03	8.28±0.03
8	8.00±0.03	8.09±0.03	20	8.24±0.03	8.04±0.04
9	7.97±0.03	8.03±0.03	21	8.21±0.04	8.09±0.03
10	8.03±0.03	8.04±0.03	22	8.35±0.04	8.09±0.04
11	7.89±0.03	7.92±0.03	23	8.36±0.04	8.24±0.04
12	7.87±0.03	7.98±0.03	24	8.96±0.07	8.29±0.06

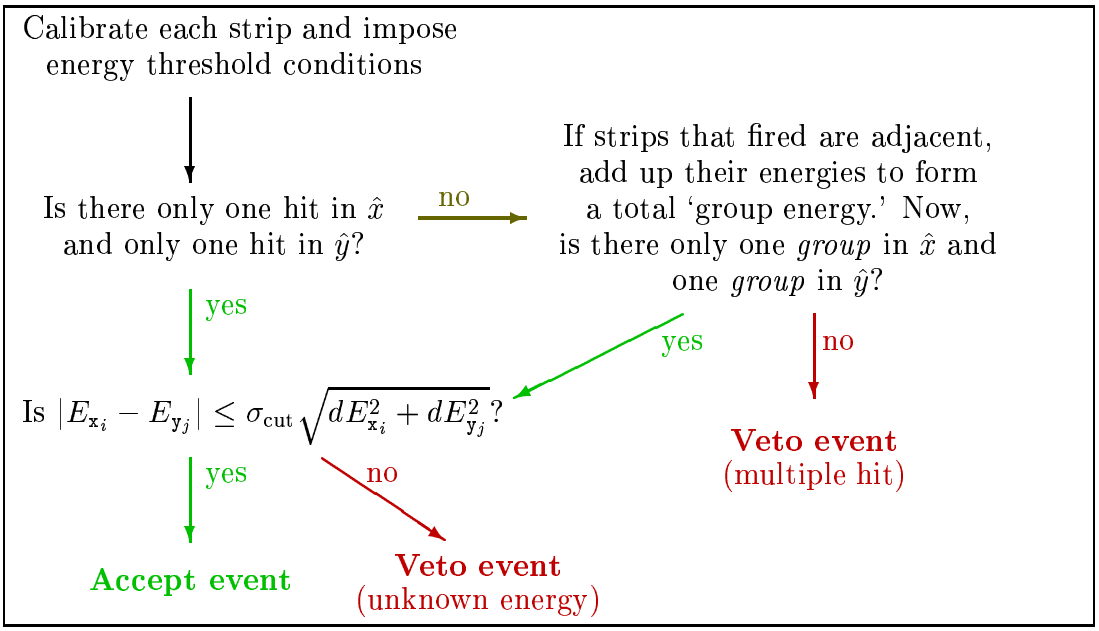

FIGURE 4.15: Block diagram of the DSSSD analysis scheme. Essentially, we simply require that events in the strip detector are consistent with a single hit, and that the energy deposited in the two sides ($\hat{x}$ and $\hat{y}$) agree to within the resolution of the strips.

4.2.5 Position Decoding and Analysis Scheme

The analysis scheme developed for the DSSSD relies on two important premises: (*i*) a 'good' event is one where only one pixel, a single hit in $\hat{x}_i$ and one in $\hat{y}_j$, fired and (*ii*) the energy reading in $\hat{x}$ is consistent with the energy reading in $\hat{y}$. The first ensures that one particle went through the detector only once (in particular discriminating against βs that backscattered out of the scintillator), while the second is a necessary condition for a final energy reading. A summary of this analysis scheme is given in Figure 4.15.

The fact that the strips are calibrated allows us to impose energy threshold conditions that applies equally to all strips. The first of these conditions is a low-energy 'strip threshold' that is placed well above the hardware (triggering) thresholds, and any strip whose energy is greater than this is considered to have fired. Ideally (indeed most likely), only one strip in $\hat{x}$ and one strip in $\hat{y}$ passes this condition giving us an event at $x_{\text{pos}} = (i - 12.5)$ mm, $y_{\text{pos}} = (j - 12.5)$ mm where i, j represent the strip

number of the x- and y-strips that fired. We would like to make this threshold as low as possible, but we must make sure that it is high enough that we don't have strips firing due to a random fluctuation above their respective pedestals; if this happens we will veto legitimate events as (phantom) multiple hits. With condition (i) satisfied and the position of the hit known, we now need to determine the energy the particle deposited using the two energy readings. As mentioned earlier, the energy in $\hat{x}$ should be the same as $\hat{y}$ to within the resolution of the individual strips, so we check to make sure that they pass an energy agreement condition:

$$\Delta E_{\mathrm{DSSSD}} \equiv |E_{\mathtt{x}_i} - E_{\mathtt{y}_j}| \leq \sigma_{\mathrm{cut}} \sigma_{\mathrm{DSSSD}} \tag{4.5}$$

where

$$\sigma_{\mathrm{DSSSD}} \equiv \sqrt{dE_{\mathtt{x}_i}^2 + dE_{\mathtt{y}_j}^2} \tag{4.6}$$

and σ_{cut} is an adjustable (user) parameter that determines how tight this energy agreement must be. The $dE_{\mathtt{x}_i}$, $dE_{\mathtt{y}_j}$ are the 1σ widths of the resolution functions, as given in Table 4.5. If this condition is true, then we take the final DSSSD energy reading to be the average of the two calculated energies weighted by their respective widths:

$$E_{\mathrm{DSSSD}} = \frac{E_{\mathtt{x}_i}/dE_{\mathtt{x}_i}^2 + E_{\mathtt{y}_j}/dE_{\mathtt{y}_j}^2}{1/dE_{\mathtt{x}_i}^2 + 1/dE_{\mathtt{y}_j}^2} \tag{4.7}$$

Events that do not satisfy (i) are not immediately vetoed because we expect that βs will occasionally be scattered into an adjacent strip. For this reason if two strips fired in, say x, instead of just one, we check to see if they were $\mathtt{x}_{\mathrm{i}}$ and $\mathtt{x}_{\mathrm{i}\pm1}$. If so, we add up the energies deposited in each and weight the position of the hit according to the energy deposited in each, *i.e.*

$$E_{\mathtt{x}} = E_{\mathtt{x}_i} + E_{\mathtt{x}_{i\pm1}} \tag{4.8}$$

and

$$x_{\mathrm{DSSSD}} = \frac{(i - 12.5)E_{\mathtt{x}_i} + (i - 12.5 \pm 1)E_{\mathtt{x}_{i\pm1}}}{E_{\mathtt{x}_i} + E_{\mathtt{x}_{i\pm1}}} \text{ mm} \tag{4.9}$$

In this way we define 'group' hits which are treated the same as single strip events: if there was one *group* in x as well as one in y, we then check for energy agreement between the *group* energy readings and accept the event if it passes.

The most sensitive test of the setting of the strip threshold is again through use of the on-line ^{38m}K data themselves; the x- and y-strip positions, combined with the relative number of single-pixel versus multiple strip events, indicates good noise discrimination without a loss of good events. Figure 4.16 is a plot of the x_{DSSSD} position for events in which there was one (group) hit in $\hat{x}$ and a corresponding one in $\hat{y}$ which passed the $\Delta E_{\mathrm{DSSSD}} \leq 3\sigma_{\mathrm{DSSSD}}$ energy agreement condition. The large peaks of the individual strips (i.e. where no adjacent strip passed the strip threshold) reflect the consistency of the x- and y-strip calibrations. A poor alignment causes the energy condition (Equation (4.5)) to veto more events, the number of which would depend on how misaligned a given strip's calibration is compared to the average of the other side's; this is seen in the position spectrum when the initial off-line calibrations were used (dashed line, slightly offset for clarity). The extended calibrations can be seen to remedy this situation by making these peaks much more homogeneous. Almost 7% of the events that would otherwise be vetoed are retrieved once the strip calibrations are properly aligned and, more importantly, the efficiency of the DSSSD is much more uniform across the strips.

The distribution of the inter-strip events is less sensitive to the relative consistency of the calibrations; the shape of the distributions for the off-line and extended calibrations is very similar as seen in Figure 4.16. These events are, however, sensitive to the applied strip threshold; if set too low, a strip adjacent to where the β left (all of its) charge is more likely to fire from random fluctuations above threshold. This will bias the shape of the inter-strip events towards having too many events just below the main single-strip peak (there is not a corresponding bias just above because of the choice of binning in this figure accentuates the very low E_{i-1}, while the corresponding E_{i+1} is absorbed in the main peak). Alternatively, if the threshold is too high, we would also see an overall loss of events because the cases where only a small fraction of the charge went into the adjacent strip would be less likely to pass. For example, if 100 keV is deposited in $\mathtt{x}_i$ and 40 keV in $\mathtt{x}_{i+1}$ (with the full 140 keV in $\mathtt{y}_j$), a threshold of > 40 keV would not add back the $\mathtt{x}_{i+1}$ energy back and may veto

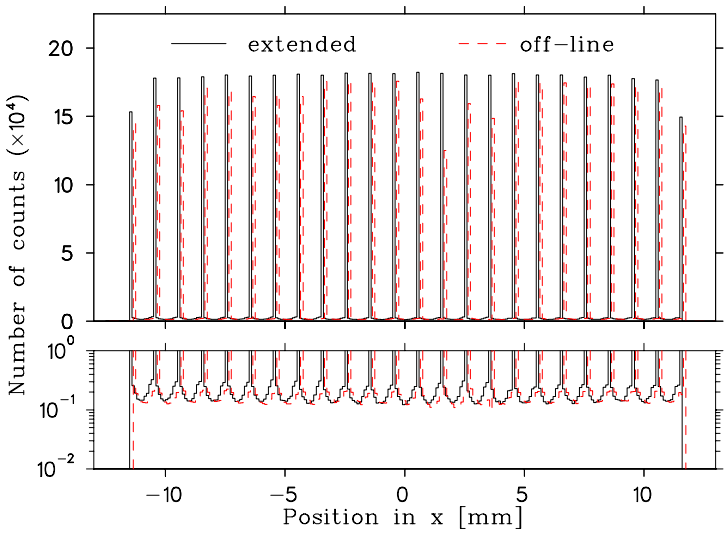

FIGURE 4.16: Position of DSSSD β hits in $\hat{x}$ from the on-line ^{38m}K data. The dashed line corresponds to the initial photon calibration while the solid uses the extended calibration. Note the improved homogeneity in the number of counts of the individual strips (linear scale, above) as well as the symmetry of the inter-strip hits (logarithmic scale, below). The corresponding spectra for $\hat{y}$ shows similar characteristics.

the event since $E_{\mathtt{x}_i} \neq E_{\mathtt{y}_j}$. Thus, too high a threshold suppresses events near $(i \pm \delta)$ where $\delta < 0.5$, but will not seriously affect events near the midpoint since these leave nearly equal amounts in each. The shape of the inter-strip events (averaged over all x-strips) are plotted in Figure 4.17 and shows how the data are affected by the value of the low-energy strip threshold. The fits, which are to a quadratic function, are all in agreement with the data except for the last point; the 20 keV threshold is too low because it allows too many events here while the 65 keV one is clearly too high. Between these two thresholds, the shape and even the overall number of counts is seen to be relatively insensitive to the value used. The large 65 keV threshold is clearly excluding events where a small (but real) amount of charge was deposited in an adjacent strip. By looking at plots similar to Figure 4.16, but with finer steps in the low-energy threshold, it was found that the inter-strip distributions were constant over the range $35 - 55$ keV. The results contained within this thesis all use a low-energy threshold of 40 keV.

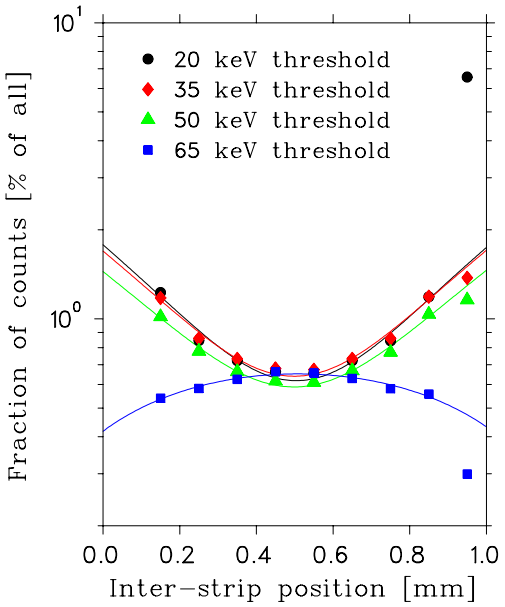

FIGURE 4.17: Average position of inter-strip DSSSD events using different low-energy thresholds. When the threshold is too low (20 keV), we see too many events below the single-strip peak and if set too high (65 keV), events to either side of the main peaks are reduced. The lines are quadratic fits to all but the last point.

4.2.6 ^{38m}K Results

As mentioned in §4.2.1, a charged particle such as a relativistic positron loses energy through multiple Coulomb scattering, which is an inherently random process. The energy deposited by the positron will depend on the angle(s) it is scattered into and how long the random walk through the detector is; the energy density distribution follows a Vavilov distribution [56] which contains a large peak corresponding to particles which suffer only small angle scattering, as well as a high-energy tail for the ones whose random walk through the detector is relatively large.

The on-line ^{38m}K data in Figure 4.18 show the final DSSSD energy reading as analyzed according to the scheme outlined in §4.2.5, and are compared to a GEANT simulation. The Monte Carlo has been renormalized so that the peaks of the two spectra are equal. Both the simulation and the data have the following conditions imposed:

- a 40 keV low-energy DSSSD threshold (from the previous section).

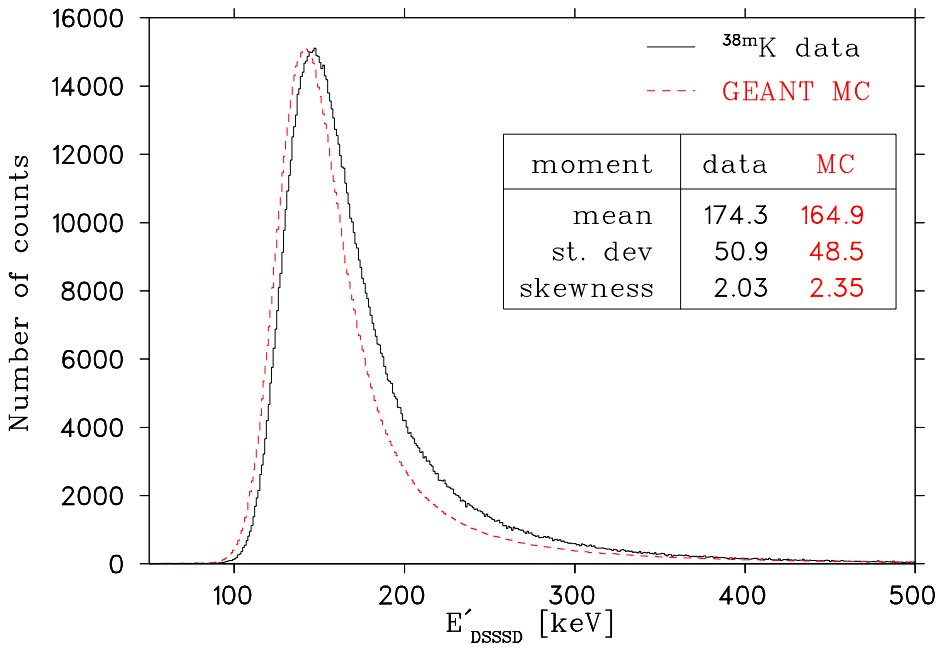

FIGURE 4.18: DSSSD energy spectrum of the on-line ^{38m}K (solid line, all strips) and the comparison to GEANT simulations (dashed). The first three moments of both distributions are given to characterize the differences.

- a 500 keV high-energy DSSSD cutoff (to reduce bias as noted for Figure 4.13).
- an $E_{x_i} - E_{y_j}$ energy agreement condition using $\sigma_{\text{cut}} = 3$.
- a 2500 keV low-energy scintillator threshold[†]

There is a clear discrepancy between the experimental data and GEANT with a > 10 keV difference in their average energy losses; the table in the figure lists the first, second and third moments of the two distributions. The sharp rise on the low-energy side of the peaks agrees (up to a constant shift) and this shows that the simulated data have had the detector resolution properly incorporated. The high energy side of the peak is clearly sharper in GEANT, and this may be indicative of an underestimate in the number (or angle) of scatters within the DSSSD. Part of the problem may arise from the extended calibration corrections (of §4.2.3), and simply be a problem with

[†]this condition on the E detector's energy reading eliminates the ^{38}K ground state γ contamination, which is not included at this stage of the analysis (see §4.3.5 and beyond).

the overall calibration. Spectra of the individual strips are all aligned by virtue of the resolution functions being centered about zero, and therefore the data are not wider due to strip calibration variations. If the difference were solely due to the overall calibration, then it could be corrected by fitting the data to the MC, with the energy scale free to vary. Attempts to do this did not fully correct the situation as the high-energy side of the peak remained underestimated, so it is more than just the calibrations.

At this time, we do not fully understand this difference, but we do know that in relation to the telescope's total $E + \Delta E$ energy reading, this discrepancy is very small: at 1 MeV, the average difference is only 1% of the total and it is only 0.2% at 5 MeV. The impact on simulations of the scintillator's spectrum, which must include the energy lost in DSSSD, is discussed in §4.4.1, and §4.3.5 shows that the total energy spectrum is well reproduced if the average difference is considered. It is therefore not crucial that we resolve the discrepancies found within this section, but improvements can be made in the understanding of this device if more careful calibrations are made. The full energy peak of a conversion electron source, such as ^{207}Bi, would help to provide a cleaner initial calibration which would make the extended calibration easier and presumably involve smaller corrections. The source must, however, be open (unlike the one used throughout this thesis) so that the electrons do not suffer (much) energy straggling before entering the DSSSD.

4.3 The Plastic Scintillator

This part of the β-telescope is important to TRINAT's β decay experiments because it provides the (majority of the) energy measurement of the emitted positron and the time of the event relative to the recoil detector. It has been my hope from the start of my studies to design and optimize the scintillator well enough that the energy and timing resolutions do not limit our measurement of the correlation parameter. The timing of the scintillator will be shown to be good enough that our recoil time-of-flight measurement is limited by the trap size. Preliminary tests [57] of our sensitivity to uncertainties in the calibration of the gain indicate that $\Delta\sigma_a = 0.1\%$ for a 0.1% change in the slope of the gain. As anyone who has worked with βs will appreciate,

this represented a formidable task.

4.3.1 Optimization

The block diagram of Figure C.1 in Appendix C (page 128) outlines the scintillator's electronics. The energy signal is taken from the dynode output of the PMT and inverted through a LeCroy 428F linear fan in/out. The anode provides the timing signal to the Tennelec 455 constant fraction discriminator which is used to set the scintillator's hardware threshold to approximately 300 keV. The stabilization unit, discussed in greater detail later (see §4.3.4), minimizes gain variations by monitoring a LED's pulse-height in the PMT.

Once the scintillator and its electronics were assembled, tests were performed to determine the wrapping that would best collect light in our geometry. The wrapping of the scintillator can be broken up into two areas: the front face of the plastic, and the wrapping around the side of the scintillator and light guide. For the front face, extra care was taken to minimize the energy straggling of positrons as they enter the scintillator. To that end, ^{207}Bi spectra obtained using a Si detector were compared when sheets of different wrappings were placed in front it. ^{207}Bi decays via orbital electron capture [58] giving two mono-energetic internal conversion electrons at 975.6 and 1048.1 keV, which are resolvable with the Si detector. Comparison of the energy loss effects of different wrappings and thicknesses could then be made using the peak-to-valley ratio of these two peaks. This was done for aluminized mylar (Al on $C_5H_4O_2$), Teflon (CF_2=CF_2), white paper and Tetlar[†], the results of which indicated that Teflon [59] caused the least amount of energy loss and straggling.

Figure 4.19 shows the spectra of a ^{207}Bi source using a few of the wrapping schemes considered. Once again, the diffuse reflector Teflon was found to be best suited for our geometry because it was with this wrapping that we observed the largest signals. One can see that Teflon around the sides clearly yields better overall light collection compared to Al mylar. With Al mylar only on the front face, the same overall gain is observed as the Teflon (once enough layers was applied), but one can also see the

[†]This is normally used to keep scintillators light-tight, but these tests indicated that it adds to the energy straggling of the incident particle and so was not used.

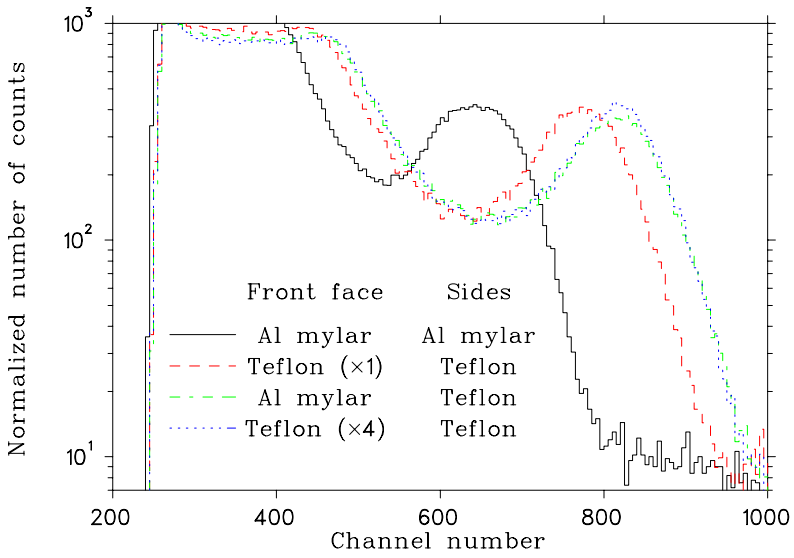

FIGURE 4.19: ^{207}Bi spectra using different scintillator wrapping schemes. The Teflon wrapping around the sides of the scintillator and light guide can be seen to provide the greatest light collection; aluminized mylar on the front face yields the same light collection efficiency, but Teflon minimizes the energy straggling of the electrons as they enter the scintillator.

energy straggling effects in the electron conversion peak. For this reason, the final wrapping of the plastic and light guide was done entirely with Teflon (as specified in GEANT's geometry on page 42).

4.3.2 Timing

Good timing resolution between the recoil and β detectors is essential for accurately determining the recoil momentum from its time-of-flight. To understand the timing characteristics of the scintillator, tests were performed with another scintillator ($\varnothing$4 cm $\times$ 4 cm) using a ^{22}Na source. When placed between the two scintillators, the back-to-back annihilation radiation from the β^+ decay of this source allows a measure of the relative timing between the two detectors. The resulting timing peak had a FWHM = 0.9 ns which, assuming both scintillators have equal timing, gives a $\sigma_{\text{scin}} \approx 0.4$ ns.

It is the relative timing of the scintillator with that of the recoil detector that is relevant to the experiment and, since the MCP does have a small efficiency for

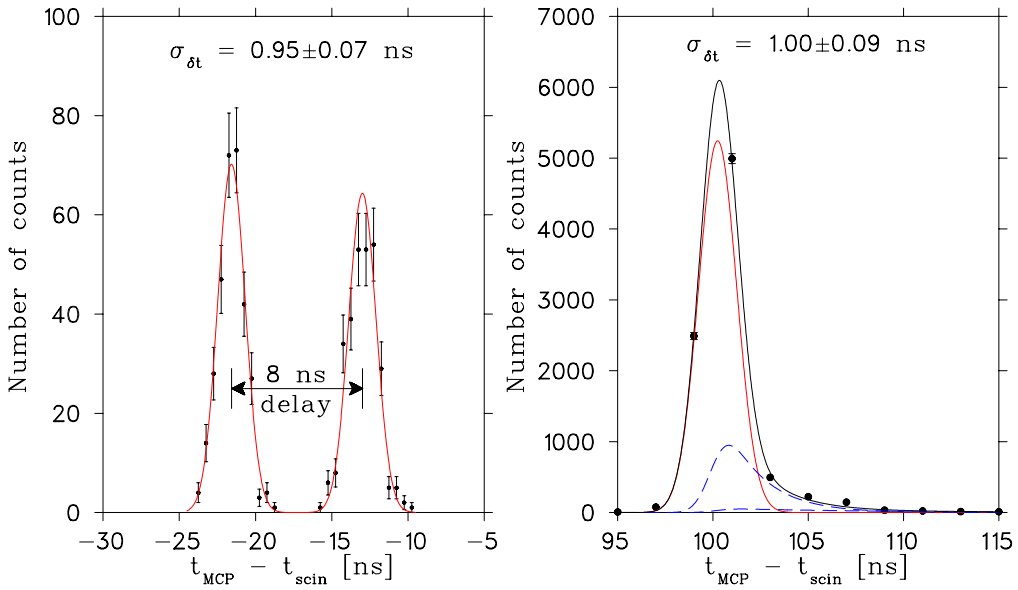

FIGURE 4.20: Relative timing between the β-telescope and the recoil detector using an ^{88}Y source (left) and the on-line data (right). Both fits yield a scintillator-MCP timing resolution of $\sigma_{\delta t} \approx 1$ ns.

detecting γs, tests using a ^{88}Y source were made using the essentially coincident emission of the 898 and 1836 keV lines. An 8 ns delay cable was added to the scintillator's timing half-way through the test in order to allow an easy channel-to-time calibration. The results of a double-Gaussian fit to the two peaks are depicted in Figure 4.20 (left) and give a relative scintillator–MCP timing, $\sigma_{\delta t}$, of about 1 ns.

The timing from scintillator–MCP coincidences in the on-line data contains, in addition to the Ar recoils, a peak at zero TOF. This 'prompt peak' (right of Figure 4.20) is thought to arise from events where one of the annihilation γs hits the recoil detector; if an electron is ejected in one of the channels, the MCP will register it as a hit. The prompt peak's energy spectrum in the scintillator is badly distorted towards lower energy, indicating that the other annihilation quantum is what predominantly fired the β-telescope[†]. The events above 511 keV probably correspond to the positron backscattering off the MCP and then into the telescope (the transit time for a relativistic β is 0.35 ns).

The tail at longer TOF (103–110 ns) may come from events where the positron

[†]A DSSSD coincidence *is* required in this timing spectrum.

fires the β-telescope and this time a low-energy photon produced by the decay fires the MCP. The daughter Ar^0 atom has a good probability of being left in an excited state (11 eV) after the β decay; these excited states decay to the ground state by the emission of a UV photon.

The fit to the prompt peak is a Gaussian plus two exponential tails with decay times of 2 and 8 ns (for the atomic excited states), all with free normalizations. This fit agrees with the ^{88}Y measurement and so we take our detector TOF resolution to be $\sigma_{\mathrm{TOF}} = 1$ ns.

In the $\beta - \nu$ experiment, the resolution of the deduced energy of the recoil is dependent not only on the relative timing of the detectors, but also on where the decay occurred. The size of the trap affects the uncertainty in the position of the decay (which is assumed to be the trap center) and hence the distance the recoiling atom transverses before firing the MCP. With the typical trap dimension of 0.5 mm along the detector axis and considering the fastest recoils ($Ar^{+4,+5,\cdots}$), this effect adds a ± 4 ns 'time jitter' which is greater than the detectors' relative timing resolution. The timing characteristics of the β-telescope are therefore adequate for the energy measurement of the recoil by TOF. If the trap size can be reduced by a factor of four, however, the uncertainty in the scintillator's timing will become significant. Another reason for trying to improve the timing resolution is to use the ^{38m}K measurement to *deduce* the trap size; this could then be compared to that obtained using a CCD camera, which is not without its own systematic errors.

4.3.3 Energy Calibration and Resolution

The largest systematic uncertainty in the $\beta - \nu$ experiment introduced by the β-telescope is the energy calibration of the plastic scintillator, and therefore considerable effort was directed toward understanding it as completely as possible. Unfortunately, a well-characterized source of mono-energetic positrons between 1 and 5 MeV is not readily available at TRIUMF, so the calibration was done by fitting the Compton edges of various γ sources.

The analysis of the Compton spectra was performed using two schemes: fitting the data analytically to the Klein-Nishina formula, as well as fitting to a Monte

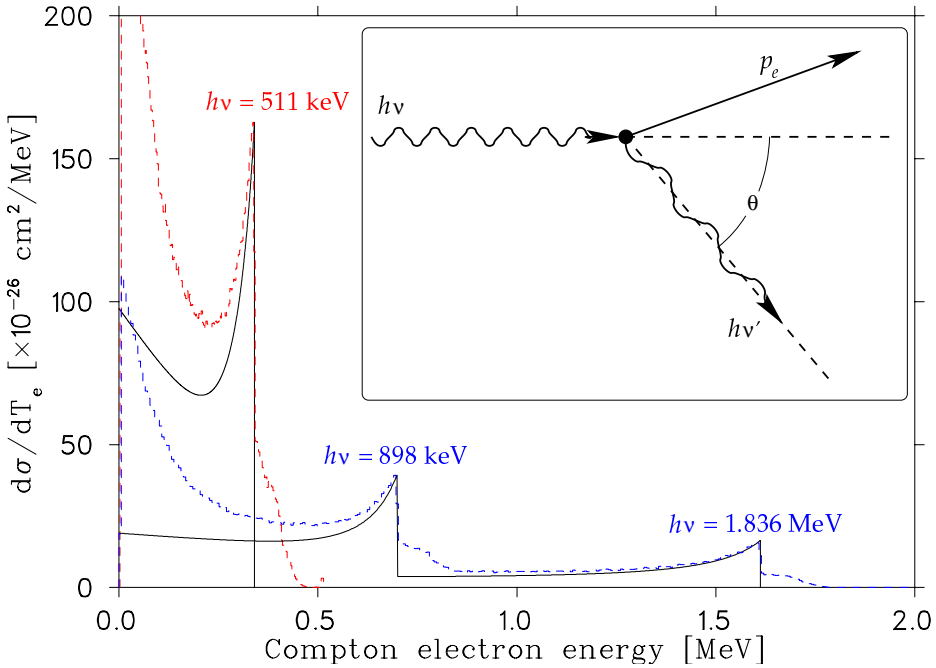

FIGURE 4.21: Kinematics of the Compton effect and the energy spectrum of the Compton scattered electron for an ^{88}Y source ($E_\gamma = 0.898$ and 1.836 MeV) and an annihilation quanta ($E_\gamma = 511$ MeV). The solid line is the Klein-Nishina calculation and the dashed lines represent GEANT simulations.

Carlo simulation. Agreement between the two methods served as a consistency check, but the detailed analysis was limited to the Monte Carlo fit since the analytical formula does not include multiple scattering, surface effects, δ rays, and other effects contributing to the low-energy tail below the Compton edge.

The energy calibration is assumed to be linear (see §A.1) so that the observed pulse height, $x_{\rm ADC}$, can be calibrated using:

$$x_{\rm ADC} = x_\circ + \lambda T_{\rm scin} \tag{4.10}$$

Here $x_\circ$ is the ADC offset and λ has units of channels/keV.

The dominant component to the spectrum of γ's in plastic is the Compton effect (*cf.* photoabsorption in a Ge(Li) or NaI scintillator) which is the inelastic scattering of a γ off an atomic electron (assumed to be free) as depicted in Figure 4.21. The energy of the Compton electron follows from energy-momentum conservation and depends

only on the direction of the scattered photon:

$$T_e = \frac{\gamma^2(1-\cos\theta)m_e c^2}{1+\gamma(1-\cos\theta)} \tag{4.11}$$

with $\gamma = E_\gamma/m_e c^2$. The photon will transfer the greatest energy when it backscatters ($\cos\theta = -1$) so that the maximum energy in the Compton spectrum occurs at the so-called 'Compton edge':

$$(T_e)_{\max} = \frac{E_\gamma}{1+m_e c^2/2E_\gamma} \tag{4.12}$$

To calculate the differential energy spectrum of the Compton electrons, we turn to the quantum mechanical calculation of Klein and Nishina [60]. Letting $s = T_e/E_\gamma$, the result is:

$$\frac{d\sigma_{\text{comp}}}{dT_e} = \frac{\pi r_e^2}{m_e c^2 \gamma^2}\left[2 + \frac{s^2}{\gamma^2(1-s)^2} + \frac{s}{1-s}\left(s - \frac{2}{\gamma}\right)\right] \tag{4.13}$$

where $r_e = e^2/4\pi\epsilon_\circ m_e = 2.818$ fm is the classical electron radius. GEANT uses Equation (4.13) to simulate Compton scattering, and one can see the comparison of the Klein-Nishina formula with simulations in Figure 4.21. The extra bump at energies above the Compton edge arise from events where the γ has scattered more than once within the scintillator. A larger low energy tail is evident due to particles escaping before depositing their full energy as well as from electrons that Compton scattered from various neighboring volumes before entering the scintillator. The effects of bremsstrahlung in the low Z scintillator at these energies is small (see Figure A.3), but is calculated in the Monte Carlo.

The final fitting function for the γ calibrations needs to account for the resolution of the scintillator which depends on the number of generated scintillation photons, the number of these collected on the photocathode, noise in the electronics and inhomogeneities in the plastic. If we assume that the width is dominated by photon statistics and is therefore Gaussian, we use a function of the form [61]:

$$\sigma^2_{\text{scin}}(T_{\text{scin}}) = \sigma^2_\circ + \mu \cdot T_{\text{scin}} \tag{4.14}$$

where μ and $\sigma_\circ$ have units of keV. The noise introduced by the electronics, $\sigma_\circ$, is reflected in the peak observed when the scintillator does not fire (the pedestal).

The distribution used to fit the γ calibrations is the convolution of the Monte Carlo simulation with the resolution, Equation (4.14), i.e.:

$$F_{\rm comp}(x_{\rm ADC}, \sigma_{\rm scin}) = \int_0^{T_e(x_{\rm max})} \left(\frac{d\sigma_{\rm comp}}{dT_e}\right) \exp\left[-\frac{\left(T_e(x_{\rm ADC}) - \epsilon\right)^2}{2\sigma_{\rm scin}^2}\right] d\epsilon \qquad (4.15)$$

The parameters free to vary in the fit to data are the energy calibration ($x_\circ$, λ) and the width of the resolution ($\sigma_\circ$, μ). The overall normalization is fixed such that the data and simulation have an equal number of counts over the fitting range. Fits to ^{88}Y are given in Figure 4.22 and are seen to agree well when the fitting range is limited to just the Compton edge itself (top and middle; the arrows denote the low- and high-energy limits of the fitting range). The events above the Compton edge arise from cases where the γ Compton scattered more than once in the plastic, and this effect is generally reproduced in the MC; for the low-energy γs (511 of ^{22}Na and ^{137}Cs), the MC does not do as good a job. The fit to the whole spectrum (bottom) is not reproduced as well, and the resolution is forced to increase to help compensate for this fact. Note, however, that when both edges are included, the offset and slope can be simultaneously fit and that the fit values for the calibration do not change much. The correlations between these parameters (as well as $\sigma_\circ$ and μ), however, are as large as 90%; the results can depend strongly on the initial guesses for their values and so the results are not reliable. We must therefore fix the offsets $x_\circ$ and $\sigma_\circ$ when fitting the spectra and should only fit over the Compton edge itself where the MC reproduces the data well. As an initial guide, the parameters $x_\circ$ and $\sigma_\circ$ are taken to be the centroid and width of the pedestal.

The channel number, $x_{\rm ADC}$, and width, $\sigma_{\rm scin}$, at each $(T_e)_{\rm max}$ are calculated using the fits to λ and μ from the γ sources: ^{22}Na, ^{60}Co, ^{88}Y and ^{137}Cs. These six points[†] are then used to fit Equations (4.10) and (4.14) which then give the first iteration of the calibrations: $x'_\circ$, λ', $\sigma'_\circ$ and μ'. In this case, the offsets, $x_\circ$ and $\sigma_\circ$, *are* free to vary and so are fit, even though in fitting the actual γ spectrum they are always fixed. The γ spectra are then re-fit with these new values of the offsets fixed, and the whole calibration process is repeated. This iterative method is continued until changes in the fit values become negligible.

[†]The two lines in ^{60}Co are not resolved by the scintillator and so only constitute one fitting point.

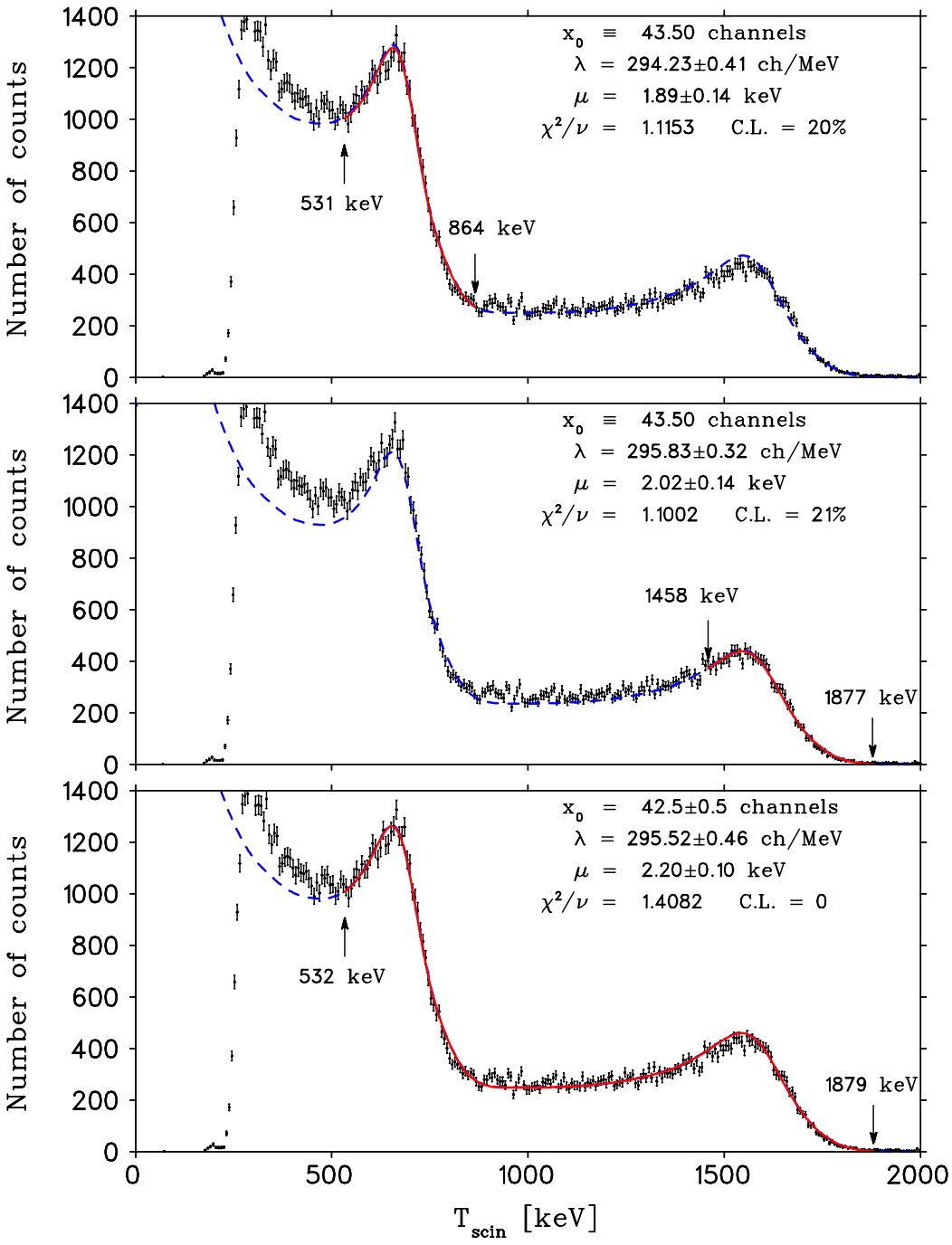

FIGURE 4.22: Fits of a ^{88}Y Compton spectrum to a GEANT simulation. The fits are to the 898 keV γ (top), the 1836 keV γ (middle) and the whole spectrum (bottom). The solid line is the MC over the fitting range (indicated by the arrows) and the dashed shows the rest of the MC spectrum.

Source	$(T_e)_{\max}$ [keV]	λ [channel/MeV] $x_\circ \equiv 38.79$	μ [keV] $\sigma_\circ \equiv 5.193$	χ^2/ν	$x_{\rm ADC}$ [channel]	$\sigma_{\rm scin}$ [keV]
^{22}Na	340.67	311.23 ± 0.70	1.54 ± 0.18	2.155	144.82 ± 0.38	23.5 ± 0.9
	1062.15	300.25 ± 0.24	1.68 ± 0.17	1.263	357.70 ± 0.39	42.5 ± 3.1
^{60}Co	1040.74	301.96 ± 0.26	1.85 ± 0.12	2.080	353.05 ± 0.40	44.2 ± 1.4
^{88}Y	699.11	301.79 ± 0.63	1.85 ± 0.30	1.221	249.77 ± 0.53	36.3 ± 5.3
	1611.71	299.10 ± 0.50	1.84 ± 0.15	1.057	520.85 ± 0.85	54.8 ± 3.7
^{137}Cs	477.65	305.59 ± 0.90	1.64 ± 0.13	3.02	184.66 ± 0.52	25.6 ± 1.2
Results of 1st iteration: $x'_\circ = 43.5 \pm 0.9$, $\lambda' = 296.3 \pm 1.0$, $\sigma'_\circ = 0.0$ and $\mu' = 1.77 \pm 0.07$						
^{22}Na	340.67	294.48 ± 0.34	1.59 ± 0.17	1.327	143.82 ± 0.32	23.2 ± 1.8
	1062.15	295.34 ± 0.16	1.87 ± 0.17	1.223	357.20 ± 0.35	44.6 ± 3.0
^{60}Co	1040.74	295.87 ± 0.16	2.03 ± 0.10	1.534	351.43 ± 0.35	46.0 ± 1.3
^{88}Y	699.11	295.01 ± 0.26	1.48 ± 0.15	1.182	249.75 ± 0.35	32.2 ± 2.5
	1611.71	296.05 ± 0.24	1.83 ± 0.12	0.977	520.64 ± 0.48	54.3 ± 2.9
^{137}Cs	477.65	295.71 ± 0.13	1.40 ± 0.13	1.624	184.65 ± 0.31	25.9 ± 1.3
Results of 2nd iteration: $x''_\circ = 43.0 \pm 0.3$, $\lambda'' = 296.2 \pm 0.4$, $\sigma''_\circ = 0.0$ and $\mu'' = 1.78 \pm 0.12$						

Table 4.6: γ calibration of the scintillator for April 1999 following the scheme outlined in the text. For each iteration, the varied parameters are λ and μ, whose fit values are used to calculate $x_{\rm ADC}$ and $\sigma_{\rm scin}$ at each $(T_e)_{\max}$. Using these six points, fits to Equations (4.10) and (4.14) give the energy calibration and resolution. For the second iteration, the offsets $x_\circ$ and $\sigma_\circ$ are fixed to the first iteration's results.

Table 4.6 lists the results of such fits for two iterations of a calibration for the April 1999 experimental run. The fit to the calculated $x_{\rm ADC}$ of the 2$^{\rm nd}$ iteration and the residual plot are given Figure 4.23. If we are interested in calculating the energy for a given channel number, the calibration in the figure is expressed as:

$$T_{\rm scin} = (3.376 \pm 0.005 \text{ keV/chan}) \times x_{\rm ADC} \; - \; (145 \pm 3 \text{ keV}) \qquad (4.16)$$

The solid lines in the residual plot are the uncertainties in the calibration as given by the above expression. The discrepant point at $(T_e)_{\rm max} = 1.94$ MeV is from the Compton edge of the ^{38}K 2.2 MeV γ. This Compton edge could not be fit well because of the large $^{38{\rm m}}$K 'background' which needed to be included in the fit; as will be mentioned later, there appears to be a 2% discrepancy in the scintillator response between γs and βs and so simultaneously fitting the β spectrum will necessarily bias the Compton edge fit. This point was therefore not included in the fit to the calibration.

Over the limited range that the γ sources cover, and neglecting the poor ^{38}K result, the scintillator is found to be linear and calibrated to within $\pm$4 keV. Indeed, since the experimental region of interest extends out to 5 MeV, we still must be concerned about the linearity at higher energies. A ^{241}Am/Be source is normally used for the neutrons it produces via the $^{9}{\rm Be}(\alpha, n)^{12}{\rm C}$ reaction, but attempts were made to use it as a 4.44 MeV γ source from when carbon atoms left in the excited state decay back to the ground state. The neutron background, much like with the ^{38}K, made the fit to the Compton edge unreliable. Still, to give some understanding as to possible non-linearities in the scintillator gain, Figure 4.24 is a plot of a fit to the Compton edges of the lower-energy γs as well as this ^{241}Am/Be source. The solid line represents a linear fit through all the points while the dashed line is a fit with the non-linear calibration given in the figure. The difference between the two types of calibration is seen to be less than $\pm$25 keV which should be a conservative upper limit considering the poor fit to the ^{241}Am/Be source. Clearly, it would be desirable to add points between the ^{88}Y (1.9 MeV) and ^{241}Am/Be Compton edges to better determine the linearity between 2–4 MeV.

Returning now to the results of Table 4.6, the resolution was fit to the $\sigma_{\rm scin}$ of the 2$^{\rm nd}$ iteration with the results given in Figure 4.25(a). The ^{38}K and ^{241}Am/Be Compton edges are plotted, but not included in the fit (the ^{241}Am/Be was taken from

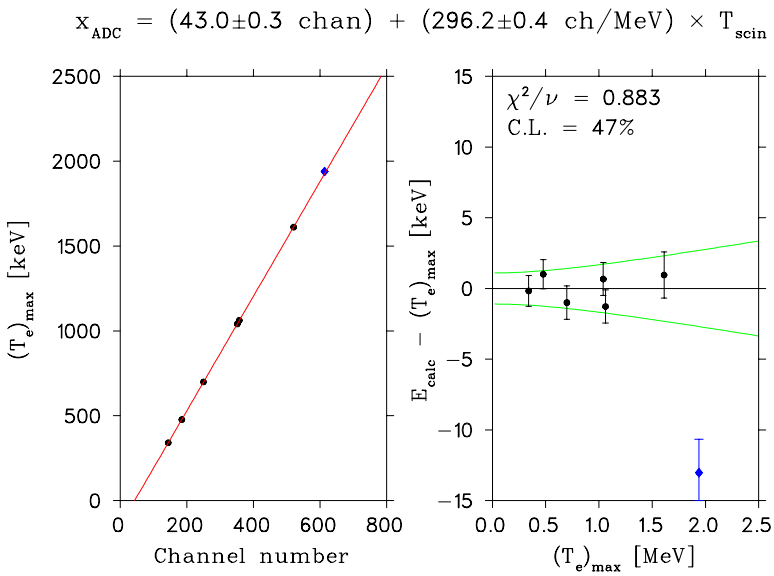

FIGURE 4.23: Calibration of May 2nd, 1999 using the Compton edges of the γ sources listed in Table 4.6 (left) and the residuals of the fit (right). The additional point at 1.94 MeV is the ^{38}K ground state, but this was fit with a large ^{38m}K β 'background' and subject to systematic errors; this point was therefore not included in the fit. The solid lines in the residual plot represent the uncertainty in the calibration.

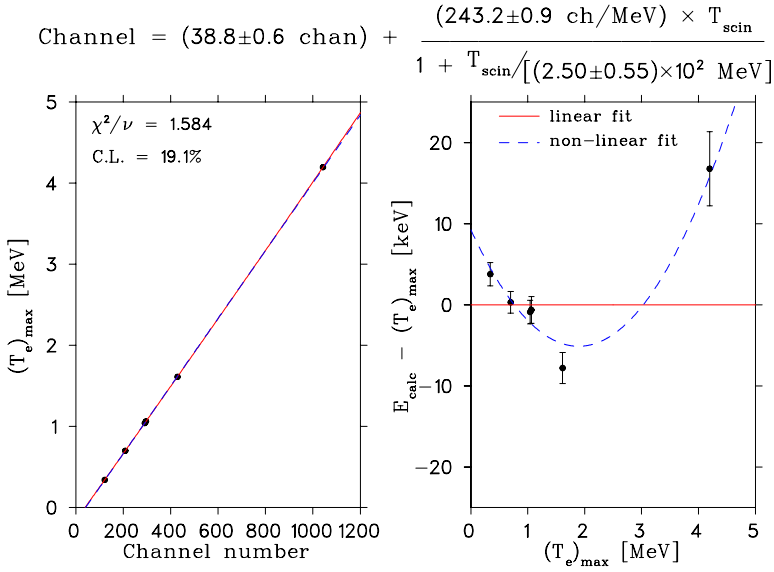

FIGURE 4.24: Non-linear fit to the scintillator's calibration using the Compton edges of γ sources. These calibration points and those of Figure 4.23 were taken at different times.

Figure 4.25(b); see below). Additionally, the result quoted by Clifford, et. al [43] is included for comparison; as indicated by the design simulations, it was hoped that TRINAT's scintillator would have a resolution comparable to Clifford's, and it can be seen that this has been accomplished. At least over the range of the γ sources, the resolution follows the square-root law expected if photon statistics dominate uncertainties in the scintillator's energy measurement. The fits actually tended towards a negative offset, i.e. $\sigma_{\text{scin}} \sim \sqrt{\mu \times T_{\text{scin}}} - \sigma_\circ$; as this is unphysical, the fit was forced to $\sigma_\circ = 0$ if it converged to negative values. The width of the Compton edge at lower energies is more dependent on multiple scattering effects as the γ cross section is increasing; this complicates deriving the resolution for ^{137}Cs and the annihilation radiation from ^{22}Na, and tends to overestimate the σ_{scin} of these points. When $\sigma_\circ \equiv 0$, the fit value of μ will increase in compensation, so that the resolution given in the figure is not *under*estimated, though it may in fact be *over*estimated.

Figure 4.25(b) is a fit to the same γ sources (except ^{137}Cs was not included) when the spectra were taken off-line in an environment where scattering off nearby volumes was minimized. The fits to these spectra provided cleaner spectra that could be fit further below the Compton edge than those taken when the scintillator was mounted in the detection chamber. The dashed line of this figure represents the fit if the ^{241}Am/Be edge was not included; the solid one, whose results are the ones quoted, is if this higher energy point is included. The result, which is in agreement with that of the April 1999 fit, is only slightly affected by the ^{241}Am/Be point due to the relatively large uncertainty in its value. The resolution of the scintillator is therefore taken to be $\sigma_{\text{scin}} = \sqrt{(1.80 \text{ keV}) \times T_{\text{scin}}}$. It is this resolution function that is used in subsequent MC simulations.

4.3.4 Stabilization

As mentioned earlier, the gain of the PMT is stabilized to correct for long-term drifts, changes in count rates, and temperature variations. The system is schematically depicted in the lower left part of the electronics diagram (page 128); further details about the 'stabilization unit' can be found in reference [62].

A blue LED is rigidly coupled to the light guide of the scintillator just outside the

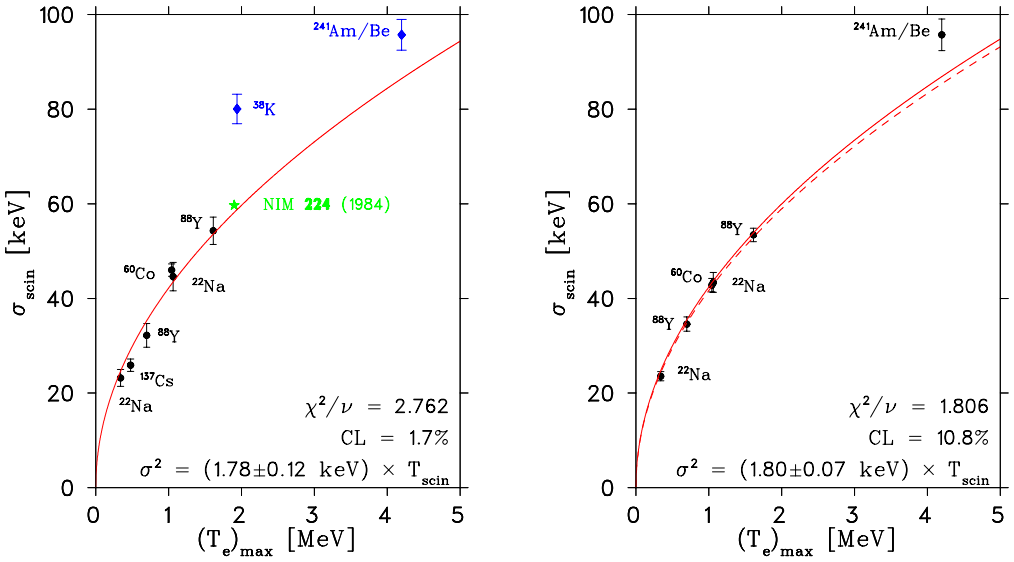

(a) April 1999 (b) November 1998

FIGURE 4.25: Resolution of the scintillator as determined by fits to Compton edges. The ^{38}K and ^{241}Am/Be points are not included in (a) because their Compton edges are on top of a large background (βs and neutrons respectively). The result quoted in (b) includes the ^{241}Am/Be point (solid line) and does not change the result much from just using the lower-energy γs (dashed line in (b) and result given in (a)).

vacuum system as well as to a photodiode (PD) via a fibre-optic cable. The intensity of the LED is locked by the stabilization unit which adjusts the power driving the LED such that the signal in the PD is maintained constant. The temperature dependence of the PD's gain was measured to be $-0.1\%/°C$, so large temperature changes would not be properly corrected for. Although TRINAT uses a temperature stabilized clean room ($\pm 0.5°C$ to help keep temperature drifts in the Ti:sapphire laser intensity from extending beyond the feedback loop's range), we decided to house the PD in a casing stabilized with Peltier coolers to ± 50 mK. Thus the LED light output is constant at the 1×10^{-4} level.

The gain of the scintillator is monitored by the unit and stabilized by locking the LED pulse height in the PMT; this is done by adjusting the (nominally -1850 V) high voltage applied to it. The 450 nm wavelength LED was specially chosen (versus more

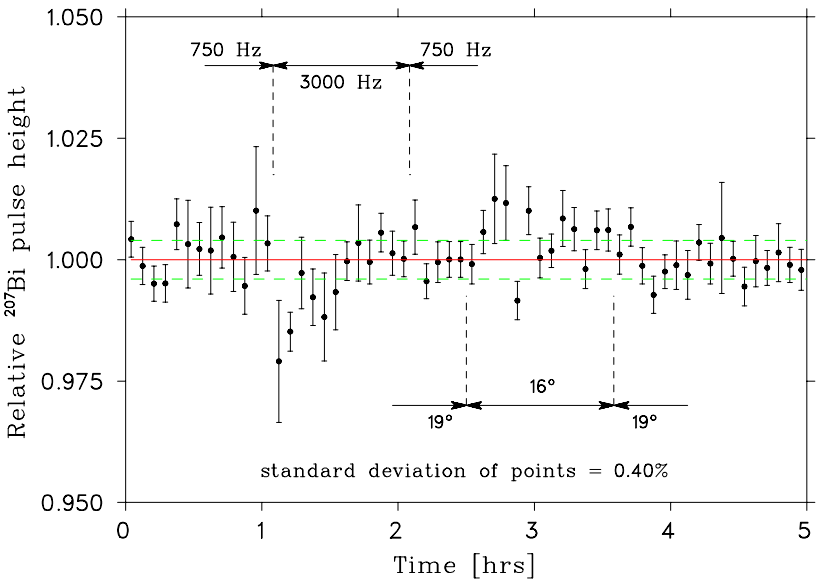

FIGURE 4.26: Stabilization test of the scintillator's gain. Plotted is the peak position of a ^{207}Bi source in the scintillator over the course of hours. The system can be seen to keep the gain of the PMT constant even when subject to large count rate changes and temperature variations.

readily available green LEDs) to closely match the spectrum of the BC408 scintillation light as well as to overlap the peak of the photocathode response (both 425 nm). This is important to ensure that the spectral sensitivity of the photocathode to the LED and scintillation light be as closely matched as possible. Also, since the temperature dependence of the photocathode's quantum efficiency is a function of the incident photon's frequency, good overlap ensures that temperature variations are properly corrected.

Tests of the stability were made using the electron conversion peak in ^{207}Bi. The scintillator, unlike the silicon detector used to test for energy straggling, does not resolve the two lines; the spectrum has just one peak at roughly 1 MeV. The ^{207}Bi decay also has a few γ lines, but a coincidence condition with the DSSSD removes this background; the full absorption peak of the mono-energetic positrons is a nearly Gaussian distribution, which is a good monitor of the PMT gain. The results of one of the stabilization tests, when the detector was subjected to large changes in the count rate as well as the ambient temperature, is given in Figure 4.26. The rates were

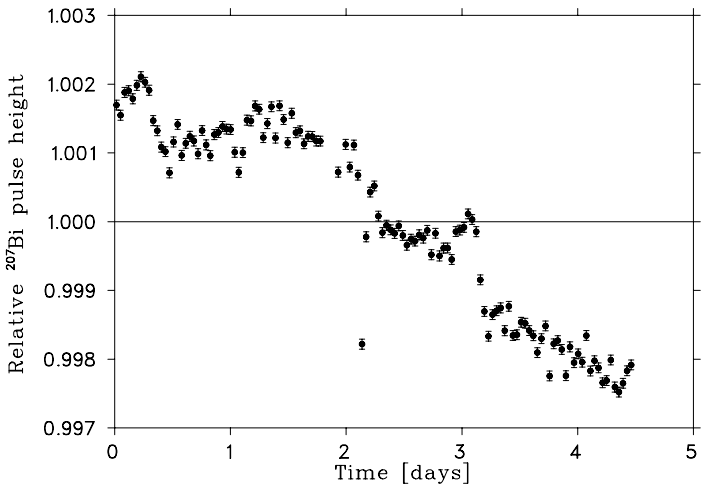

FIGURE 4.27: Long term test of the scintillator stabilization system. The count rate was a constant 750 Hz and temperature variations are less than 0.5°.

changed by introducing γ sources (^{137}Cs and ^{60}Co) which do not contaminate the electron conversion peak again because of the DSSSD coincidence. In the experiment the count rates only vary from $100 - 500$ Hz, predominantly due to changes in the amount of ^{38}K background. The test demonstrates that, after an initial jump, the stabilization system adequately corrects the PMT's gain when subject to count rate changes $5\times$ larger than we see in the experiment.

The temperature dependence of the system was investigated by adjusting the ambient temperature of the TRINAT laboratory by 3°, which again is much larger than experienced during the correlation experiment. As it did when the count rate was tested, the stabilization system recovers shortly after an initial jump, and correctly locks the gain.

The overall stability of the gain including large count rate and temperature changes is 0.4%. With only small, long-term drifts in the temperature and a constant count rate of 700 Hz, the long term stability was tested over a period of four days with the results given in Figure 4.27. Though the gain shows a definite drift of approximately -0.4%, the short term variations in this case are seen to be as low as 0.05%. The Compton calibration has an uncertainty of 0.14% (extrapolated to 5 MeV) so the stabilization unit corrects the gain well enough considering how well we can measure the energy.

Approximately every three days during the April/May 1999 run, calibrations using ^{88}Y, ^{22}Na and ^{60}Co were made so as to monitor the long term drift of the scintillator gain. The differences in these calibrations are only about as large as the uncertainties in the fits themselves, and so the system is stable to within our ability to measure it this way. Increased sensitivity to long-term drifts might be obtained by comparing the scintillator's on-line β spectrum as a function of time. Indeed, as we will see in the next section, the final calibration of the scintillator is taken from fitting the β spectrum of the entire data set. By doing this, we become less sensitive to the long-term drifts because in this case, the calibration is fit to the gain *averaged* over the entire running period.

4.3.5 ^{38m}K Results and an Extended Calibration

The on-line spectrum of the scintillator on its own, despite the 75 cm collection–detection trap separation and the lead shielding (both of which help greatly), is still dominated by the ^{38}K background. The γ-β ratio in the pre-scaled scintillator spectrum was measured to be 45:1 by simultaneously fitting the Compton edge of the 2.2 MeV γ and the ^{38m}K β spectrum to GEANT simulations of the two. The hardware DSSSD coincidence greatly reduces the ground state background by a factor of 35, but the γ events cannot be *totally* removed this way because they do in fact have a non-negligible probability of firing both detectors in the telescope. The most likely mechanism for these γ coincidences is when the photon Compton scatters in the DSSSD and the collisional partner, the electron, is detected in the nearby scintillator; both detectors in this case register an event which is thus indiscernible from a (good) β event.

Here and throughout the rest of this section, the scintillator spectra presented require a coincident DSSSD event that passed the analysis scheme outlined in §4.2.5. This condition, which can also be imposed in simulations, is used because it provides a cleaner β spectrum by reducing the ^{38}K background; however, the 2.2 MeV γs *do* fire both detectors and so will still need to be included in the analysis as a background.

The shape of the on-line β spectrum, particularly the low-energy part of it, was found to have a strong dependence on the conditions imposed by the DSSSD anal-

ysis scheme. In order to get 95% of the events in the resolution functions of the strips, a $\sigma_{\rm cut} = 3$ energy acceptance should be chosen (see Equation 4.5 on page 59). By definition, the variation of the energy reading in the ΔE increases with the $\Delta E_{\rm DSSSD} \leq 3\sigma_{\rm DSSSD}$ acceptance, and the suppression of background events will be less efficient; note also, however, that it tends to accept more higher-energy DSSSD events ($\gtrsim 500$ keV) since these events are the ones which suffer most from inconsistencies between the strip calibrations (see for example Figure 4.13). More precisely, a tight cut of $1\sigma_{\rm DSSSD}$ will *exclude* (good[†]) higher-energy DSSSD events whereas the larger acceptance *retains* them. The plots in the top of Figure 4.28 show the Kurie plots[‡] for the different DSSSD energy agreement conditions of $1\sigma_{\rm DSSSD}$, $2\sigma_{\rm DSSSD}$ and $3\sigma_{\rm DSSSD}$. The tightest condition, $\Delta E_{\rm DSSSD} \leq 1\sigma_{\rm DSSSD}$, accounts for 68% of the $3\sigma_{\rm DSSSD}$ overall acceptance; the $(1-2)\sigma_{\rm DSSSD}$ and $(2-3)\sigma_{\rm DSSSD}$ events contain the additional 26% and 6% respectively. In order to compare the spectrum shapes (bottom of the figure), the spectra have been renormalized so that they all have the same total number of counts and then the difference from the average was taken. The spectrum shape of the $2\sigma_{\rm DSSSD}$ events is not dramatically different from the tight $1\sigma_{\rm DSSSD}$ cut, but does have slightly more events at lower β energy. The $3\sigma_{\rm DSSSD}$ events have a very different shape which is expected, whether the low-energy events correspond to high-energy DSSSD events or to a background; §4.4.1 discusses the total $(E + \Delta E)$ β energy reading which discriminates between these two cases. As statistics is not a concern in the β spectra from the April/May 1999 run, a DSSSD energy agreement condition of $1\sigma_{\rm DSSSD}$ is used throughout this thesis unless otherwise noted.

GEANT simulations of the ^{38m}K decay were programmed [63] to generate the initial positrons (as well as the recoils) from the trap* according to the decay rate, Equation (2.24); the Standard Model values of the $C_S = C_S' = 0$ and $C_V = C_V' = 1$ are (always) assumed. The βs are emitted isotropically into 4π and tracked until they either annihilate or exit the detection chamber. Any generated secondaries are also fully tracked to ensure the simulation properly accounts for coincidences where the

[†]'Good' in that it was an $e^{\pm}$ which fired the DSSSD; it will be 'bad' in that we will have a large uncertainty in the overall energy.

[‡]The response function is not accounted for in Figure 4.28 so as to show its effects.

*The finite size of the trap, as measured by CCD cameras, is incorporated in [63].

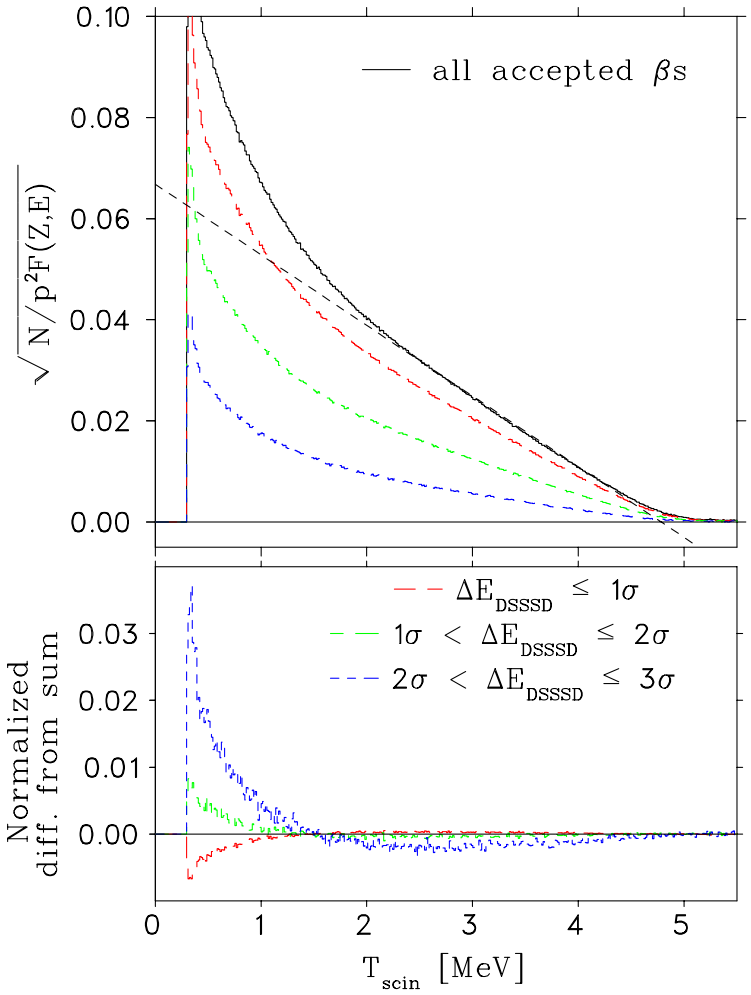

FIGURE 4.28: Scintillator Kurie plots for different DSSSD x- and y-strip energy agreement conditions. The Kurie plot with $\Delta E_{\mathrm{DSSSD}} \leq 3\sigma_{\mathrm{DSSSD}}$ follows a straight line above the 2.2 MeV γ background; the events above the end point (nominally 4.75 MeV, which is below the Q-value because of the energy lost in the Be foil, DSSSD and Teflon) are from Compton summing of the annihilation radiation. A DSSSD energy agreement condition set between $(2-3)\sigma_{\mathrm{DSSSD}}$ does not contribute many events compared to the rest (top), but have a much larger low-energy tail (bottom; renormalized).

scintillator and/or DSSSD *only* fires as a result of the annihilation radiation or a δ ray that goes from one into the other. The scintillator and DSSSD singles spectra are incremented by the total energy deposited in them by either the primary positron or any generated secondary. If the simulated energies deposited in the detectors both pass their respective thresholds, as defined by those used in the experimental data analysis, then the telescope's singles (i.e. the $T_\beta = T_{\rm scin} + E_{\rm DSSSD}$ coincidence) spectrum is also incremented.

Simulations of the ^{38}K decay were made in an attempt to generate the shape of the γ background. The MC generates the 2.2 MeV photons at the collection trap since this is where most of the ground state's activity is concentrated. In order to speed up the simulations, the γs are not emitted isotropically, but are initially directed towards the β-telescope in a cone that covers the area exposed by the 15.24 cm diameter detection chamber. The Monte Carlo does not contain any volumes outside the detection chamber, but it is important to start the γs from the first trap because they can (predominantly forward) scatter in the chamber wall and this probability will depend on the initial direction of the γ. The lead shielding is not included because the CPU requirements would be exorbitant; this will certainly affect the simulated ^{38}K spectrum shape because the γs that (forward) Compton scatter in the lead (and *then* detected in the telescope) will appear as a source of γs that are distributed with energies less than the original 2.2 MeV.

The Kurie plots of the scintillator's on-line β spectrum in Figure 4.28 can be seen to be linear above about 2.2 MeV. The deviations are predominantly due to the ^{38}K background, but effects from the response function of the scintillator must also be included. The response function effects are most clearly visible as the high energy tail near and above the end point, and by the large number of events just above threshold; the former is from Compton summing of the annihilation radiation while the latter arises from events where the positron was stopped in the DSSSD and one of the annihilation quanta Compton scattered in the plastic. Both of these effects are reproduced in GEANT as can be seen in Figure 4.29; this is a fit of the data to MC simulations of the ^{38m}K β spectrum and the ground state's (coincident) γ background. The Compton edge at 340 keV corresponds to the 511 keV annihilation quanta and has in fact allowed us to keep the offset and the slope of the energy calibration

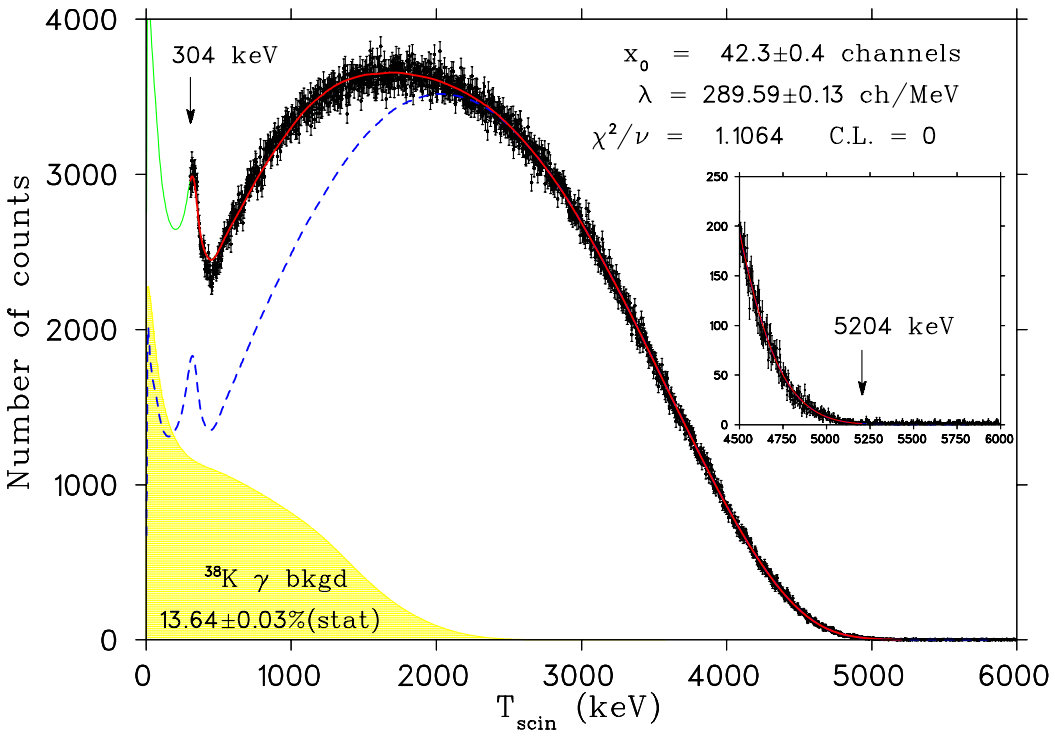

FIGURE 4.29: Fit of the ^{38m}K spectrum to a Monte Carlo simulation that includes the 2.2 MeV background. This spectrum represents the energy deposited in the scintillator (only) detected in coincidence with an event in the DSSSD. The dashed line represents a simulation of the β spectrum and the filled curve is the ^{38}K ground state background. The solid line is the sum of these two simulations over the fitting range (304 – 5204 keV, over the entire spectrum).

both free to vary in the fit because we have two distinct points in the data: this Compton edge and the known Q-value of 5.022 MeV. Note that the β spectrum only appears to extend all the way out to the Q-value because of Compton summing of the annihilation radiation; the bulk of the missing energy is deposited in the DSSSD and will be retrieved in the telescope's total energy reading. Approximately 25 and 40 keV are lost in the β window and the Teflon wrapping respectively; however, these small dead layers are included in GEANT and so this energy loss should be accounted for in the simulations.

In addition to the slope and offset of the energy calibration, the relative normalization of the ^{38}K and ^{38m}K Monte Carlos and the resolution of the γ spectrum were also free to vary in the fit. The resolution of the β spectrum was fixed as the function

obtained from the Compton edge analysis (Figure 4.25). The same could not be done for the γ spectrum because the Compton edge ends up being much too sharp. As mentioned earlier, the lead shielding (and other additional scattering volumes) will cause the ^{38}K background not to be the result of only 2.2 MeV photons, but a distribution of γ energies; this will smooth out the Compton edge at $E_{\rm scin} = 1.94$ MeV. The resolution of the background was therefore free to grow as large as necessary to get essentially the same effect and indeed it tended towards much larger resolutions (typically $\sigma_{\rm scin}^{^{38}{\rm K}} \approx \sqrt{25 E_{\rm keV}}$). This method of smoothing the simulated ^{38}K spectrum to account for the lack of scattering volumes included in GEANT's geometry allows the fit to be extended all the way down to threshold, approximately 300 keV as indicated in the figure (also, see below). The smoothed background is not a perfect approximation to the true ground state background as is immediately evident by the fact that it extends above 2.2 MeV, the total energy of the initial photon. The calculated 14% contamination from the ground state represents an additional 9.4× suppression from the DSSSD analysis scheme (using a $\Delta E_{\rm DSSSD} \leq 1\sigma_{\rm DSSSD}$ acceptance) on top of the 35× suppression from the hardware scintillator-DSSSD coincidence. This calculation of the amount of ^{38}K background present in the β spectrum can only be considered approximate, however, because the fitting of the relative normalization is based on the *total* integral number of counts in the two MCs. This will depend on the shape of the spectrum and, since it changes rapidly below about 250 keV, is subject to systematics which far outweigh the statistical uncertainty quoted.

The imperfect understanding of the γ background is the source of most[†] of the discrepancy between the data and the fit, most notably in the 'valley' at about 450 keV. This compromises the effectiveness of the 511 Compton edge in reducing correlations between the fit parameters (in particular $x_\circ$ and λ of the scintillator calibration). The fit of the edge's position in channel number is still good, however, because the γ spectrum is smooth and does not change very much over the limited range of the 511 Compton edge itself. It would be very useful to obtain an experimental shape for this ^{38}K background because it would allow more precise calibrations down to lower energies and provide an overall better understanding below 2.2 MeV. Attempts were

[†]Another possibility is an underestimation of the low-energy tail by GEANT, but this will be shown to be small by the results of §4.5.2.

Channel	Energy [keV]	$x_\circ$ [channels]	λ [ch/MeV]	χ^2/ν
128	285	45.59	288.76	2.256
129	292	44.46	289.05	1.869
130	299	43.41	289.31	1.515
131	306	42.32	289.59	1.106
132	309	42.27	289.60	1.106
133	313	42.29	289.60	1.107
134	316	42.27	289.60	1.107

TABLE 4.7: Map of the χ^2/ν as a function of the low-energy cut-off of the fitting region. The threshold determined from the γ sources of 131 channels is consistent with this map. The high-energy limit of the fit was fixed at channel 1550.

made to get the shape from events when the ^{38m}K was not trapped, but with only a 7.6 min half-life of the ground state, they did not provide nearly enough statistics in the scintillator-DSSSD coincidence spectrum. A dedicated period of the next run should be directed towards measuring this background, simply by not trapping the ^{38m}K but still having ISAC provide us with the potassium beam.

In fitting the on-line β spectrum, the χ^2 was found to depend on the fitting region used, particularly with the low-energy cutoff. This is not surprisingly because the low-energy part of the spectrum is where the greatest contribution to the χ^2 comes from. In order to have an unbiased estimate of the true energy threshold of the scintillator[†], the threshold was determined from spectra of γ sources (^{88}Y, ^{60}Co and ^{137}Cs) which do not contain a 511 Compton edge. These spectra showed that the threshold does not affect the scintillator's spectrum above channel 131. As a check, the χ^2 per degree of freedom (ν) was mapped as a function of the low-energy cut-off with the results given in Table 4.7. The χ^2/ν as well as the fit parameters can be seen to change dramatically below channel 131, but are all more or less constant above it and so this map is consistent with the threshold value found in the γ sources. The threshold is therefore always taken to be at channel 131 in the scintillator spectrum; for the calibration of Figure 4.29, this corresponds to 306 keV.

[†]It is difficult to differentiate between the fast fall immediately below the 511 Compton edge and that caused by the threshold.

The dependence on the high-energy cut-off is less sensitive; fits where the upper limit of the fitting region was varied between 4.94 and 5.46 MeV showed that the χ^2/ν remained essentially constant: it only changed by +1.8% at 4.94 MeV, but by +11.1% at 5.46 MeV. Note that a small background subtraction, not included in the present analysis, would reduce the dependence above the end point; the MC has virtually no counts above 5.3 MeV, so the χ^2/ν naturally rises due this high-energy tail (which probably is a result of the cosmic ray background). The fit values for $x_\circ$ and λ (i.e. the calibration) changed only by a negligible amount, $^{+0.07}_{-0.5}\%$ and $^{+0.04}_{-0.01}\%$ respectively. These differences are within the fit parameter uncertainties, so the fit of the β spectrum is independent of the high-energy cut-off. The counts in the data are predominantly background above channel 1550 ($\approx$ 5.2 MeV) and so this value is chosen for the β fits which follow.

The calibration fit in Figure 4.29 is rather different from that obtained using the γ sources (see Figure 4.23 on page 75). The channel numbers corresponding to 5 MeV differ by 2.2%, which is well outside the difference allowed from the calibration uncertainties. This effect may be a result of inefficient light collection from where the βs generate scintillation light compared to the whole; since the γs Compton scatter homogeneously throughout the plastic, they average over the bulk of the plastic while the βs are concentrated more near the front face of it. Another possibility is the inaccuracy of GEANT's ability to properly simulate (*i*) annihilation-in-flight, (*ii*) the differences in the radiative energy losses of e^+ to that of a Compton scattered e^-, and/or (*iii*) the relative cross-sections for radiative and collisional energy losses of positrons. Differences in calibrations from γ and positron sources has been noted by others [64], but a full explanation has still not been found. Since the β spectrum fit is to the data themselves and it averages over variations throughout the running period, this calibration is preferentially used instead of the Compton calibration. The resolution, however, remains defined by the fits to the Compton edges.

For the $\beta - \nu$ correlation experiment, the additional coincidence condition with the recoil detector virtually eliminates the ^{38}K γ background and indeed, may one day be used as a test of the lower β energy part of GEANT's simulations. At present though, other uncertainties preclude doing this (see §4.5.2), and so the measurement on a will be sensitive to how different the β-telescope's response function is from

GEANT simulations. The present analysis scheme does not, however, use events below $T_\beta = 2.5$ MeV; thus the fit of the scintillator's β spectrum that is relevant to the experiment does not include the ground state background. Without fitting the 511 Compton edge, the offset of the calibration cannot be fit, so we fix it to the result obtained from the β fit of Figure 4.29, namely $x_\circ \equiv 42.3$ channels. With now only the slope, λ, of the calibration free to vary, Figure 4.30 shows the result of a fit where the low-energy limit of the fitting range was 2.2 MeV. Over this more limited range, the GEANT simulation of the β spectrum is excellent, with a confidence level of over 80%. This means that for the correlation experiment, GEANT does a very good job of reproducing the β spectrum over the region of interest. A potential source of concern would be a difference in the value of λ fit here with that of Figure 4.29, however the difference of 0.05 ch/MeV is well within both of their uncertainties. The two calibrations agree, and this result is important because it shows that the γ background and, to a lesser extent, the DSSSD–GEANT discrepancy, does not bias the scintillator's calibration obtained in fitting the β spectrum. The GEANT simulation of the ground state smoothed with a resolution much worse than measured, is in this case an adequate approximation because fitting above it does not change the best-fit calibration. Therefore, the calibration of Figure 4.29:

$$T_{\rm scin}(x_{\rm ADC}) = (3.4531 \pm 0.0014 \text{ keV/chan}) \times x_{\rm ADC} \; - \; (146.1 \pm 1.5 \text{ keV}) \qquad (4.17)$$

can be considered reliable and should be used in any analysis of the April/May 1999 data set that requires the βs energy. The differences from the observed DSSSD energy spectrum and that of GEANT's may also affect this fit because this energy is subtracted in both the MC and the data; the calibration may therefore be biased, but only slightly since the discrepancy is very small compared to the energy deposited in the scintillator. This effect is addressed later in §4.4.1.

4.4 The β-telescope

Whereas earlier sections dealt with the E and ΔE detectors separately, this section deals with the results from the April/May 1999 run of the β-telescope as a whole. First, the telescope (meaning the $T_{\rm scin} + E_{\rm DSSSD} = T_\beta$) β spectra are presented and

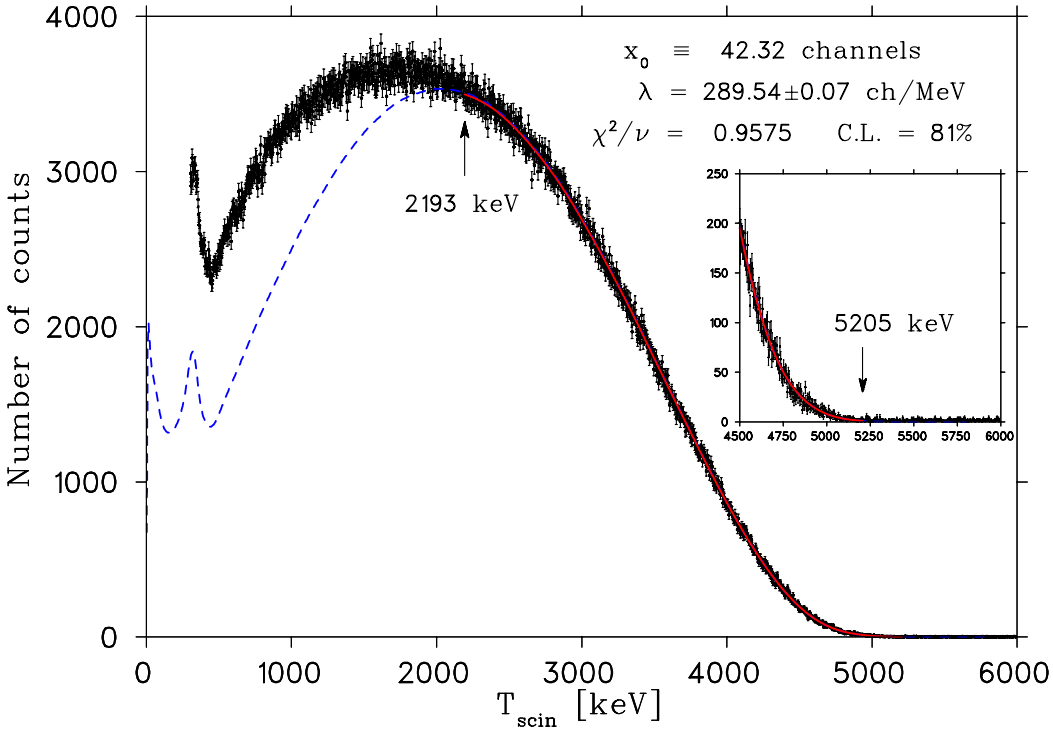

FIGURE 4.30: Fit of the ^{38m}K spectrum above 2.2 MeV to a Monte Carlo simulation. The fitting region (2193 – 5205 keV) is above the ^{38}K background contamination, and so the MC in this case is only of the β spectrum. The offset of the calibration is fixed at $x_\circ \equiv 42.3$ from Figure 4.29 because the 511 Compton edge is not fit.

discussed. Following this is §4.4.2 which compares backscatter calculations of GEANT to those on-line using the DSSSD position information. The uniformity of the telescope response to the incident positron's direction is discussed in §4.4.3. The final section explains how the β-telescope may be used to measure b_e, the Fierz interference parameter.

4.4.1 Total β Energy

The previous two sections have provided us with both the calibration and the resolution of the scintillator and all of the forty-eight DSSSD strips, as well as an effective position decoding analysis scheme. The calibrations allow us to sum up the scintillator and DSSSD energy readings for a total T_β measurement[†]. Having an understanding of these detector resolutions further allows us to program GEANT to simulate the telescope's β spectrum of the ^{38m}K decay; the resolutions are essential because they must be applied *before* adding the two energies (as is the case with the real data) rather than fitting them after. Prior to fitting or comparing the on-line spectra to these MCs, considerable effort must be made to ensure that all conditions placed on the on-line data are reflected in the simulation. As a quick list, the most important parameters to consider are:

- The detectors' resolutions and calibrations (fixed).
- The scintillator's low-energy threshold (user parameter).
- The DSSSD low- *and* high-energy thresholds (user parameters).
- The active area of the DSSSD (user's choice; for example, whether or not the edge strips are included).

We saw earlier in Figure 4.28 how the value of σ_{cut} used in the analysis of the on-line data has an impact on the resulting β-telescope's spectra. The corresponding figure for the total energy, $T_\beta = T_{\text{scin}} + E_{\text{DSSSD}}$, is given in Figure 4.31. A qualitative comparison of these two figures tells us that the additional low-energy events in the

[†]In fact, this coupled with the position information gives us a measurement of the positron's *momentum*, $\boldsymbol{p}_e$.

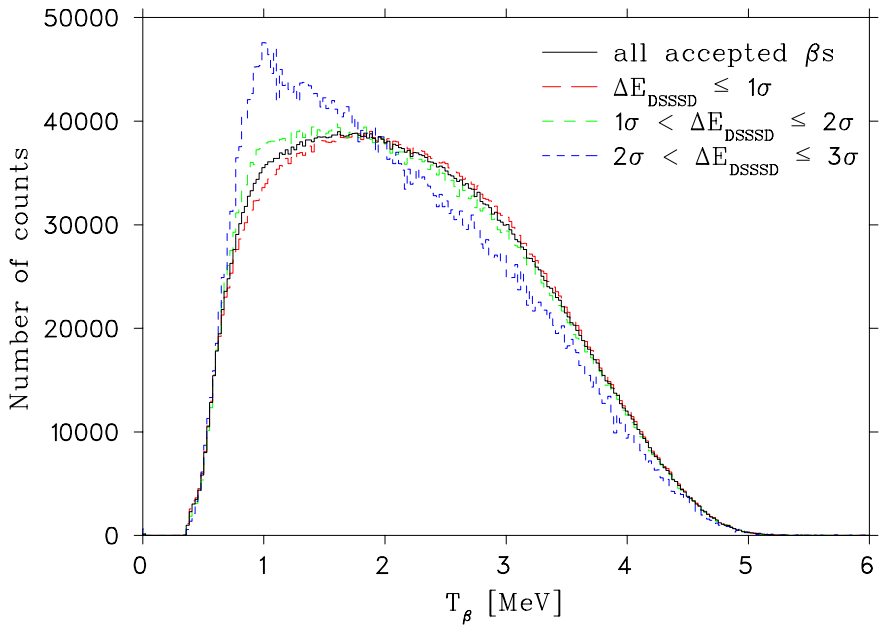

FIGURE 4.31: The telescope's β spectra for different $\Delta E_{\mathrm{DSSSD}}$ conditions. These are the corresponding spectra for Figure 4.28; they have the same conditions applied and only differ in that the DSSSD energy has been added to the scintillator's.

larger $\Delta E_{\mathrm{DSSSD}}$ spectra are *not* due to the greater acceptance of high-energy DSSSD events (as suggested they may be in §4.3.5) because adding back the DSSSD energy does not remove this low-energy tail. With just a little imagination, one can see the Compton edge of the 2.2 MeV background in the $3\sigma_{\mathrm{DSSSD}}$ β spectrum, indicating that the larger acceptance instead allows a greater contamination from this, and presumably other, backgrounds. Thus unless statistics is a great concern[†], the tighter $\Delta E_{\mathrm{DSSSD}}$ energy cut of $\lesssim 1\sigma_{\mathrm{DSSSD}}$ should definitely be used.

The Compton edge at 340 keV, prominent in the scintillator's energy spectrum, no longer appears once the DSSSD energy has been added back in. If the peak remained, it would indicate that these events fired just above the DSSSD's threshold, and they would likely be due to a random fluctuation above threshold, randomly coincident low-energy photons, or they might point to a flaw in the analysis scheme. The fact that the edge does not remain in the telescope's β spectrum shows that an appreciable amount of energy was deposited in the DSSSD; this is consistent with a

[†]Which may be the case once the recoil coincidence is applied, for example.

positron scattering or stopping in the strip detector, and then one of the annihilation quanta Compton scattering in the scintillator. The total energy of these events are distributed above the Compton edge in the β spectrum, so the telescope *will* contain some background from these events, but these events are (*i*) impossible to remove by a re-design of the telescope, (*ii*) a small percentage of the total number of events, and (*iii*) reproduced reasonably well by GEANT for the scintillator's spectrum as shown in Figure 4.29. They can be greatly suppressed, however, simply by setting the scintillator's (software) threshold at or above 400 keV in the analyzing program.

Although it is good that these events do not remain a well-defined Compton edge in the telescope's spectrum, it also perhaps a *little* unfortunate because we no longer have two distinct points to fit to as before. As was the case when fitting above the 2.2 MeV background, we must fix the offset of the energy calibration. For the telescope, this 'energy calibration' will be different from the scintillator or DSSSD's in that it is *already* calibrated, and therefore in units of energy rather than channels. If we were to fit the MC to the telescope's β spectrum and if everything was perfectly calibrated and simulated, the telescope's calibration:

$$T_\beta = T_\beta^\circ + \eta\,(T_{\rm scin} + E_{\rm DSSSD}) \tag{4.18}$$

would yield an offset of $T_\beta^\circ = 0$ keV and $\eta = 1$ keV/keV for the slope. The poor agreement between the DSSSD's energy spectrum and that simulated by GEANT is an immediate indication that this is not the case. To first order, however, the difference between the DSSSD and GEANT's energy distributions is given by the difference of their mean values, which is -10.3 keV (see Figure 4.18). We therefore can account for the ΔE's discrepancy *on average* by fixing the offset to be $+10.3$ keV.

The β spectrum from the on-line data and the results of a fit to a MC simulation is given in Figure 4.32. As mentioned earlier, the resolution of the detectors must be input into the MC before adding the detectors' energies up, and therefore the resolution cannot be fit. The free parameters in this fit are just the slope of the calibration and the relative normalization of the β and 2.2 MeV γ background. The simulation of the ground state, which is convoluted with the same resolution as in Figure 4.29, is not as good an approximation anymore as the Compton edge is clearly visible at 1.9 MeV. The unreasonably large resolution of the ground state in fact

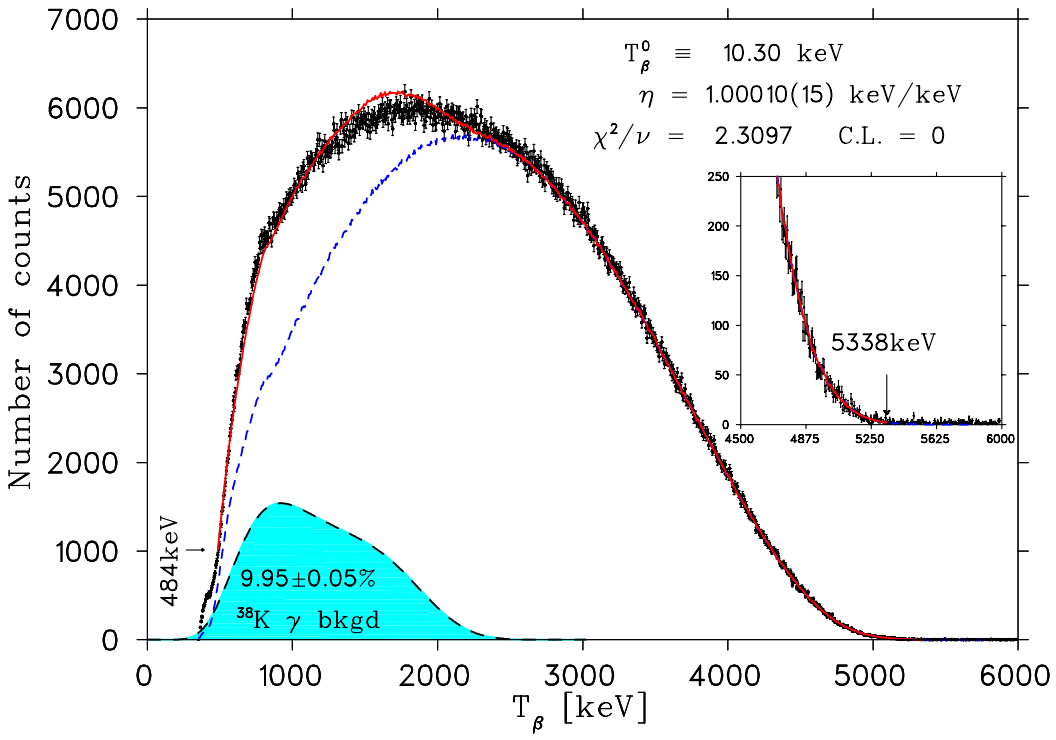

FIGURE 4.32: Fit of the ^{38m}K T_β spectrum to a Monte Carlo simulation. The offset was fixed at 10.3 keV because of the average difference between the GEANT simulated and measured DSSSD energy spectra. The ^{38}K background is not reproduced as well when the DSSSD energy is added back in.

can be seen to limit our low-energy fitting range because it unphysically places events below the scintillator's threshold, resulting in a low-energy tail. One point that should be noted is that the resolution of the ^{38}K background *in the DSSSD* was not adjusted since we have no idea what the DSSSD's spectrum is in this case. Indeed, simulations indicate a higher average energy loss than the ^{38m}K βs, and since there already is a DSSSD–GEANT discrepancy, the DSSSD's ^{38}K spectrum can play a more important role. Perhaps most significant, however, is the fact that in this case the background shape in both detectors must be fixed when fitting the β spectrum, rather than open to approximating over-estimations of the resolution. It is not too surprising, then, that this total β energy spectrum is not reproduced as well. Once again, an experimentally measured spectrum shape for the ground state is essential for a good understanding below 2 MeV.

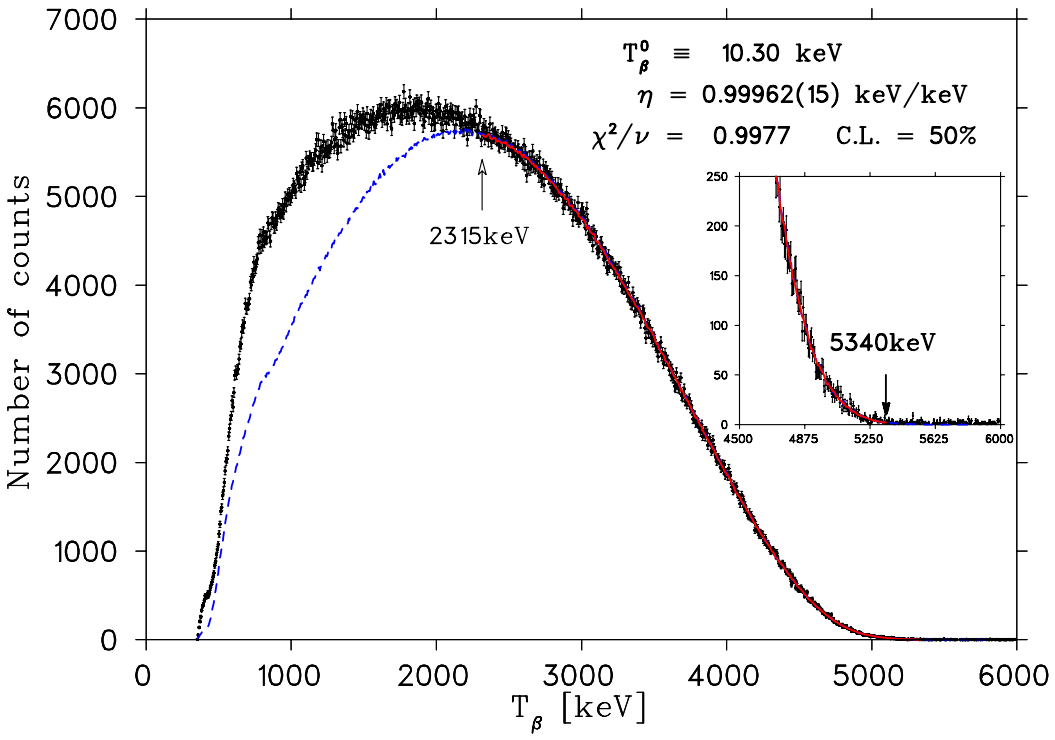

FIGURE 4.33: Fit of the ^{38m}K T_β spectrum above 2.3 MeV to a Monte Carlo simulation. Above the ^{38}K background, the MC is seen to reproduce the on-line ^{38m}K β spectrum very well.

The fit to the data naturally has a large χ^2/ν due to the ground state background, but otherwise the fit looks very good. The fit to the re-calibrated slope is unity within uncertainties which is encouraging. As with the scintillator's spectrum, we also fit above this ground state to see how that affects the calibration. The result is plotted in Figure 4.33 and again we find that the MC does an excellent job of reproducing the data. The fits were sensitive to the low-energy cut of the fitting region, and needed to be placed slightly higher than expected ($\leq$ 2.2 MeV) in order to obtain good agreement. The value of η is one to within 0.06%, which is a clear indication that the DSSSD–GEANT discrepancy is negligible once the average difference is accounted for ($T_\beta^\circ = 10.3$ keV).

4.4.2 Backscattering Losses

As discussed earlier, one of the reasons TRINAT decided to switch to a plastic scintillator instead of the Si(Li) as the E detector was to reduce backscattering losses. The low-Z plastic has a relatively low probability for backscattering and the simulations of Figure 4.2 indicate that our losses are dominated by backscattering off the DSSSD; this represents an overall loss of event acceptance and *can* affect the β spectrum if an annihilation photon then Compton scatters in the scintillator, as discussed in the previous section.

There is also another type of backscattering loss to consider, and one that can be measured and then compared to GEANT as a check of how well it is reproduced in the simulations. Consider events where the β first goes through the DSSSD, then scatters in the scintillator, and eventually scatters back out through the DSSSD again. These events (hereafter called 'backscattered events') *will* add to the low-energy tail of the telescope's response function because energy is deposited in both the E and ΔE detectors. The pixel of the DSSSD that the positron enters through will, in general, differ from the one that it backscatters out through; in this case, the event is flagged as a double hit and vetoed by the analysis of the DSSSD position information. We assume that these double hits in the DSSSD, where both ($\hat{x}$ and $\hat{y}$) group hits passed the position and energy cuts ($\sigma_{\rm cut} = 1$) of the DSSSD analysis scheme, are primarily a result of this backscattering effect; the probability of a random double β coincidence is very small considering our β event rate of typically $\lesssim 30$ Hz. The fraction of these backscattered events in the ^{38m}K data was 1.12% of the total number of accepted β (one DSSSD hit) events using $\sigma_{\rm cut} = 1$ in the analysis scheme. If the DSSSD energy agreement is increased to $\sigma_{\rm cut} = 3$, the fraction of backscattered β's increases to 1.35%. In either case, events where there was more than two groups in $\hat{x}$ or $\hat{y}$ were still excluded (less than 0.09%), and not considered to be a backscattered β. GEANT simulations can also have these backscattered events tagged, and the comparison to the on-line data gives an idea as to how well GEANT calculates scattering within the scintillator. The result of a simulation of the unweighted β spectrum was 1.22%. This is in agreement with the data, considering the spread in the results from the choice of $\sigma_{\rm cut}$.

4.4.3 Uniformity of Response

The gain of the scintillator may vary according to where in the plastic the scintillation light was generated because the light collection efficiency can vary with position. Off-line tests were performed with a ^{207}Bi source where the source was moved along the length of the scintillator, with variations in the gain found to be at the 1% level.

This preliminary result is encouraging, but the effect on the correlation experiment can be different. By placing different position conditions on events in the DSSSD, we can use the on-line ^{38m}K data to map out the non-uniformity. The difference in the β spectra of the different cuts can be used to determine our sensitivity. For example, if we define an 'inner' DSSSD position cut and and outer DSSSD cut, we can check that the light collection of the scintillator around the centre is the same as near its edge. In order to obtain good statistics on the β spectra, a large area at the centre of the DSSSD (defined by a $\varnothing$1.2 cm circle) was chosen for the inner cut; an outer area defined by strip positions outside the $\varnothing$2.4 cm circle has the same area as the inner circle. Circles are defined (rather than 0.1 mm wide squares) because of possible inter-strip events, even though they are but a small fraction of the single-strip events. Note that these circles *do* in fact have an equal number of the dominant single-strip pixels (only one strip in $\hat{x}$ and one in $\hat{y}$).

The β spectra of Figure 4.34 are the results where the inner and outer position conditions were imposed on the ^{38m}K data set. The outer DSSSD events' efficiency is 83% that of the inner ones and this is mainly due to the reduced efficiency of the edge strips as discussed in §4.2.5. In order to aid in comparison of the spectra, this relative inefficiency has been corrected for by renormalizing the inner DSSSD's spectrum to have an equal number of counts as the outer. The plot in the upper right of the figure is the difference in the number of counts, and generally the agreement can be seen to be very good. The difference is $\lesssim \pm 5\%$ in the number of counts (for energies less than 4 MeV; see plot in upper right of Figure 4.34) indicating uniformity of the scintillator and telescope as a whole to the direction of the incident β.

Above 4 MeV, the difference *is* a considerable fraction of the total number of counts and we should determine how sensitive our measurement of the correlation parameter, a, will be to this non-uniformity. To that end, full Monte Carlo [65] simulations with

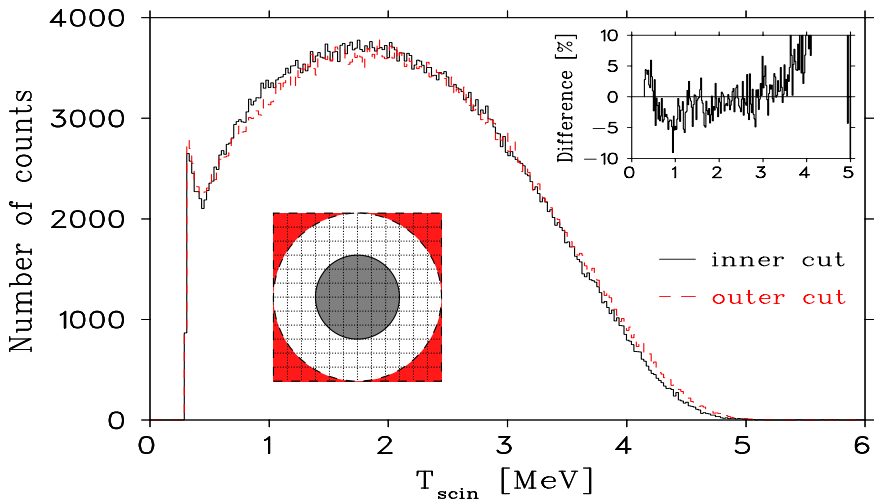

FIGURE 4.34: Uniformity of response of the plastic scintillator. The two β spectra differ by the position condition of the DSSSD imposed on them: the shaded ∅1.2 cm circle in the centre ('inner') and the shaded area of the corners ('outer') chosen such that the two have equal DSSSD areas. The plot insert in the upper right is the (percentage) difference in the number of counts between the two spectra.

both responses must be performed. The resulting fits of a to these fake data, and their deviations from that input into the MC, will give us the relative importance of the telescope's uniformity.

4.4.4 The Fierz Interference Term

The Fierz interference term, b_e, of Equation (2.24) will, in general, be non-zero if $a \neq +1$; this is made explicit by Adelberger, et. al [10] when they express their measurement in terms of $\tilde{a} \equiv \frac{a}{1+b_e\langle m_e c^2/E_e\rangle}$. The final analysis of TRINAT's $\beta-\nu$ correlation experiment may very well incorporate b_e by directly fitting the $C_{S,V}$ and $C'_{S,V}$ parameters; in the present analysis scheme, our sensitivity to this interference term will be small because it only considers events above $E_\beta = 2.5$ MeV where $0.093 < m_e c^2/E_e < 0.17$. With the limit of $|b_e| \leq 0.007$ [11], the impact on the correlation parameter is relatively small: $\tilde{a}$ would only differ from a at the 0.1% level.

The ability to reproduce so well the unweighted β spectrum for the ^{38m}K data allows us to consider fitting b_e using the telescope on its own. A preliminary investigation into this prospect has been completed which looks very promising, but a more

detailed analysis is necessary to compete with current limits. The unweighted β spectrum was fit to MC simulations as in §4.3.5, but this time the number of counts in this MC spectrum was renormalized by (see Equation (2.24) with Jackson, Trieman and Wyld's Coulomb correction):

$$N'_{MC}(E) = \frac{N_{MC}}{1 + b_e \frac{m_e c^2}{E_e}\sqrt{1-(18\alpha)^2}} \tag{4.19}$$

where b_e was a free parameter in the fit. The other parameters left free to vary were the slope of the energy calibration (λ of Equation (4.10)) as well as the relative normalization and resolution of the ^{38}K background (which was *not* renormalized by Equation (4.19)). The slope of the calibration in this fit agreed with the fit when b_e was set to zero: $\lambda = 289.59 \pm 0.13$ versus 289.72 ± 0.15 channels/MeV and $x_\circ = 42.2 \pm 0.4$ versus 42.3 ± 0.4 channels). This is an important result because it shows that the Fierz interference term will not bias our on-line β calibrations of the scintillator. The normalization of the γ background did significantly change, however, and was *highly* correlated with b_e (97%). This is a result of the poor spectrum shape of the background simulated by GEANT, and limits our sensitivity to b_e since energies below the Compton edge are where the interference term will have the largest effect. The result of this fit was $b_e = -0.05 \pm 0.03$ which is much larger than the limit of $|b_e| \leq 0.007 \pm 0.005$ [11] reported earlier. If only λ of the calibration and b_e are left free (with the background fixed to the results of the fit with $b_e = 0$), then the limit on b_e is very good and comparable to the published results: $b_e = -0.003 \pm 0.008$. There is no justifiable reason for fixing the background parameters, however, and this result is only an indication of what limits may be attainable once efforts in understanding the shape of the ^{38}K background are complete; in addition, questions about non-linearities in the scintillator gain will need to be addressed, and calculable higher-order corrections must also be included.

4.5 β–Ar Coincidences

The MCP–β-telescope coincidence spectra are presented in this section. As this is largely the basis of A. Gorelov's thesis [18], the analysis contained here is preliminary

and only meant to give an indication as to how the β-telescope will be used (as well as how it will perform) in the $\beta - \nu$ correlation experiment. The first section explains the scattering effects that are present in our geometry and shows how well GEANT reproduces them. The other section compares simulations of β spectra where a recoil coincidence is required to those observed on-line in April/May 1999.

4.5.1 Scattering Effects

The plot in Figure 4.35 is a Monte Carlo simulation of the $\beta-\nu$ correlation experiment for the Ar^{+1} recoils. This MC is a combination of GEANT (positron tracking) and A. Gorelov's (recoil tracking) code [65]. The electric field of -829 V/cm is not strong enough to collect all of these recoils, but it does increase the efficiency greatly and is easily implemented in the analysis if it can be considered uniform, as it was in the simulation. The efficiency of the MCP is assumed to be uniform, and its active area has been assumed to be $\varnothing$2.5 cm. The kinematic limits indicated in the figure were calculated for the back-to-back geometry using point-like detectors with an ideal β response function. The Monte Carlo includes the finite trap and detector sizes, as well as the energy and timing resolution of the β-telescope; the Compton summing of the annihilation radiation is clearly evident as a ridge at β energies above the slow branch.

The events outside the kinematically allowed region at longer times-of-flight deserve special attention because they correspond to positrons which were not emitted toward the β-telescope, but (predominantly back-) scattered before entering; this will bias the initial direction of the recoil and hence the TOF. Consider the case where the Ar^{+} ion recoils toward the β detector; the electric field is strong enough that it will be turned back and accelerated onto the MCP. If the decay is in the fast branch of this 'reversed geometry', then the recoil TOF will be constant (at ≈ 1 μs) and the leptons will both be emitted toward the recoil detector. The positron then has a non-negligible probability of backscattering off the MCP (lead glass) or one of its electrostatic hoops (aluminum) into the β-telescope. If this happens, the event would be detected just like a 'good' $\beta -$ Ar coincidence, but outside the kinematic limits at longer TOF. These events are plotted separately in the bottom of Figure 4.35. Now

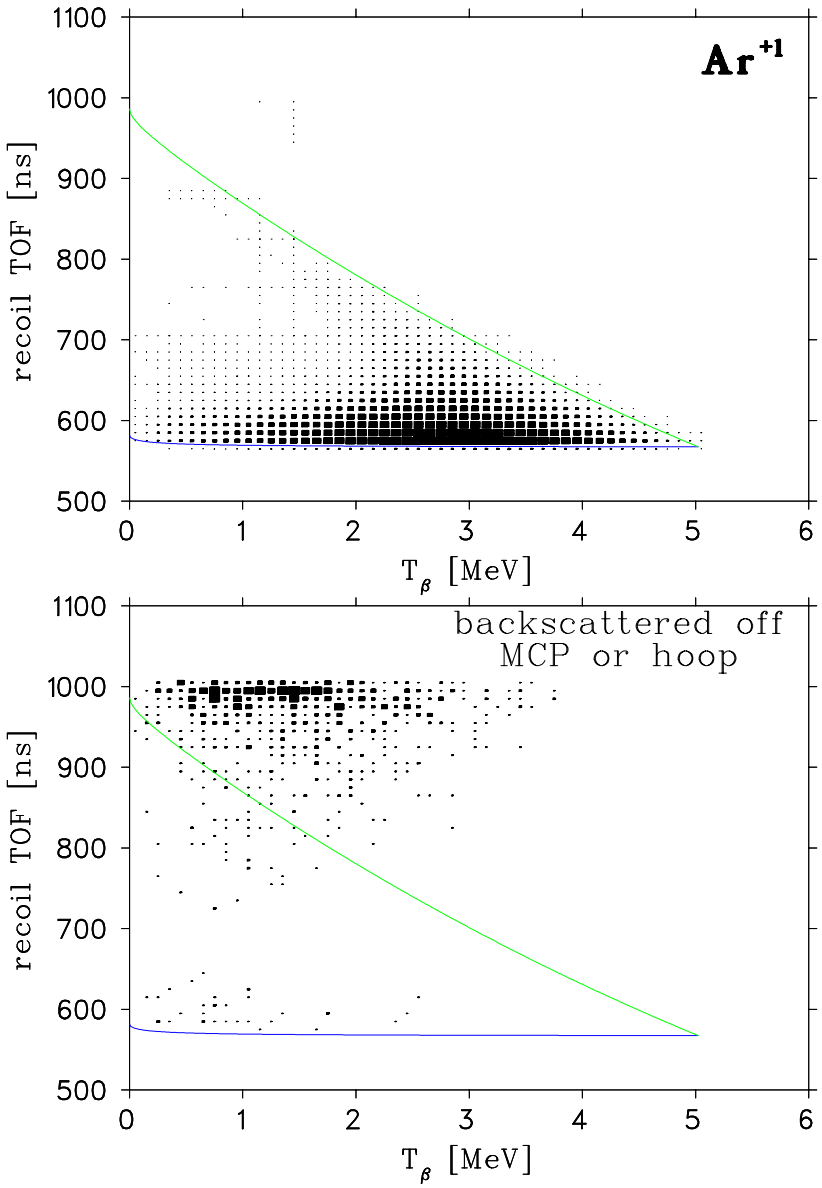

FIGURE 4.35: Monte Carlo simulation of the recoil TOF as function of β energy for Ar^{+1} recoils (top) with the kinematic limits for the back-to-back geometry (solid lines). Events in the kinematically forbidden region at longer times-of-flight are a result of positrons that scattered before firing the β-telescope. Most of these events are a result of the β backscattering off the recoil detector or one of the electrostatic hoops (bottom).

consider a backscattered[†] β which came from the slow branch; the recoil in this case is directed *toward* the recoil detector rather than away, and so the event is detected at *faster* TOF. Essentially, the spectrum shape of the backscattered βs will have the same form as the 'direct' ones, but it is reversed in TOF and shifted down in β energy (from the energy lost in the volume where it backscattered).

The events where positrons backscattered off the MCP or one of the hoops were tagged in the Monte Carlo once it was found to be a clearly visible background. Table 4.8 gives the percentage of β–Ar coincidences where the positron scattered off a volume before firing the telescope. The G10 frame of the DSSSD and the inside part of the front face of the telescope vacuum chamber that defines the β window are seen to scatter the largest fraction of the events. Exclusion of the edge strips does not reduce these scattered events as much as one might expect; this agrees with the lack of (real) low-energy tails observed in the edge strips, although other systematic effects still favour restricting the DSSSD active area. The major concern regarding these events is that though they will appear to be good β events, they will be registered in the wrong DSSSD position (and so will yield an incorrect measurement of $\theta_{\beta\nu}$) and will be in the low-energy tail due to the energy lost when scattering. The MCP and electrostatic hoops are the dominant source of backscattered β events and explain most of the background seen above the slow branch in TOF; additional volumes off which the β can backscatter include the mount for the hoops behind the MCP, the MCP's flange and the vacuum chamber itself.

We do in fact see evidence of these backscattered βs in the on-line data, which is given in Figure 4.36. A comparison of this with the simulation of Figure 4.35 shows that the two are very similar and that the MC does a good job of reproducing the scattered events. The two differences between them are a small constant background from random MCP–telescope coincidences, and the tail of Ar^{+2} events at TOF $\lesssim$ 550 ns. The TOF for the fast branch of the backscattered events of the Ar^{+2} will overlap the (direct) fast branch of the Ar^{+1}. This same effect will occur for all higher, otherwise resolved, charge states as well. Once a E_β cut of 2.5 MeV is applied, however, the backscattered peak is greatly reduced, and the different charge states *are* separated

[†]This definition of 'backscatter' is not the same as in §4.4.2; in this case, it corresponds to positrons that were initially emitted in the $-\hat{z}$ direction.

β scattering volume		Ar^0	Ar^{+1}	Ar^{+2}	Ar^{+3}	Ar^{+4}
Forward scattering (low T_β)	Steel around β window					
	— including edge strips	1.85%	2.59%	2.69%	2.73%	2.72%
	— excluding edge strips	1.73%	2.27%	2.47%	2.48%	2.42%
	G10 DSSSD mounting					
	— including edge strips	1.42%	2.03%	2.28%	2.45%	2.55%
	— excluding edge strips	1.32%	1.65%	1.85%	2.02%	2.02%
Back scattering (low T_β; long TOF)	Lead glass of MCP (including edge strips)	0.28%	0.12%	0.17%	0.19%	0.20%
	Electrostatic hoop (including edge strips)	0.48%	0.78%	1.00%	1.23%	1.44%

TABLE 4.8: GEANT calculations of the percentage of βs that scatter before firing the telescope for various Ar recoil charge states.

in TOF so that this is not a serious concern.

A measure of the quality of the GEANT simulations can be estimated by comparing the TOF projections of Figures 4.35 and 4.36. Such a comparison for the Ar^{+1} recoils is given in Figure 4.37 where the background was fit to the events between the Ar^{+1} and Ar^0 peaks, and the summed curve (Monte Carlo + background) is normalized to have the same number of counts as the on-line data. The MCP positioning is not fully understood at the present time, and known non-uniformities in the electric field of the April/May 1999 data are not included in this preliminary analysis. However, once they are, the comparison over the peak of the fast branch should improve greatly. The backscatter peak is not quite as large as in the data, but the MC does account for most of it; the addition of the ceramic rods used to mount the electrostatic rings into GEANT's geometry should reduce this difference even further in future simulations that include them.

Regardless of the outcome as to GEANT's reliability in its absolute scattering rates once a detailed analysis is completed, it has already helped improve the experiment

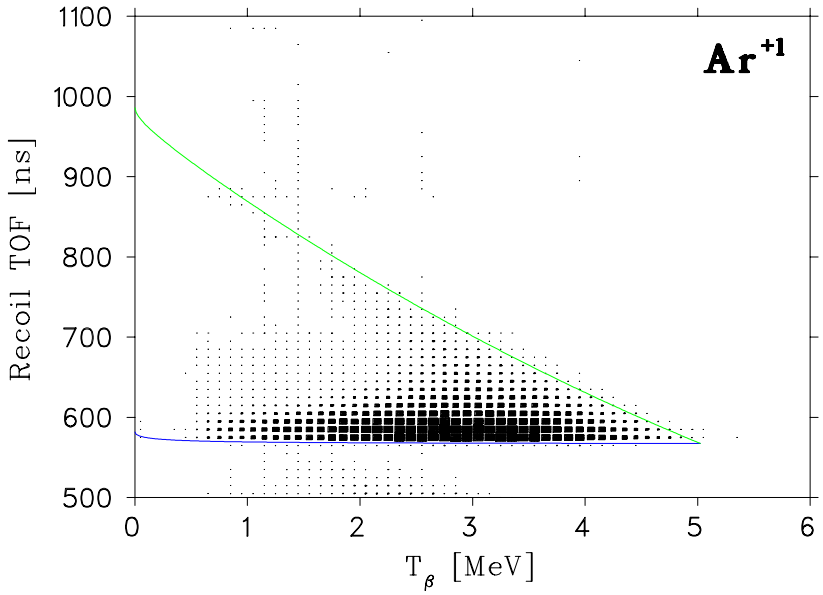

FIGURE 4.36: Scatter plot of recoil TOF versus T_β from the on-line ^{38m}K measurement. The same kinematic limits as in Figure 4.35 are plotted for comparison.

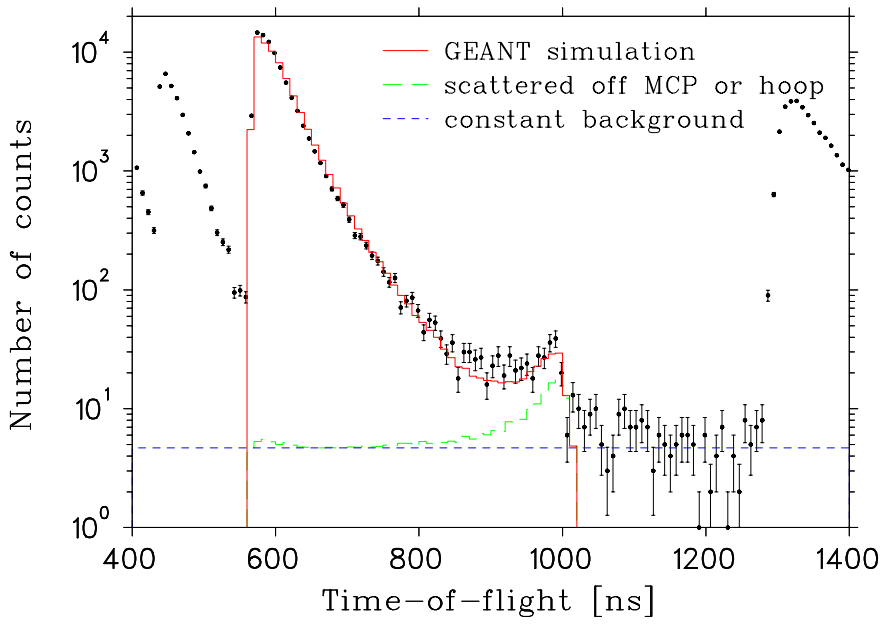

FIGURE 4.37: TOF projections for the Ar^{+1} and comparison to GEANT. The solid line represents the full GEANT simulation; of these, the dashed line are events where the positron backscattered off of the MCP or one of its electrostatic components before entering the β-telescope.

by identifying the backscatter background and, once known, its TOF has proven to be useful in understanding the electric field.

4.5.2 ^{38m}K β – Ar Coincidence Spectra

Although not easily evident in the scatter plots of the previous section, the β–Ar coincidence condition virtually eliminates the ^{38}K background. This can be clearly seen by the examining the recoil-coincident β spectra and looking for any sort of bump at around 1.9 MeV. Using the same analysis as was done for the β spectra in §4.3.5 and §4.4.1, these spectra are given in Figure 4.38 for the different recoil charge states Ar^0, Ar^1 and Ar^2; the Ar^3 and Ar^4 are continued in Figure 4.39. Both the scintillator (left) and the scintillator + DSSSD spectra (right) are compared[†] to MCs.

Happily, there is no evidence of a ^{38}K background in any of the spectra; this result is expected because the probability of the γ firing all three detectors is *extremely* small. In fact, the MCs generally agree very well with data for $T_{\rm scin} \approx T_\beta \lesssim 2$ MeV. It is for this reason the claim was made (see page 85) that the discrepancy in the scintillator's β spectrum was predominantly due to the ^{38}K background, and not from a grossly incorrect GEANT simulation of the low-energy tail. Note in particular how GEANT correctly reproduces the Compton edge from the 511 keV annihilation quanta in the scintillator spectra; this indicates that the discrepancy in Figure 4.29 is due predominantly to the misunderstood ^{38}K background, and not GEANT's simulation of the background.

We can actually hope to one day *test* the low-energy tail of GEANT's response function by seeing how well it reproduces the data of these background-free spectra. At present, however, the data are subject to a number of uncertainties:

- The MCP efficiency. This is most notably true for the Ar^0 because their efficiency is unknown and may vary significantly. The charged recoils are all accelerated to energies where the response is flat to within 2%.

- The electric field. Considerable effort has been made to understand the electric field as thoroughly as possible [57], but the preliminary analysis presented here

[†]Note, they are not, in any way, *fitted*; the relative normalization is chosen so the data and MCs have an equal number of counts.

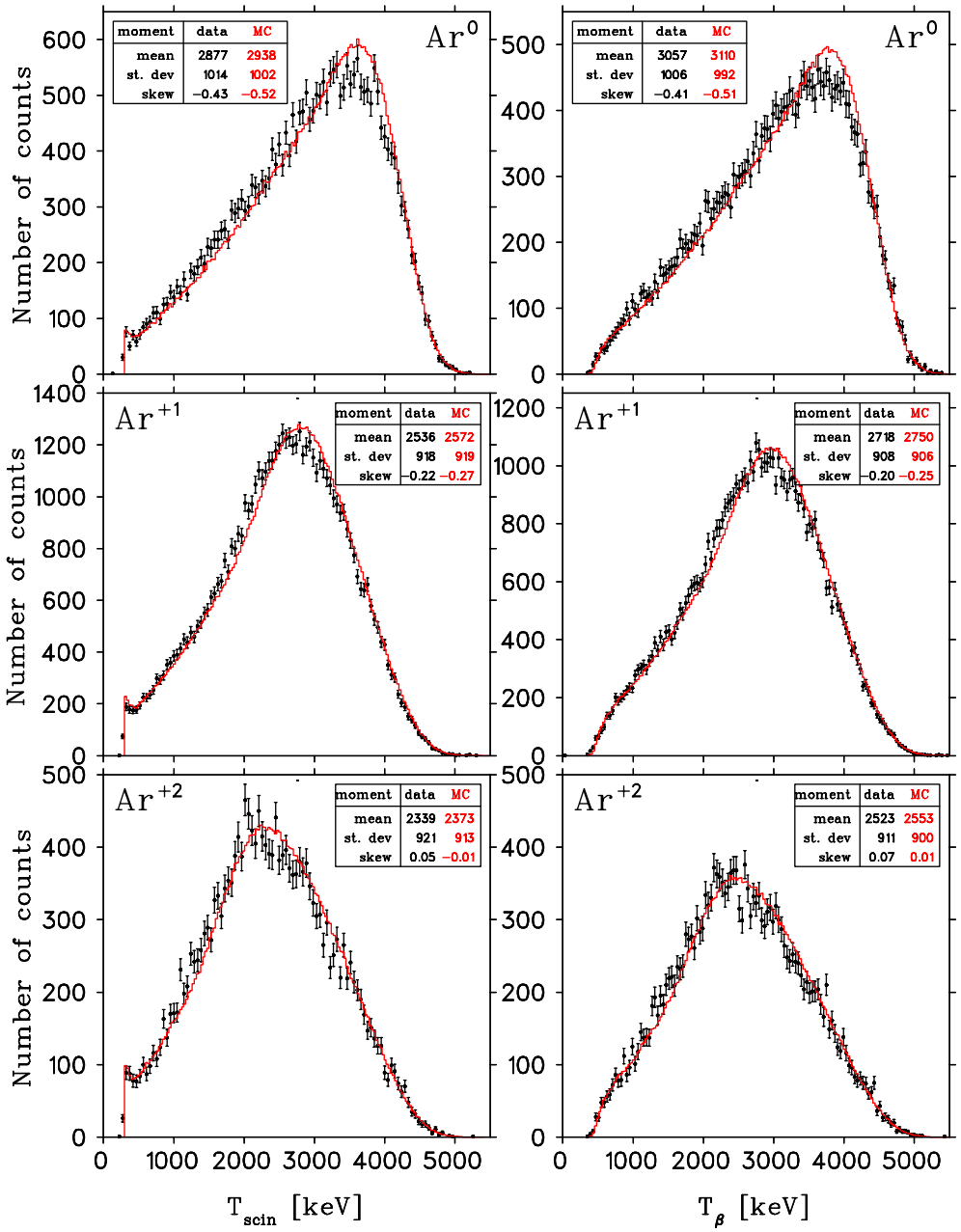

FIGURE 4.38: The ^{38m}K β spectra coincident with Ar^0, Ar^{+1} and Ar^{+2} recoils. Overlayed is a Monte Carlo simulation which assumes a uniform MCP efficiency and a uniform electric field of -829 V/cm. The calibration was taken from the fit of the unweighted β spectrum, Figure 4.29 on page 84.

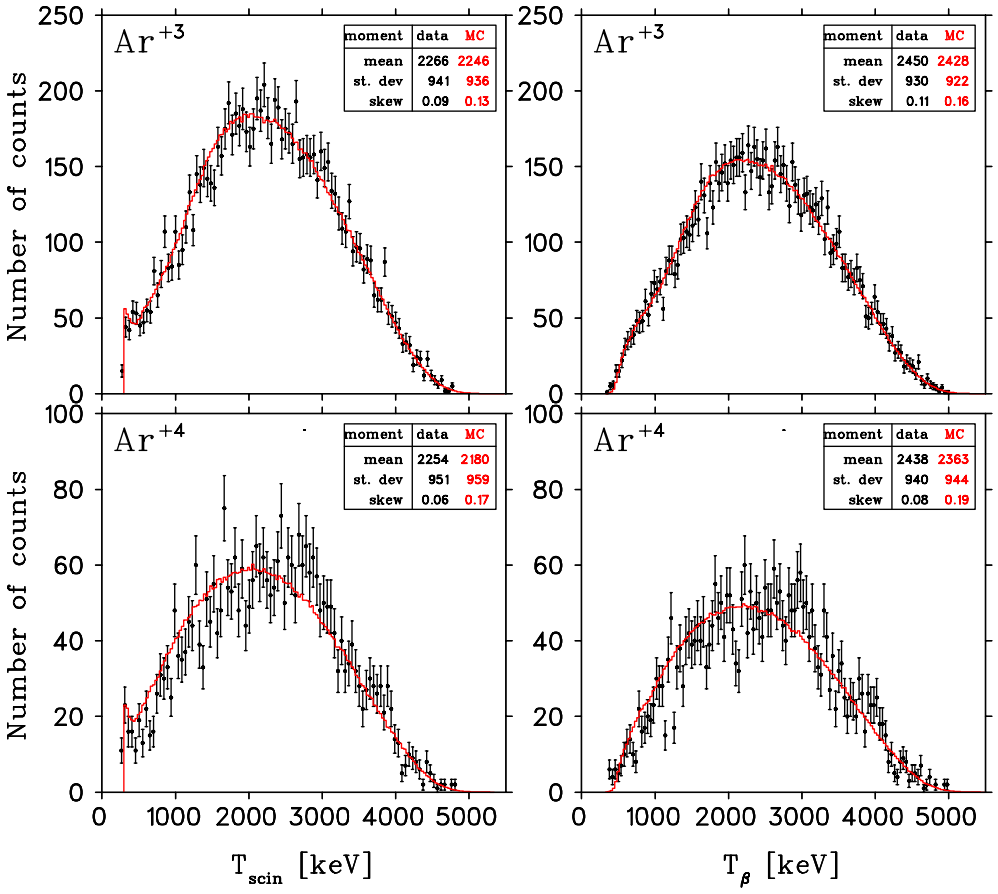

FIGURE 4.39: The ^{38m}K β spectra coincident with Ar^3 and Ar^4 recoils and comparison to Monte Carlo simulations.

has not incorporated known non-uniformities. Indications are that the field was close to -829 V/cm near the trap, but decreased to about -780 V/cm at the surface of the MCP.

- The active area of the MCP. The position spectrum of the MCP is not fully characterized yet and this affects the present discussion because, although we are integrating over the whole area, we need to accurately know what that area is. It was found that by changing the MCP radius by 1 mm the resulting spectra were noticeably different, especially for the neutrals and lower (< 3) charge states.

Considering these varied systematics, the present comparison of GEANT to the on-line data must remain relatively qualitative. The different charge states were chosen by simple cuts in TOF; a more detailed analysis should consider the overlap of higher charge states. To indicate the differences that currently exist, tables of the first through third moments of the two spectra are given in each plot of Figures 4.38 and 4.39. The differences are largest for the Ar^0 data which is most likely a result of the MCP efficiency. All of the charged recoils have better agreement which is expected since the uncertainties in the electric field are less than the uncertainty in the efficiency of the neutrals. As we go to higher charge states, the coincident-β spectra look more and more like unweighted β spectra and the agreement generally improves.

Once the systematics are better understood, a detailed analysis of the recoil-coincident β spectra may be made. This would complement fitting the β-singles spectrum down to threshold once the shape of ^{38}K ground state background has been measured.

Chapter 5

Conclusions

A β-telescope consisting of a double-sided silicon-strip detector and a plastic scintillator has been designed and constructed to observe the positrons emitted in the β decay of ^{38m}K.

The energy calibration of the plastic scintillator has been accomplished using the Compton edges of various γ sources as well as by fitting the on-line β spectrum to detailed Monte Carlo simulations. The resolution of the scintillator is derived from the Compton edge analysis and found to follow the square-root law expected if it is dominated by scintillation photon statistics. The width, $\sigma_{\delta t}$, of the scintillator's timing resolution relative to a micro-channel plate detector has been measured to be one nanosecond. These characteristics fulfill, and in some cases even surpass, the specifications we had set when designing the scintillator.

The calibration and resolution of each strip of the ΔE detector have also been determined by using both low-energy photon sources as well as the on-line data themselves. The strip detector is an essential component of the β-telescope because, in addition to providing the position information needed for a measurement of the positron's momentum, it is an effective tag for β events and greatly reduces γ backgrounds.

Monte Carlo simulations using GEANT are generally in good agreement with the measurements of TRINAT's April/May 1999 ^{38m}K data set for observables that are independent of any scalar interactions which will be determined in the final analysis. There is a $\langle E_{\mathrm{DSSSD}} \rangle = 10.3$ keV discrepancy between the MC and the measured energy spectrum in the strip detector that is not presently understood, but the impact on the total T_β measurement was found to be negligible. The simulations reproduce

the scintillator's β spectra very well, although our understanding below 2.2 MeV is complicated by the large ^{38}K (ground state) γ background. The $E - \Delta E$ coincidence reduces this background by more than 99.5%, but there is still about a 15% contamination in the telescope's β spectrum. GEANT calculations of the fraction of βs that backscatter out of the plastic and through the strip detector a second time are in agreement with those found in the data.

The goal of TRINAT's ^{38m}K β decay experiment is to make a precise measurement of the $\beta - \nu$ correlation parameter a. The β-telescope's most significant contribution to the uncertainty in this measurement, σ_a, is 0.05% taken from the uncertainty in the β calibration of the scintillator; possible non-linearities in the gain may increase this uncertainty to 0.5%. The uniformity of the scintillator's response over the active area of the strip detector has been investigated, and small differences are noticed. This is a concern because it will be highly correlated with $\theta_{\beta\nu}$, but an estimate of the contribution to σ_a still needs to be performed. The ground state's γ background, prevalent in the telescope's unweighted β spectra, is virtually eliminated once a recoil is required to have fired the micro-channel plate detector. These Ar-coincident β spectra have been compared to preliminary MC simulations and though the spectra are reproduced reasonably well, further detailed analysis will improve the agreement; in particular, understanding the active area of the micro-channel plate and proper inclusion of the non-uniform electric field are necessary for the a measurement.

The data set from April/May 1999 has enough statistics for a 0.3% measurement of a, but the final analysis is still in progress. Continued experiments are planned with an improved geometry for a cleaner measurement with better statistics. Although the energy and timing measurements of the positron in this data set are precise enough considering the statistics accumulated, further improvement in our understanding of the β-telescope is of course desirable, and below we outline how this may be accomplished.

The greatest advancement may be made by experimentally determining the shape of the ^{38}K background and by reducing the amount of this background relative to the ^{38m}K β spectrum. According to GEANT simulations, the plastic scintillator is much larger than is necessary for the experiment; by simply making the scintillator half the current length, we should be able to reduce this background by a factor

of two. The shape of this background can easily be determined in TRINAT's next experiment by accepting ISAC's potassium beam but not trapping the isomer; we can then measure the spectra of just the ground state where both the E and ΔE detectors fire. Such a determination would aid in calibrating the scintillator and is essential if the unweighted β spectrum is to be used to measure the Fierz interference parameter, b_e.

The need for the large corrections in the extended calibration of the strip detector may be reduced with a better initial calibration of the strips, particularly if this calibration covers more of the experiment's energy range. Calibrations using an open electron conversion source would complement the low-energy photon sources and may help to explain the small discrepancy between GEANT's simulation of the strip detector's spectrum with that observed in the data.

Possible non-linearities in the scintillator's energy calibration should be investigated further using γ sources over the energy range $2 - 4$ MeV. Additionally, extending the Compton edge calibration to higher energies may reduce the differences observed in the γ and β calibrations of the scintillator.

Although GEANT seems to reproduce the experiment very well, a complete understanding of the telescope's response function can only be made using a well characterized beam of mono-energetic positrons. Such a study could be undertaken at a dedicated facility such as the pelletron facility at the Max Planck Institute at Stuttgart [66], or at TRIUMF as has previously been done [40]. The appeal of Stuttgart is the excellent beam quality whereas doing it locally would allow us more time to optimize the set-up and reproduce the environment of the correlation experiment as closely as possible.

Appendix A

Response function of the scintillator

Ideally, the signal generated by the scintillator, x_{ADC}, is a perfect representation of the energy deposited in it, T_{scin}. In reality, every detector has a response function which relates the actual energy deposited and the resulting observed signal. Typical response functions (shown in Figure 4.1) have a large peak corresponding to the incident particle's kinetic energy as well as a low-energy tail where part of the energy loss was undetected. The positron response function has an additional high-energy tail due to the finite probability of detecting the annihilation radiation as well.

To understand the characteristics of the response, we need to understand the process by which the particle is detected. The incident particle interacts with the scintillator and suffers energy loss through Coulomb interactions with atomic electrons. These electrons are then excited to a higher energy level in the atom (excitation) or, if the energy transferred is greater than the binding energy, is ejected into the continuum. In the latter case, these freed atomic electrons (which are known as δ rays) suffer energy losses and excite other atoms as they transverse the scintillator, just like the primary particle. The atoms in the excited states rapidly decay to the ground state by fluorescing, which is to say they emit (visible) photons. Some of these photons are collected on the photosensitive surface of an optically coupled photo-multiplier tube (PMT), ejecting (at most) one photoelectron per photon. These photoelectrons are accelerated and focused by electrodes called dynodes, which are typically made of materials with a high secondary electron emission probability so that the cascade is multiplied as well. The resulting pulse after repeated amplification through the dynode structure of the PMT, is the final signal generated by the scintillator.

A.1 Saturation Effects

The efficiency of the excitation process is not unity and in fact is dependent on the local energy loss. Since there are a finite number of atoms near the ionizing particle, it is reasonable to expect that as the dE/dx gets large, the efficiency is reduced as there are fewer atoms nearby that are still in the ground state. This saturation effect was first investigated semi-empirically by Birks [67] who parameterized the amount of scintillation light generated (luminescence) in terms of the energy loss:

$$\frac{dL}{dx} = \mathcal{A}\frac{(dE/dx)}{1 + k_B\frac{1}{\rho}(dE/dx)} \tag{A.1}$$

with $\mathcal{A}$ a proportionality constant, ρ the density of the medium and k_B is a factor which Birks found to depend primarily on the type of particle. The number of scintillation photons generated is proportional to the integral of Equation (A.1) over the range of the particle's track. In the limit that $\frac{dE}{\rho dx} \ll \frac{1}{k_b}$, the scintillation light generated *is* proportional to the energy lost, and saturation only becomes important for large dE/dx. For Compton electrons and β's, $k_B = (9-10)\times 10^{-6}$ g keV^{-1} cm^{-2}, so that $dL/dx \propto dE/dx$ to within half a percent below energy losses of about 5 MeV/cm.

If the incident positron has energies greater than about 100 keV, the energy loss will be relatively flat at about $dE/dx \gtrsim 1$ MeV/cm (see Figure A.1). These positrons will only be slightly modified by the saturation effects. The energy loss of positrons below 100 keV is larger; in this case, the Birks effect can become significant and may affect the amount of scintillation light generated. As this is well below the scintillator's threshold, we do not need to worry about these low-energy effects for the correlation experiment.

This quenching effect, however, not only occurs for the primary particle, but also to any generated secondaries, such as δ rays. The positrons in the energy range of interest to the experiment may not be heavily affected by saturation, but it is difficult to predict how large the dE/dx of the generated secondaries will be. To estimate this effect, GEANT simulations were performed where the Birks factor was included in the scintillator's response. The value used was $k_B = 10 \times 10^{-6}$ g keV^{-1} cm^{-2} and the results are given in Figure A.2. This is a scatter plot of the initial β's kinetic energy against the energy lost to saturation effects, whether from the initial positron or a

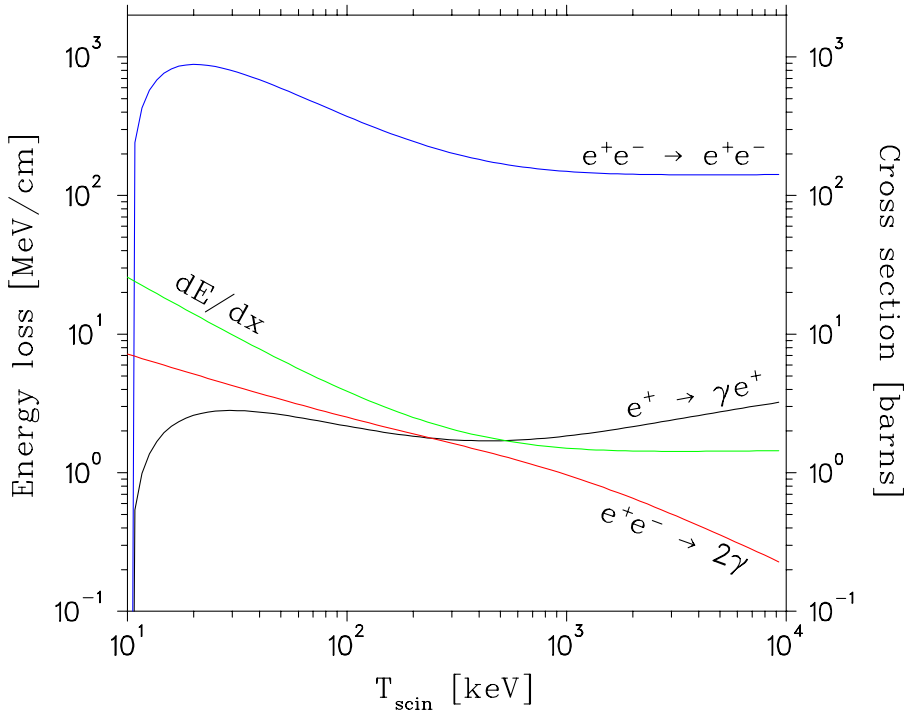

FIGURE A.1: Total cross-sections used in GEANT for the energy loss of positrons in plastic. The dominant interaction is Bhabha ($e^+e^- \to e^+e^-$) scattering which generally generates δ rays, but bremsstrahlung ($e^+ \to \gamma e^+$) and even annihilation-in-flight ($e^+e^- \to 2\gamma$) contribute.

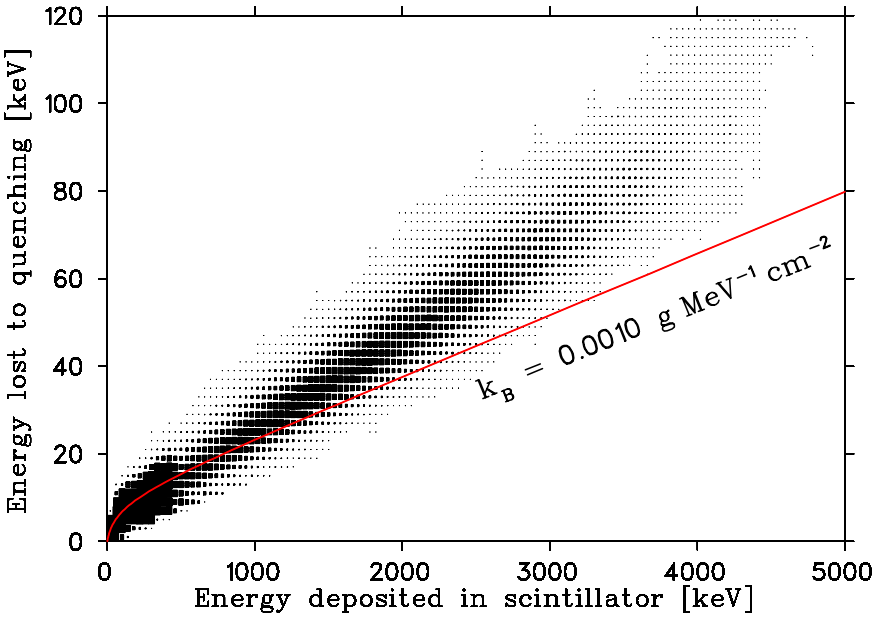

FIGURE A.2: Monte Carlo simulation of saturation effects in plastic with $k_B = 10 \times 10^{-6}$ g keV^{-1} cm^{-2}. The solid line represents the energy loss expected using Equation (A.1), but the effect is slightly enhanced due to the production of δ rays in the GEANT simulation.

secondary. The solid line is a calculation based on tables of the dE/dx for positrons in NE104 plastic (only the primary positron is considered) and Equation A.1. As both the Birks effect and δ ray production are inherently random processes, we expect to see the spread in the energy lost to quenching as seen in the figure. Note that for higher β energies, the average energy lost is *not* equal to the calculation; this is due to the higher production of δ rays which, since they are lower energy electrons, suffer more saturation than expected if no δ rays were produced.

The Monte Carlo simulation shows that this is a relatively small effect ($\lesssim 2\%$) and furthermore that it is nearly linear with energy. The quenching therefore manifests itself simply as a slight change in the slope of the energy calibration, allowing us to neglect the effect and assume that the light output *is* proportional to the energy deposited. The spread depicted in Figure A.2 indicates that, by making this assumption and calibrating to the average light output for a given positron energy, for any given event we have about a ± 20 keV uncertainty in the energy reading as a result of saturation effects. This is not important for the correlation experiment where we do not

plan to utilize the event-by-event information, but analysis which includes kinematic reconstructions (see, for example, §B.2) should make sure that this is considered.

A.2 Bremsstrahlung

The low-energy tail of the response functions arise mainly from three effects: (*i*) particles (primary *or* secondary) that escape the scintillator and therefore do not deposit all of their energy, (*ii*) radiative energy losses (bremsstrahlung) that escape detection and (*iii*) annihilation-in-flight quanta which take some of e^+'s kinetic energy out of the detector. The first is brought up within chapter 4 (design simulations and backscattering losses from the plastic) and the third is discussed in §A.3; below we briefly discuss bremsstrahlung losses.

Often as an electron or positron is suffering collisional losses within the detector, its velocity quickly changes when it scatters into large angles, which is enhanced due to their small mass. This results in drastic decelerations and since any accelerating charged particle must radiate electromagnetic energy, the $e^{\pm}$ lose energy through bremsstrahlung photons (instead of ionization losses). If these photons escape the detector instead of being re-absorbed and generated into scintillation light, the detected energy will be less than the incident particle's, thereby adding to the low-energy tail.

In the relativistic limit, which is where radiative losses contribute significantly, the ratio of ionizing energy losses to that of bremsstrahlung for electrons is given by [68]:

$$\frac{(dE/dx)_{rad}}{(dE/dx)_{col}} \approx Z\frac{T_e + m_e c^2}{1600 m_e c^2} \tag{A.2}$$

For scintillators, the $\tilde{Z} \simeq 5.6$ so that at $T_e \lesssim 5$ MeV, this ratio is less than 4% (see Figure A.3). In comparison, this ratio is 10% for a higher Z material detector, for example a Si(Li) for which $Z = 14$, . The ratio increases because the electrons are more likely to scatter into large angles; thus the Si(Li) has a larger low-energy tail in its response function than the lighter scintillator†. This was one of the motivating reasons for switching from a Si(Li) detector to the plastic scintillator described in this thesis.

†Also contributing to the Si(Li) low-energy tail are $e^{\pm}$ that backscatter out of the detector before stopping; this is also a function of the detector's Z.

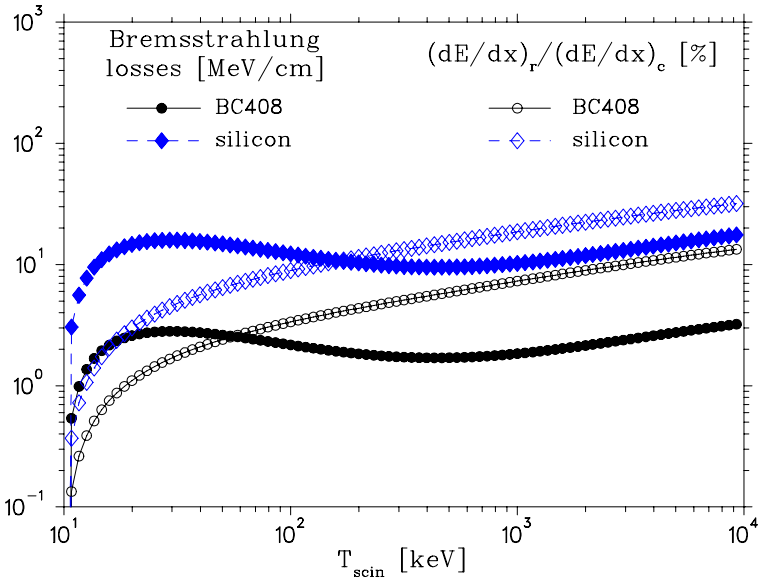

FIGURE A.3: Radiative energy losses in plastic and silicon. Both the cross-section and average radiative energy loss is reduced in plastic compared to the higher Z silicon.

The GEANT simulations of positrons include radiative energy losses (with a cross-section as given in Figure A.1), and also track the bremsstrahlung photon to see if it does get reabsorbed in the plastic before escaping. To correct for differences in electron and positron cross-sections, GEANT includes a function that scales with T/Z^2 [44]. Earlier comparisons of measured response functions to (other) GEANT calculations [40] had the MC consistently underestimating the low-energy tail. Although the response function measurements may have some systematic bias from the $e^{\pm}$ beam characteristics, the discrepancy is a concern for us because (a) of our sensitivity to the low-energy tail in the $\beta - \nu$ correlation experiment and (b) because we have not experimentally measured the scintillator's response function and are relying on GEANT to simulate them.

We are presently limited by backgrounds or systematics in our understanding of the low-energy part of our ^{38m}K spectra, and so cannot at present use the on-line data to test GEANT. Once these uncertainties are reduced, an attempt at measuring the response function for $\approx 2-3$ MeV positrons may be possible along the slow branch (see §3.1) because the β's energy is slowly varying at longer times-of-flight. Reconstruction

of E_β is possible due to the overdetermined kinematics in our geometry; comparison of the observed and calculated energies for TOF cuts along the slow branch should at least provide good estimates of the relative tail-to-total ratios of the response function. Happily, preliminary calculations [69] are in agreement with GEANT, but a dedicated study has yet to be performed.

A.3 Annihilation Radiation

Up to now, the effects have been applicable to both electrons and positrons, with perhaps only minor differences in the details. The response function of positrons will have additional components unique to them because they annihilate with free and atomic electrons.

Compton summing In the case that the positron comes to rest before annihilating with a free electron, we know from simple energy-momentum conservation that two back-to-back γs will be generated with momenta $\boldsymbol{p}_{\gamma_1} = -\boldsymbol{p}_{\gamma_2}$ and $E_{\gamma_1} = E_{\gamma_2} = m_e c^2$. If these annihilation photons do not interact with the scintillator, then the response is unaffected since the positron deposited all of its kinetic energy. However, if one Compton scatters within the scintillator, then the additional energy deposited by the Compton scattered electron will be added to the positron's signal. The positron response will therefore have a high-energy tail extending up to 340 keV from the full-energy peak. Although less likely, both annihilation γs may Compton scatter extending this tail even further, up to 680 keV. This 'Compton toe' is a concern in the correlation experiment because an improper calculation of this high-energy Compton tail will affect the scintillator's calibration; the 5.022 MeV end point will appear shifted if too much or not enough Compton summing is included.

Annihilation-in-flight An additional complication with positrons is the fact that they can annihilate *before* coming to rest (annihilation-in-flight). The γs will no longer be back-to-back and $E_{\gamma_1} \neq E_{\gamma_2} \neq m_e c^2$ as some of the kinetic energy of the positron is transferred to annihilation radiation. This time, if the annihilation γs escape the detector, the energy reading will be in the *low*-energy tail of the response

function because the positron did not deposit all of its energy in the detector before annihilating. The cross-section for annihilation into two γs is given by [70][†]

$$\sigma_{2\gamma} = \frac{\pi r_e^2 Z}{\gamma + 1}\left[\frac{\gamma^2 + 4\gamma + 1}{\gamma^2 - 1}\ln\left(\gamma + \sqrt{\gamma^2 - 1}\right) - \frac{\gamma + 3}{\sqrt{\gamma^2 - 1}}\right] \tag{A.3}$$

with $r_e = 2.818$ fm and $\gamma = E/m_e c^2$. This cross-section is compared with that of collisional losses in Figure A.1 and, though it is small compared to ionization losses in our energy range, the integrated probability of annihilation-in-flight is as large as 10% for a 5 MeV positron [71].

[†]Annihilation to one γ can occur if the electron is bound, but this cross section goes like $(\alpha Z)^4$ compared to $\sigma_{2\gamma}$ and so only contributes in high Z materials.

Appendix B

GEANT and Future Work

The success of GEANT in reproducing the observed β spectra enables us to place some trust in its simulations. This coupled with its ease of programming to suit a users needs has meant it has found applications to other aspects of TRINAT's potassium program. Two of these applications, improved geometry designs to reduce scattering and searching for massive neutrinos, are described below.

B.1 Future geometries

In order to obtain a more uniform and calculable electric field, a redesign of the electrostatic hoop system is being performed and is hoped to be implemented before the next running period. Inspired in large part by the scattering effects presented earlier (see Section 4.5.1), design simulations of the experiment are concurrently being performed to try to minimize these effects in the new geometry.

One of the major changes to the electric hoops (see Figure B.1) is in the one closest to the β-telescope. In order to be less sensitive to where ground is defined, this hoop has been changed into two wide, flat concentric rings ('hoop 5' and the collimator) maintained at different potentials. On the other side, another end plate ('hoop 0') has also been added for more uniform fields on the recoil detector's side of the trap. Then the natural questions became "What sizes (inner diameters and thicknesses) and materials (Be, Al, W, Ta) should we choose for these new volumes?" The GEANT geometry was amended to include hoop 5 and collimator so that simulations could help us to best answer these questions. The geometry was further adapted by T.J. Stocki, a research associate working with TRINAT, to reflect the rest of the changes in the

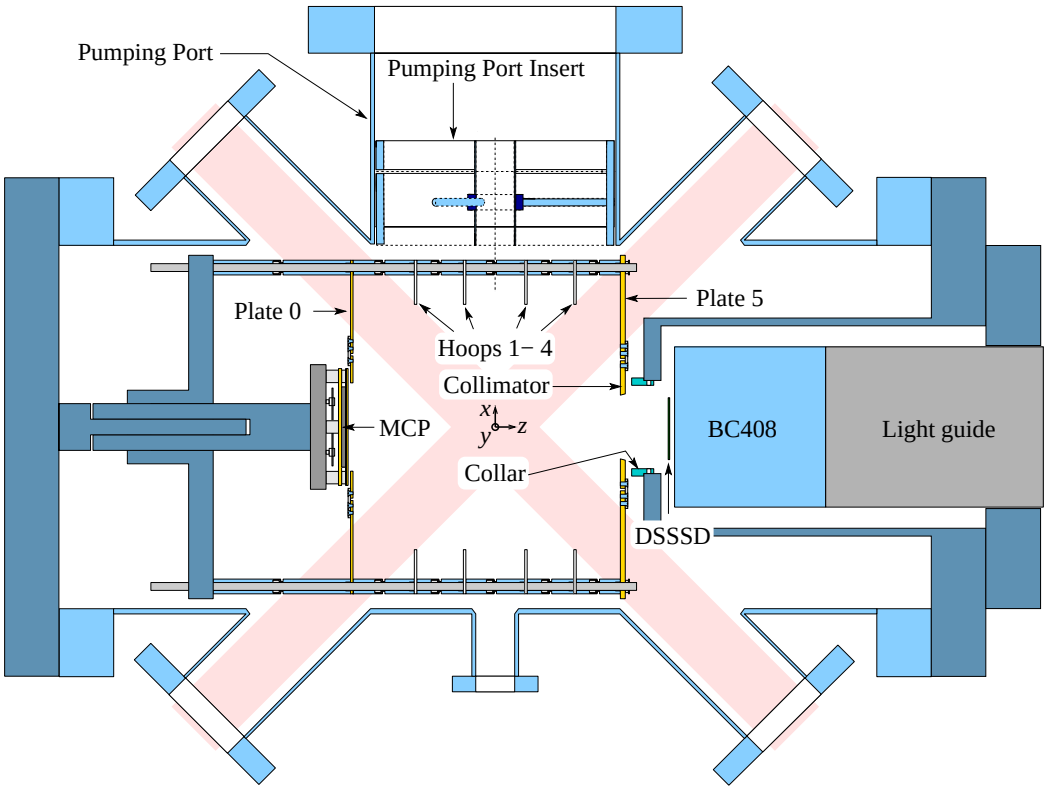

FIGURE B.1: Schematic diagram of TRINAT's new electrostatic hoop design. The changes can be seen by comparing this to Figure 4.7 on page 42.

new electrostatic hoop design, including hoop 0 and the ceramic rods used to mount the hoops.

Simulations were run for various dimensions and materials of the collimator and hoop 5; the MC indicates a factor of two improvement over the geometry presented in this thesis if a copper-tungsten collimator is used to restrict the cone of βs from the trap to hit only the foil of the β window (and not the steel of the front face). Hoop 5 is made of glassy carbon, and it was found that a number of βs scattered through it and then into the β-telescope; in an effort to reduce these new scattering effects, another copper-tungsten collimator (the 'β window collar') was added to the front face of the scintillator vacuum chamber. The collar extends out far enough that βs have no solid angle for entering the telescope directly from hoop 5 and greatly reduces these scattered events.

The material of hoop 0 was carefully considered because we want to make sure we minimize backscattering effects. If this plate is also made of glassy carbon, the βs have a good probability of transmitting through the plate rather than backscattering; once through, they readily scatter off the other (higher Z) materials, but the solid angle for firing the β-telescope is very small.

B.2 Massive neutrinos

The correlation experiment, as mentioned earlier, provides us with the momenta (both direction and magnitude) of both the recoil and the β from the ^{38m}K decay. From these measurements, we can deduce the neutrino momentum on an event-by-event basis, limited by how well the e^+ energy is measured. The kinematics of the decay described in §3.1 (on page 15) assumed a massless neutrino, and indeed we know this to be true at the eV level for the ν_e. The limits on the μ and τ neutrino's, however, are not as stringent and, if they have mass, the observable eigenstates of the weak interaction can mix with the mass eigenstates. In this case the kinematics of the decay will be quite different, as depicted in Figure B.2. For the fast branch, where there are many events, a massive neutrino will take energy away from the recoil to conserve momentum, resulting in an extra ridge at longer time-of-flight. The separation of this ridge from the fast branch where no mixing occured will be related to the mass of the heavy neutrino; for a 2 MeV/c^2 heavy neutrino in the geometry of this experiment, it corresponds to a shift of approximately 200 ns. The relative population of this ridge compared to that of the regular fast branch is determined by the probability of the electron neutrino mixing with a heavier one (as well as changes in the phase space of the decay and the angular correlation).

With the ^{38m}K decay Q-value of 5.022 MeV, our geometry should be sensitive to neutrinos in mass range of approximately $1 - 4$ MeV/c^2. The analysis, which is the central part of M. Trinczek's Ph.D. thesis [72], will reconstruct the recoil TOF, assuming a massless neutrino, as a function of T_β bins, and then compare this calculated time with the observed TOF. The massive neutrinos will be clearly visible as their reconstructed TOF will be incorrect; for this reason, they will be far removed in TOF from the fast branch's peak at $\mathrm{TOF}_{\mathrm{obs}} - \mathrm{TOF}_{\mathrm{calc}} = 0$. The overall number of

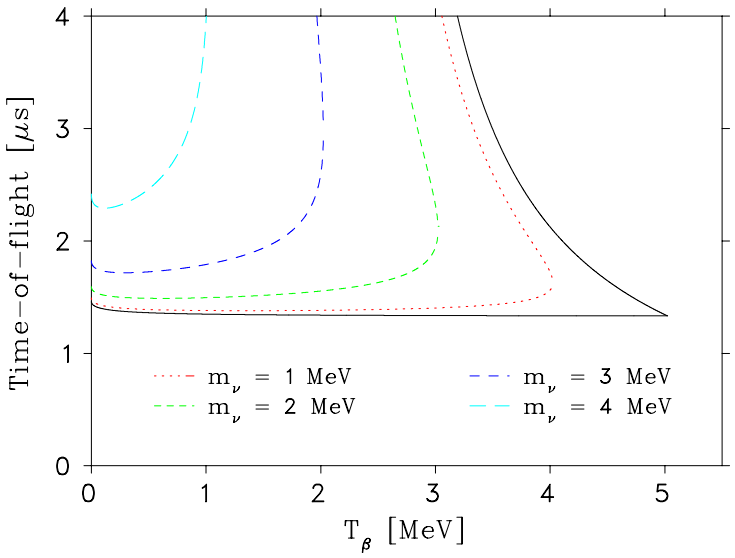

FIGURE B.2: Kinematics of ^{38m}K decay where the emitted neutrino is massive (dashed lines), for masses $m_\nu c^2 = 1, 2, 3$ and 4 MeV; the solid line is $m_\nu = 0$. The position of the heavy neutrino ridges depends on its mass, and the relative intensity of this ridge compared to that of the regular fast branch (which is related to the mixing strength).

counts in each of the two peaks will be used to place limits on the mixing strength of $\nu_e \longrightarrow \nu_{\text{heavy}}$.

In order to be able to accurately fit the (regular) fast branch's peak, a MC simulation must be performed to properly account for (*i*) various scattering effects, (*ii*) the finite trap and detector sizes, and (*iii*) the response function of the β-telescope. MC simulations [65] where the recoil and positron are tracked with a simple model of (*i*) (at most one scatter) are *much* faster than GEANT simulations ($\approx 4000\times$). This fast simulation accounts for (*ii*) and includes (*iii*) by convoluting the generated β energy with GEANT simulations of the telescope's response function[†].

The detailed tracking of the positron using GEANT, however, appears to be essential because the fast simulations fail to reproduce the tail of the main $\text{TOF}_{\text{obs}} - \text{TOF}_{\text{calc}} = 0$ peak [73]. One major source of the TOF tail is the (back)scattered βs because the reconstructed TOF will have a wrong value of $\theta_{\beta\nu}$ in the calculations.

[†]These response functions were generated in 1998, and so updating them should help to improve the fast MC

The massive neutrino peak, though shifted in TOF from the main peak, will still be in the tail of the $m_\nu = 0$ peak. Analysis of the reconstructed events, which looks for very small peaks on top of the large zero mass 'background,' therefore requires GEANT simulations since they best reproduce the $m_\nu = 0$ tails.

The $m_\nu > 0$ spectrum shape does not need to be as accurately for the analysis because it is so small compared to the main $m_\nu = 0$ peak. For this reason, the fast Monte Carlo is being used to generate the massive neutrino events and GEANT is only be needed to generate the background.

Appendix C

Electronics of the β-Telescope

A schematic of the electronics diagram for the telescope assembly is depicted in Figure C.1. Below is a brief overview of the system as a whole.

The DSSSD provides us with 24 $\hat{x}$ + 24 $\hat{y}$ = 48 energy signals and 6 groups of $\hat{y}$ timing signals (consisting of 4 strips each). Each of the 24 y-strip's timing signals have discriminators set to $\lesssim$ 15 keV; if any of the strips pass this hardware threshold, the timing signal is used to generate a (wide) DSSSD event trigger. The gain of all 48 strips is monitored using the Ortec 448 research pulser.

The scintillator energy is taken from the dynode output of the PMT after it is inverted by the LeCroy 428F linear fan-in/fan-out. The high voltage applied to the PMT is adjusted by the stabilization unit based on the LED signals observed; the intensity of the LED is (independently) maintained constant using a temperature-stabilized photodiode. The Tennelec 455 constant fraction discriminator uses the anode signal to generate the scintillator's (short) timing signal.

The gates for the ADCs and the starts for the TDCs are all derived from the LeCroy 429A unit labelled 'event trigger'. The inputs to this unit, i.e. the various event types, are:

1. A prescaled scintillator event,

2. A hardware DSSSD-scintillator coincidence,

3. DSSSD/MCP pulser events from the Ortec 448,

4. Scintillator pulser (LED) events from the stabilization unit, and

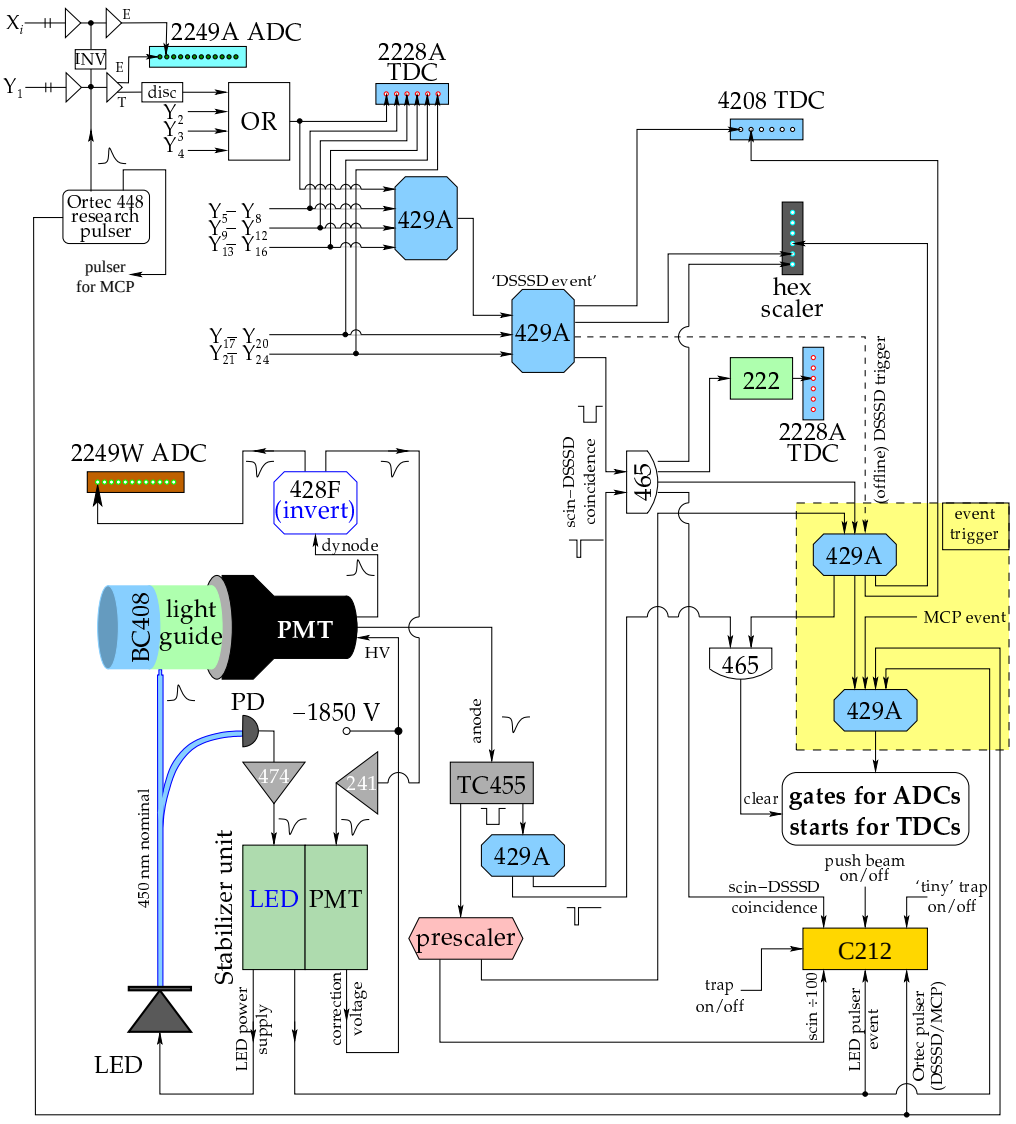

LeCroy 429A: quad logic fan−in/fan−out	LeCroy 465: triple 4−fold logic unit
LeCroy 428F: quad linear fan−in/fan−out	LeCroy 622: quad 2 input logic unit
LeCroy 2249A: charge−sensitive ADC	Ortec 474: timing filter amplifier
LeCroy 2249W: charge−sensitive ADC	Ortec 241: spectroscopy amplifier
LeCroy 4208: wide range multihit TDC	Ortec C212: coincidence register
LeCroy 2228A: high precision TDC	LRS 222: dual gate generator
Tennelec 455: constant fraction discriminator	

D. Melconian 2000

FIGURE C.1: Electronics diagram for the DSSSD and scintillator.

5. Event triggers from the MCP (though not generally used on-line because of its high rates).

The coincidence register (C212) allows us to record which of these generated the event trigger. In addition, this unit is used to define where within the trap cycle a given event took place; the signals are taken from the PC controlling the trap and tell us when the atoms are being transferred (push beam on/off), if there are atoms in the trap or if they are being loaded (trap on/off) and what detunings are used in the MOT's lasers[†] ('tiny' trap on/off).

The CAMAC system is used to acquire the data and is recorded in the YBOS format both on the disk of the host Pentium III 500 MHz Linux PC as well as on magnetic tapes. Both the on-line and off-line data analysis are done using a TRIUMF standard program [74] with a special subroutine added to incorporate the analysis scheme of the DSSSD 4.2.5.

[†]By changing the detunings once the trap is already loaded, the size of the atom cloud is reduced.

Bibliography

[1] F. Halzen and A.D. Martin. *Quarks and Leptons: An Introductory Course in Particle Physics.* John Wiley and Sons, 1984.

[2] K.S. Krane. *Introductory Nuclear Physics.* John Wiley and Sons, 1988.

[3] D. Griffiths. *Introduction to Elementary Particles*, chapter 10.7. John Wiley and Sons, 1987.

[4] E. Fermi. Zeitschrift für Physik, **88**, (1934) 161.

[5] The Particle Data Group. *Review of particle physics.* The European Physical Journal, **C3**, (1998).

[6] M.A. Preston. *Physics of the Nucleus*, chapter 15, page 424. Addison-Wesley, 1965. He cites [4] as a reference.

[7] T.D. Lee and C.N. Yang. *Question of parity conservation in weak interactions.* Physical Review, **104**, (1956) 254–258.

[8] The H1 Collaboration. *A search for leptoquarks at HERA.* Physics Letters, **B369**, (1996) 173–185.

[9] The D0 Collaboration. *Search for first generation scalar leptoquark pairs in $p\bar{p}$ collisions at $\sqrt{s} = 1.8$ TeV.* Physical Review Letters, **80**, (1998) 2051–2056.

[10] E.G. Adelberger, C. Ortiz, A. García, H.E. Swanson, M. Beck, O. Tengblad, M.J.G. Borge, I. Martel, H. Bichsel, and the ISOLDE Collaboration. *Positron-neutrino correlations in the $0^+ \longrightarrow 0^+$ decay of ^{32}Ar.* Physical Review Letters, **83**, (1999) 1299–1302.

[11] A.S. Carnoy, J. Deutsch, and P. Quin. *The superallowed* $0^+ \longrightarrow 0^+$ *beta-transitions and possible scalar coupling.* Nuclear Physics, **A568**, (1994) 265–270.

[12] J.D. Jackson, S.B. Trieman, and H.W. Wyld. *Possible tests of time reversal invariance in beta decay.* Physical Review, **106**, (1957) 517–521.

[13] J.D. Jackson, S.B. Trieman, and H.W. Wyld. *Coulomb corrections in allowed beta transitions.* Nuclear Physics, **A4**, (1957) 206–212.

[14] P.M. Endt. *Supplement to energy levels of* $A = 21 - 44$ *nuclei (VII).* Nuclear Physics, **A633**, (1998) 1–220. ^{37}K on page 180; ^{38,38m}K on page 187.

[15] E. Hagberg, V.T. Koslowsky, J.C. Hardy, I.S. Towner, J.G. Hykawy, G. Savard, and T. Shinozuka. *Test of isospin mixing corrections in superallowed* $0^+ \longrightarrow 0^+$ *decays.* Physical Review Letters, **73**, (1994) 396–399. (See also Erratum: Physical Review Letters, **74**, p. 1041).

[16] P.D. Harty, N.S. Bowden, P.H. Barker, and P.A. Amundsen. *Energy of the superallowed* β *decay of* ^{38m}K. Physical Review, **C58**, (1998) 821–25.

[17] H. Trottier, 2000. Private communication.

[18] A. Gorelov. PhD thesis, Simon Fraser University. In preparation.

[19] E.L. Raab, M. Prentiss, A. Cable, S. Chu, and D.E. Pritchard. *Trapping of neutral sodium atoms with radiation pressure.* Physical Review Letters, **59**, (1987) 2631–2634.

[20] H. Metcalf and P. van der Straten. *Cooling and trapping of neutral atoms.* Physics Reports, **244**, (1994) 203–286.

[21] G.D. Sprouse and L.A. Orozco. *Laser trapping of radioactive atoms.* Annual Reviews of Nuclear and Particle Science, **47**, (1997) 429–461.

[22] E. Arimondo, W.D. Phillips, and F. Strumia, editors. *Laser Manipulation of Atoms and Ions.* Amsterdam: North Holland, 1992.

[23] D.R. Swenson and L.W. Anderson. *Relaxation rates for optically pumped Na vapor on silicone surfaces.* Nuclear Instrumentation and Methods, **B29**, (1988) 627–642.

[24] G. Ball, D.M. Moltz, J. Cerny, J. Powell, G. Savard, J.C. Hardy, S. Bishop, J.M. D'Auria, P. Bricault, J.A. Macdonald, J.R. Leslie, H.-B. Mak, and I.A. Towner. Pure Fermi decay in medium mass nuclei, 2000. TRIUMF experiment E823.

[25] K.S. Krane, B.G. Turrell, J.L. Wood, J.M. D'Auria, B. Heinrich, C.A. Davis, P.P.J. Delheij, P. Mantica, R. Kiefl, A. Kotlicki, J. Pond, R.C.C. Ward, and M.R. Wells. Nuclear moments in the mass-100 region, 2000. TRIUMF experiment E828.

[26] S. Dunsiger, R. Miller, R.F. Kiefl, J.C. Chakhalian, W.A. MacFarlane, J. Pond, J. Sonier, B. Turrell, B.D. Gaulin, M. Gingras, R. Heffner, B. Heinrich, and B. Ittermann. β-nmr investigations of magnetic multilayers and giant magnetoresistance, 2000. TRIUMF experiment E815.

[27] R.N. Boyd, L. Buchmann, J.M. D'Auria, J.D. King, and I. Tanihata. Proposed study of the ^{8}Li$(\alpha, n)^{11}$Be reaction, 2000. TRIUMF experiment E812.

[28] N.P.T. Bateman, J.M. D'Auria, and the DRAGON collaboration. Measurement of the astrophysical rate of the ^{21}Na$(p, \gamma)^{22}$Mg reaction, 2000. TRIUMF experiment E824.

[29] J.M. D'Auria, L. Buchmann, M. Dombsky, P. McNeely, G. Roy, H. Sprenger, and J. Vincent. *Upgrade of the* TRIUMF *on-line isotope separator,* TISOL. Nuclear Instrumentation and Methods, **B70**, (1992) 75–79.

[30] J.M. D'Auria, J. Behr, L. Buchmann, M. Dombsky, K.P. Jackson, and H. Sprenger. *The* TISOL *facility at* TRIUMF*: operational status at 10 years.* Nuclear Instrumentation and Methods, **B126**, (1997) 7–11.

[31] ISOLDE user's guide. Technical Report 86-05, CERN, 1986.

[32] J.A. Behr, A. Gorelov, T. Swanson, O. Häusser, K.P. Jackson, M. Trinczek, U. Giesen, J.M. D'Auria, R. Hardy, T. Wilson, P Choboter, F. Leblond, L. Buchmann, M. Dombsky, C.D.P. Levy, G. Roy, B.A. Brown, and J. Dilling. *Magneto-optic trapping of β-decaying ^{38m}K, ^{37}K from an on-line isotope separator.* Physical Review Letters, **79**, (1997) 375–378.

[33] J. Dilling, J.A. Behr, A. Gorelov, T. Swanson, O. Häusser, D. Melconian, K.P. Jackson, M. Trinczek, U. Giesen, and J.M. D'Auria. *β-decay experiments of neutral atoms in a magneto-optic trap.* Hyperfine Interactions, **115**, (1998) 159–164.

[34] J.A. Behr, A. Gorelov, D. Melconian, M. Trinczek, P. Dubé, O. Häusser, U. Giesen, K.P. Jackson, T. Swanson, J.M. D'Auria, M. Dombsky, G. Ball, L. Buchmann, B. Jennings, J. Dilling, J. Schmid, D. Ashery, J. Deutsch, W.P. Alford, D. Asgeirsson, W. Wong, and B. Lee. *Beta-neutrino correlation experiments on laser trapped ^{38m}K, ^{37}K.* Hyperfine Interactions. (in press).

[35] P. Bricault, M. Dombsky, P.W. Schmor, and G. Stanford. *Radioactive ion beams facility at* TRIUMF. Nuclear Instrumentaion and Methods, **B126**, (1997) 231–235.

[36] R. Gückert, X. Zhao, S.G. Crane, A. Hime, W.A. Taylor, D. Tupa, D.J. Vieira, and H. Wollnik. *Magneto-optical trapping of radioactive ^{82}Rb atoms.* Physical Review (rapid communications), **A58**, (1998) R1637–R1640.

[37] T. Swanson, D. Asgeirrson, J.A. Behr, A. Gorelov, and D. Melconian. *Efficient transfer in a double magneto-optic trap system.* Journal of the Optical Society of America, **B15**, (1998) 2641–2645.

[38] Galileo. *Galileo Micro-Channel Plate data sheets.* The recoil detector is largely the work of A. Gorelov.

[39] B. Brehm, J. Grosser, T. Ruscheinski, and M. Zimmer. *Absolute detection efficiencies of a microchannel plate detector for ions.* Measurements in Science and

Technology, **6**, (1995) 953–958. See also J. Oberheide, P. Wilhelms and M. Zimmer, *New results on the absolute ion detection efficiencies of a microchannel plate*. Measurements in Science and Technology, **8**, (1997) 351–354.

[40] J. Dilling. Beta-zerfall untersuchungen von ^{37}K und ^{38m}K in einer neutralen atom laser falle. Diplomarbeit thesis, Ruprecht-Carls-Universität Heidelberg, 1997.

[41] O. Häusser. β asymmetry measurements using ^{37}K. (unpublished), 1998.

[42] E.T. Clifford. *Kinematic shifts in β delayed particle emission as a probe of $\beta - \nu$ angular correlations*. PhD thesis, University of Toronto, 1981.

[43] E.T. Clifford, E. Hagberg, V.T. Koslowsky, J.C. Hardy, H. Schmeing, and R.E. Azuma. *Measurements of the response function of a hybrid detector telescope to monoenergetic beams of positrons and electrons in the energy range 0.8–3.8 MeV*. Nuclear Instrumentation and Methods, **224**, (1984) 440–447.

[44] CERN. *GEANT Detector Description and Simulation Tool*, October 1994 edition, 1993.

[45] A. Gorelov and D. Melconian, 1999. The careful and meticulous design of the DSSSD mount was done by Alexandre.

[46] W.T. Scott. *The theory of small-angle multiple scattering of fast charged particles*. Reviews of Modern Physics, **35**, (1963) 231–313.

[47] Brush Wellman Inc. *Material specification sheet*. The type of beryllium decided upon was IF1.

[48] Bicron Corp. *Bicron data sheet*, 1997.

[49] U. Giesen. TRINAT DSSSD electronics. Locally designed and constructed, but largely based upon the Hermes electronics., 1994.

[50] C.R. Hurlbut. *Plastic Scintillators: A Survey*. Bicron Corp., 1985. Presented at the American Nuclear Society Winter Meeting, November, 1985.

[51] T. Davinson, A.C. Shotter, E.W. MacDonald, S.V. Springham, D. Jobanputra, A.J. Stephens, and S.L. Thomas. *Development of a silicon strip detector array for nuclear structure physics.* Nuclear Instrumentation and Methods, **A288**, (1990) 245–249.

[52] Micron Semiconductor Ltd. *Micron Semiconductor data sheet*, 1998. BB2-500 design.

[53] R.A.B. Shaheen. *Nuclear data sheets for $A = 133$.* Nuclear Data Sheet, **75**, (1995) 491.

[54] Y.A. Ellis-Akovali. *Nuclear data sheets for $A = 241$.* Nuclear Data Sheet, **74**, (1995) 461.

[55] J. Yorkston, A.C. Shotter, D.B. Syme, and G. Huxtable. *Interstrip surface effects in oxide passivated ion-implanted silicon strip detectors.* Nuclear Instrumentation and Methods, **A262**, (1987) 353–358.

[56] P.V. Vavilov. *Ionization losses of high energy heavy particles.* Soviet Physics JETP, **5**, (1957) 749.

[57] A. Gorelov, 2000. Private communication.

[58] M.J. Martin. *Nuclear data sheets for $A = 207$.* Nuclear Data Sheet, **70**, (1993) 315.

[59] C. Moisan. Private communication. Diffuse reflectors were found to yield the best light collection for the PET scintillators.

[60] O. Klein and Y. Nishina. Z. Phys., **52**, (1929) 853.

[61] Philips Photonics. *Photomultiplier Tubes: Principles & Applications*, 1994. see Equation (3.34).

[62] Y. Holler, J. Koch, and A. Naini. *A stabilized NE213 scintillator for neutron time-of-flight spectroscopy.* Nuclear Instrumentation and Methods, **204**, (1983) 485–490.

[63] A. Gorelov, 1998–present. The decay generation and recoil tracking subroutine, `beta_decay.F`, is taken from the 'fast Monte Carlo' [65].

[64] E.T. Clifford, 1999. Private communication.

[65] A. Gorelov, 2000. Monte Carlo simulation program (Fortran) for TRINAT's $\beta - \nu$ correlation experiment.

[66] W. Bauer, J. Briggman, H.-D. Carstanjen, S. Connell, W. Decker, J. Diehl, K. Maier, H.-E. Schaefer, A. Seeger, H. Stoll, and E. Widmann. *The stuttgart positron beam, its performance and recent experiments.* Nuclear Instrumentation and Methods, **B50**, (1990) 300–306.

[67] J.B. Birks. *Theory and practice of scintillation counting.* Pergamon Press, 1964.

[68] R.D. Evans. *The Atomic Nucleus.* Robert E. Kreiger Publishing Company, 1955.

[69] J.A. Behr, 1999. Private communication.

[70] W. Heitler. *The Quantum Theory of Radiation.* Clarendon Press, Oxford, 1954.

[71] R.B. Firestone and V.S. Shirley, editors. *Table of Isotopes*, volume II. John Wiley and Sons, 8^{th} edition, 1996.

[72] M. Trinczek. PhD thesis, Simon Fraser University. In preparation.

[73] M. Trinczek, 2000. Private communication.

[74] P.W. Green. *NOVA.* TRIUMF / The University of Edmonton, v2.0 edition, 1995.